



MONASH University

Analysis of Scattering Properties of Nanohybrids with Non-Spherical Nanoresonators and Coupled Quantum Emitters

Viraj Rangana Senevirathne Kulathunge Mudiyanse
BSc Eng (Hons)

A thesis submitted for the degree of Doctor of Philosophy at
Monash University in 2020
Department of Electrical and Computer Systems Engineering

© Viraj Rangana Senevirathne Kulathunge Mudiyansele
2020

I certify that I have made all reasonable efforts to secure copyright permissions for third-party content included in this thesis and have not knowingly added copyright content to my work without the owner's permission.

This page intentionally left blank.

Summary

Plasmonic biosensors have gained significant research interest in the past decades due to their unprecedented sensing capabilities, which allow sensing even at the single molecule level. The main component of the plasmonic biosensor is the nanoresonator that is conventionally a metal nanoparticle. Under coherent illumination, the nanoresonator gives rise to localized surface plasmon resonances (LSPRs) that are sensitive to the refractive index changes in the surrounding environment. Recently, due to tighter confinement and higher tunability of LSPRs, graphene resonators are widely explored as potential candidates for biosensing. Quantum emitters such as quantum dots and carbon nanotubes are extensively used for fluorescence-based imaging and sensing applications. When coherently illuminated, excitons, which are electron-hole pairs, are generated in the quantum emitter. If a nanoresonator and a quantum emitter are brought closer to each other, LSPRs of the nanoresonator and excitons in the quantum emitter interact with each other, and they behave like a single composite system, which is known as a nanohybrid. Due to the exciton-plasmon interactions, the scattering properties of nanohybrids are significantly distinct and have high tunability compared to that of their constituents. Because of the superior scattering properties, nanohybrids show great potential as biosensors in extremely accurate and minute imaging and sensing applications. The scattering properties of the nanohybrids can be easily tuned by tailoring the nanoresonator parameters, interparticle separation and quantum emitter properties. For nanohybrid based sensors to become mainstream, it is critical to find improved nanohybrid systems

with enhanced and tunable scattering properties. However, a majority of the previous theoretical studies were mostly focused on modelling and analysing scattering properties of nanohybrids with spherical metal nanoparticle resonators. This thesis, therefore, intends to theoretically model and analyse novel nanohybrid systems with non-spherical nanoresonators that provide additional tuning of scattering properties. It presents an elegant, versatile analytical model which can be used to analyse scattering properties of nanohybrid systems with different types of nanoresonators such as ellipsoidal, spheroidal, and disk-shaped resonators. The developed analytical model is used to investigate the scattering properties of several nanohybrid designs. The research presents an all-carbon nanohybrid with high biocompatibility and tunability that is highly suited for biosensing applications. The thesis concludes by discussing the prospect of using scattering characteristics of the proposed nanohybrid designs as biosensors in tumour detection applications.

General Declaration

This thesis is an original work of my research and contains no material which has been accepted for the award of any other degree or diploma at any university or equivalent institution and that, to the best of my knowledge and belief, this thesis contains no material previously published or written by another person, except where due reference is made in the text of the thesis.

Signature : _____

Name : Viraj Rangana Senevirathne Kulathunge Mudiyansele

Date : 14th March 2020

This page intentionally left blank.

Publications During Enrolment

- Viraj Senevirathne, Harini Hapuarachchi, Sudaraka Mallawaarachchi, Sarath D Gunapala, Mark I Stockman and Malin Premaratne **Scattering characteristics of an exciton-plasmon nanohybrid made by coupling a monolayer graphene nano flake to a carbon nanotube.** J. Phys. Condens. Matter 31 (8) 085302, Jan. 2019.
- Viraj Senevirathne and Malin Premaratne **Comparison of the permittivity sensing capabilities of graphene-based nanohybrids and metal nanoparticle-based nanohybrids.** In 2019 IEEE 19th International Conference on Nanotechnology (IEEE-NANO) 2019 Jul 22 (pp. 302-305). IEEE.

This page intentionally left blank.

Acknowledgements

Firstly, I would like to express my sincere gratitude to my supervisor Prof. Malin Premaratne for all the support, mentorship, patience, and encouragement throughout my candidature. His constructive feedback and guidance led me through challenging times. Beyond research matters, he also provided me with valuable lessons for a successful life. I could not have asked for a better supervisor.

I am especially grateful to my colleagues Harini, Sudaraka, Tharindu and Lakshitha for their ideas and support during crucial times of my research. I want to extend my heartfelt gratitude to all my colleagues at the Advanced Computing and Simulation Laboratory, Champi, Tharaka, Kamani, Nisal, Charith, Sachinthana, Dilusha, Dasuni, Ravi and Ashan for fruitful discussions and cherishable memories we shared during my time there. I also thank all my friends from Monash for making my PhD journey memorable.

I want to acknowledge facilities and financial support provided by Monash University and the Department of Electrical and Computer Systems Engineering throughout my candidature.

Last but not least, I would like to thank my beloved parents Ranjani Samaraweera and Senevirathne Kulathunge, my sister Ridmika and my wife Samadhi, for their moral and emotional support and unconditional love.

This page intentionally left blank.

Contents

1	Introduction	1
1.1	Background and Motivation	1
1.2	Research Aims and Thesis Scope	2
1.3	Thesis Outline	4
2	Components of Nanohybrids	7
2.1	Surface Plasmons	7
2.2	Localized Surface Plasmon Resonance (LSPR)	9
2.2.1	LSPR dependence on nanoparticle shape	11
2.2.2	LSPR dependence on nanoparticle size	12
2.2.3	LSPR dependence on nanoparticle composition	13
2.2.4	LSPR dependence on the surrounding medium	14
2.3	Different Types of Nanoresonators	15
2.3.1	Metal nanoparticle resonators	15
2.3.2	Characterizing the dielectric function of metals	17
2.3.3	Graphene resonators	19
2.3.4	Characterizing the dielectric function of the graphene	21
2.4	Excitons	22
2.5	Different Types of Emitters Used in Sensing Applications	24
2.5.1	Quantum dots	24
2.5.2	Carbon nanotubes	26
3	Analytical Modelling of a Nanohybrid With an Ellipsoidal Nanoresonator	27
3.1	Overview	27
3.2	Model Description	28
3.3	Formalism	29
3.3.1	Calculation of the NR dipolar response	35
3.4	Importance of Using Ellipsoidal NRs in Nanohybrid Designs	41
3.5	Nanohybrid Scattering Properties	43
3.5.1	Dependence on the aspect ratio of the NR	44
3.5.2	Dependence on the polarization of the external electric field	45
3.5.3	Dependence on the submerging medium permittivity	47

3.5.4	Dependence on the separation distance and the QE dipole moment	48
3.6	Summary and Conclusion	52
4	Scattering Properties of a Nanohybrid with a Spheroidal Nanoshell Resonator	55
4.1	Polarizability and Effective Permittivity of an Ellipsoidal Nanoshell Resonator	56
4.2	Numerical Model Overview	58
4.3	Scattering Spectrum Dependence on the Core to Shell Ratio	59
4.4	Scattering Spectrum Dependence on the Core Material	62
4.5	Scattering Spectrum Dependence on the Shell Material	65
4.6	Scattering Spectrum Dependence on the Medium Permittivity	66
5	Scattering Properties of an All-Carbon Nanohybrid	69
5.1	Introduction	69
5.1.1	Overview of the GNF-CNT nanohybrid system	71
5.1.2	Numerical simulation parameters	72
5.2	Results and Discussion	72
5.2.1	Enhanced scattering intensities of the nanohybrid	73
5.2.2	Scattering spectrum dependence on GNF size, CNT size and interparticle distance	75
5.2.3	Tailoring the scattering properties using Fermi energy level	76
5.2.4	The sensitivity of the scattering properties to the medium permittivity	78
5.3	Summary and Conclusion	78
6	Comparison of the Permittivity Sensing Capabilities of Graphene-based Nanohybrids and Metal Nanoparticle-based Nanohybrids	81
6.1	Overview	81
6.2	Simulation Parameters	82
6.3	Numerical Results and Discussion	83
7	Nanohybrids for Biosensing Applications	89
7.1	Nanohybrid-based <i>in vivo</i> Tumour Detection Procedure	89
7.2	Exploiting Nanohybrid Scattering Properties in Biosensing	91
7.2.1	Tumour detection from the frequency separation of the two peaks	92
7.2.2	Tumour detection from the magnitude of the scattering intensity	95
7.3	Summary and Conclusion	97

8 Contributions and Future work	99
8.1 Summary of Contributions	99
8.2 Suggestions for Future Work	102
Bibliography	107

This page intentionally left blank.

List of Figures

2.1	This figure shows the Lycurgus cup, which is made by glass embedded with noble MNPs. The glass appears red and translucent when illuminated from inside of the cup (a), and green and opaque when illuminated from outside (b).	8
2.2	Formation of localized surface plasmons on a MNP resonator under the influence of an oscillating electrical field.	10
2.3	(a) Illustration of an exciton formation in a QE. The area marked by the dotted region shows the electron-hole quasiparticle where the electron and the hole are attracted to each other by a Coulomb force. (b) Effective two-level system of the QE. The excited level has E_e energy and the ground level has E_g energy.	22
3.1	The schematic of the nanohybrid system.	28
3.2	The LSPR frequency variation of a gold spheroidal NR ($L_x = L_y = 10$ nm) for various aspect ratios. The black, red and blue markers show LSPR frequencies for prolate spheroidal NR ($L_z = 12$ nm), spherical NR ($L_z = 10$ nm) and oblate spheroidal NR ($L_z = 8$ nm), respectively. The red and blue lines correspond to real and imaginary parts of the gold permittivity, respectively. The NR is submerged in a medium with permittivity of $\epsilon_b = 5.45$	42
3.3	The normalized scattering spectra for nanohybrid systems with different NRs. The blue, red and orange lines show scattering spectra for nanohybrids with prolate spheroidal NR, spherical NR, and oblate spheroidal NR, respectively. The dimensions of each NRs are the same as that were used to obtain figure 3.2. All plots are normalized by the maximum scattering intensity value in the figure.	44
3.4	The normalized scattering spectra of the nanohybrid for different polarizations. The blue line shows the scattering spectrum for the parallel polarization and the red line shows the scattering spectrum for the perpendicular polarization. All plots are normalized by the maximum scattering intensity value in the figure.	46

3.5	The normalized scattering intensity variation of the nanohybrid at different external medium permittivities. The blue, red, orange, purple and green lines correspond to scattering spectra for submerging permittivity values $\epsilon_b = 6$, $\epsilon_b = 5.5$, $\epsilon_b = 5$, $\epsilon_b = 4.5$ and $\epsilon_b = 4$, respectively. All plots are normalized by the maximum scattering intensity value in the figure.	47
3.6	(a) Variation of the interaction energy between the NR and the QE (g) for various separation distances. (b) Scattering intensity of the nanohybrid compared to that of the isolated NR for varying separation distances. The y-axis of the graph shows the ratios of the maximum scattering intensity of the nanohybrid to that of the isolated NR at specific distances. The blue line and red line correspond to the values obtained for the nanohybrids comprising QEs with dipole moments $\mu_{QE} = 33.62$ D and $\mu_{QE} = 24.01$ D, respectively.	49
3.7	The normalized scattering intensity of the nanohybrid for different separation distances (L_s). The blue line and red line correspond to the scatterings intensity of the nanohybrids comprising QEs with dipole moments $\mu_{QE} = 33.62$ D and $\mu_{QE} = 24.01$ D. The dashed orange line shows the scattering intensity from the isolated NR. (a) $L_s = 16$ nm (b) $L_s = 28$ nm (c) $L_s = 40$ nm (d) $L_s = 100$ nm.	50
4.1	(a) The ellipsoidal nanoshell resonator. The permittivity values of the core and shell of the resonator are ϵ_1 and ϵ_2 , respectively. The semi-axes dimensions of the core are $L_{x,i}$, $L_{y,i}$ and $L_{z,i}$, and the dimensions of the shell are L_x , L_y and L_z . (b) The effective homogeneous NR with semi-axes dimensions L_x , L_y and L_z	56
4.2	The nanohybrid system with the gold spheroidal nanoshell resonator and the QD. The nanohybrid system is submerged in a medium with relative permittivity $\epsilon_b = 5.45$	58
4.3	(a) and (b) show normalized scattering spectra and ϵ_{eff} variation for different ratio values. The dotted and solid lines in (b) represent the imaginary and real parts of the ϵ_{eff} . The blue, red and orange lines correspond to the core to shell ratio values $r = 0$, $r = 0.5$ and $r = 0.8$, respectively. (c) The maximum scattering intensity values obtained for a range of ratio values. (d) The LSPR frequency variation of the gold nanoshell resonator for different ratio values.	60

4.4	(a) and (b) show normalized scattering spectra and ϵ_{eff} variation for different core materials. The dotted and solid lines in (b) represent the imaginary and real parts of the ϵ_{eff} . The blue, red and orange lines correspond to core materials air (hollow), silica and silicon. (c) The maximum scattering intensity variation of the nanohybrid for a range of core permittivity values. (d) The LSPR frequency variation of the gold nanoshell resonator for different core permittivity values.	62
4.5	The normalized scattering spectra of the nanohybrid for different shell materials. (a) and (c) show the normalized scattering spectra when gold nanoshell resonator is used. (b) and (d) show the normalized scattering spectra when silver nanoshell resonator is used. (c) and (d) depict the scattering intensity surface plots for the entire r and frequency range. All plots are normalized by the maximum intensity peak in the relevant subplot.	64
4.6	The normalized scattering spectra for various medium permittivity values. (a) The normalized scattering spectra when the detuning between the QD and NR is fixed at -30 meV. (b) The normalized scattering spectra when the QD excitation frequency is fixed at 1.43 eV. All plots are normalized by the maximum intensity peak in the relevant subplot.	67
5.1	The schematic diagram of the GNF-CNT nanohybrid system. . . .	71
5.2	The normalized scattering intensity calculated for the parameters specified in section 5.1.2. Red, green and blue solid lines indicate scattering intensities for the GNF-CNT nanohybrid, isolated GNF and isolated semiconducting CNT, respectively.	73
5.3	(a) and (b) show the normalized scattering intensities calculated by varying L_y from 16 nm to 20 nm. The initial L_x/L_y ratio $7/9$ is kept constant during this analysis. (c) and (d) show the normalized scattering intensity calculated by varying the length of the CNT L_{cnt} from 4.5 nm to 8.5 nm. (e) and (f) show the normalized scattering intensity calculated by varying the separation distance L_s between CNT and GNF from 10 nm to 25 nm (Fermi energy maintained at $E_F = 0.96$ eV, which corresponds to a detuning of 5 meV). (g) The colour bar used in the surf plots. (a), (c) and (e) are the line plots of normalized scattering intensities at different values of L_y , L_{cnt} and L_s , respectively. (b), (d) and (f) depict the top view of the colour coded scattering intensity surface plots for the entire L_y , L_{cnt} and L_s range. The dotted lines correspond to the relevant coloured line plots depicted in (a), (c) and (e). All plots are normalized by the maximum intensity peak in the relevant subplot.	74

5.4	(a) and (b) show the normalized scattering intensities calculated by varying Fermi energy of the GNF E_F from 0.95 eV to 0.97 eV. (c) and (d) show the normalized scattering intensities calculated by varying the bath permittivity ϵ_b from 3 to 8. (a) and (c) are the line plots of normalized scattering intensities at different values of E_F and ϵ_b . (b) and (d) depict the top view of the colour coded scattering intensity surface plots for the entire E_F and ϵ_b range. The dotted lines correspond to the relevant coloured line plots depicted in (a) and (c). All plots are normalized by the maximum intensity peak in the relevant subplot.	76
6.1	Nanohybrid systems used in the comparison. (a) MNP-CNT nanohybrid (b) GNF-CNT nanohybrid. Both systems are using the same CNT and are submerged in a dielectric medium with real positive relative permittivity ϵ and excited by a coherent external laser beam E	82
6.2	Scattering spectra of each nanohybrid compared to that of their isolated components. (a) Scattering spectrum of the MNP-CNT nanohybrid for medium permittivity values 4 (solid green line) and 5 (solid purple line). When $\epsilon = 4$, the scattering intensities from the MNP-CNT nanohybrid has no significant enhancement over the isolated MNP resonator scattering intensity values. (b) Scattering spectrum for the GNF-CNT nanohybrid for medium permittivity values 4 (solid green line) and 5 (solid purple line). For both values, scattering intensity values from the GNF-CNT nanohybrid show improvement over that of the isolated GNF resonator. Dotted lines in (a) and (b) show the scattering spectra for the isolated resonators at the corresponding permittivity values. The solid brown lines in (a) and (b) show the scattering spectra for the isolated CNT.	84
6.3	The response of the isolated MNP and the isolated GNF resonators to the medium permittivity variations. (a) The maximum scattering amplitude variation for different medium permittivity values. (b) LSPR frequency variation for different medium permittivity values.	85
6.4	Comparison of the maximum scattering intensity values from the nanohybrid systems (I_{NH}) to that of their constituents for different medium permittivity values, ϵ . (a) and (b) Nanohybrid scattering intensity values compared to that of their isolated CNT (I_{CNT}) and isolated NRs (I_{NR}), respectively. The red lines correspond to the MNP resonator-based nanohybrid (NH_{MNP}) and the black lines correspond to the GNF resonator-based nanohybrid (NH_{GNF}). . . .	86

7.1	Nanohybrid based <i>in vivo</i> tumour detection procedure. (a) Patient with the tumour. (b) Injecting nanohybrid sample to the patient. (c) Nanohybrids are starting to accumulate inside the tumour due to the EPR effect. (d) After some time, most of the nanoparticles are accumulated inside the tumour. (e) The nanohybrids are excited by a light source, and the detected scattering intensities are used for tumour detection.	90
7.2	(a) Artistically illustrated skin cancer on a hand. The tumour area is marked using the red outline. (b) The grayscale pixel intensity values of the tumour region are linearly mapped to permittivity values (5-5.45) and colour coded.	91
7.3	Tumour permittivity reconstruction using the frequency separation of the two peaks in the scattering spectrum of a nanohybrid with a nanoshell resonator and a QD. (a) Scattering spectra of the nanohybrid for medium permittivity values 4.8, 5, 5.2, 5.4 and 5.6. D_p is the frequency separation of the two peaks in the scattering spectrum. The dotted line shows the scattering enhancement at the QD excitation frequency. (b) Variation of the peak frequency separation D_p with the medium permittivity value. (c) Normalized peak frequency separation $D_{p,N}$ variation with the medium permittivity. (d) Reconstruction of the tumour permittivity profile shown in figure 7.2(b) using the externally measurable $D_{p,N}$ values.	93
7.4	Tumour permittivity reconstruction using the scattering intensity from an all-carbon nanohybrid. (a) Normalized scattering spectra of the nanohybrid for medium permittivity values 4.8, 5, 5.2, 5.3, 5.4 and 5.6. (b) Red line shows the normalized peak scattering intensity magnitude (P_N) variation with the medium permittivity value. P_N was calculated using the Eq. (7.2). The dotted line shows $\max(I_N)$ variation with medium permittivity value. (c) Reconstruction of the tumour permittivity profile shown in figure 7.2(b) using the externally measurable scattering intensity values. .	96

This page intentionally left blank.

Chapter 1

Introduction

1.1 Background and Motivation

When a nanoresonator (NR) and a quantum emitter (QE) are under coherent illumination, localized surface plasmon resonances (LSPRs) are generated at the NR and excitons are generated at the QE [1–3]. If the QE and the NR are sufficiently close to each other, due to exciton-plasmon interactions, they act as a single hybrid system which has unique and enhanced optical properties compared to its constituents [4, 5]. The optical properties of these nanohybrid systems are easily tunable using various system parameters such as interparticle distance, resonator size, resonator shape. Because of their remarkable optical properties, nanohybrids hold great potential for a plethora of applications such as metamaterials, optoelectronic devices and sensing applications [4, 6–10].

The scattering properties of a nanohybrid are highly sensitive to the refractive index changes in the surrounding environment. This property can be exploited in sensing applications such as biosensing where the scattering signatures from the nanohybrids can be used to image and detect tumours. However, most of the previous research work has focused on studying the optical properties of nanohybrid systems with spherical metal nanoparticle (MNP) resonators [6, 9, 11, 12]. Modelling and analysing optical properties of nanohybrids with non-spherical nanoparticle resonators can increase the understanding, further development,

and potential applications of nanohybrids.

This thesis theoretically studies the scattering properties of nanohybrid systems with non-spherical NRs and different QEs. It aims to develop a generalised mathematical model using a cavity quantum electrodynamics (cavity QED) based approach to describe the scattering properties of nanohybrids with an ellipsoidal NR coupled to a QE. The mathematical model is highly versatile and can be used to analyse nanohybrids with different NRs such as ellipsoidal, spheroidal, spherical, and disk-shaped NRs. Using the developed analytical model, the research investigates the scattering properties of several nanohybrid designs, including a novel all-carbon nanohybrid system that has enhanced and tunable optical properties. The thesis concludes by discussing the prospect of using nanohybrids as biosensors for the detection and classification of tumours.

1.2 Research Aims and Thesis Scope

Developing an analytical model to describe the scattering properties of a nanohybrid comprising an ellipsoidal nanoresonator coupled to a quantum emitter

In this stage, we aim to develop an analytical model to describe the scattering properties of a nanohybrid system with an ellipsoidal NR and a coupled QE. We use a cavity QED based formalism when deriving the optical response of the nanohybrid where the nanohybrid is modelled as an open quantum system, considering the effects from the external environment. We plan to analyse how scattering properties of a nanohybrid system with a gold spheroidal NR and a quantum dot are affected when the aspect ratio of the resonator is changed. We also aim to perform numerical simulations to investigate how different system parameters influence the scattering properties of the nanohybrid.

Studying the scattering properties of a nanohybrid with a spheroidal metal nanoshell resonator

In this stage, we aim to analyse the scattering properties of a nanohybrid system with a spheroidal metal nanoshell resonator. The LSPR of a solid homogeneous MNP resonator can only be changed by altering its size or material. Therefore, if an application imposes both size limitations and resonance requirements, using homogeneous MNP resonator-based nanohybrids might not be feasible. In this stage, we aim to investigate the possibility of overcoming this limitation by using nanoshell resonators in the nanohybrid designs. The LSPRs of nanoshell resonators can be controlled by changing the core to shell ratio of the resonator. We plan to use an effective permittivity model based on internal homogenization to model the polarizability of a spheroidal metal nanoshell resonator. We aim to investigate how the choice of core and shell materials, core to shell ratio, and bath permittivity affect the scattering properties of the nanohybrid.

Investigating the scattering characteristics of an all-carbon nanohybrid

Due to their remarkable optical and mechanical properties and high biocompatibility, carbon nanotubes (CNTs) and graphene nanoflakes (GNFs) are extensively considered for use in biomedical applications. Therefore, by combining them, we can create a nanohybrid that is highly suitable for biosensing. In this stage, we aim to analyse the scattering properties of a novel all-carbon nanohybrid design where a monolayer GNF resonator is coupled to a single-walled CNT. As LSPR properties of the GNF can be controlled using electrostatic or chemical gating without changing any of the physical dimensions, we expect the scattering properties of the novel all-carbon nanohybrid systems to have a higher tunability than conventional MNP resonator-based nanohybrids. We plan to perform numerical simulations to investigate how CNT and GNF dimensions, the distance between the GNF and the CNT and the Fermi energy level of the GNF affect the

scattering properties of the proposed all-carbon nanohybrid. We also aim to discuss the possibility of using the proposed all-carbon nanohybrid for biosensing applications.

Comparing the permittivity sensing capability of GNF resonator-based nanohybrid and a MNP resonator-based nanohybrid

The permittivity sensing capability of a nanohybrid mainly depends on the type of resonator used inside the nanohybrid. There are a large number of NRs that are being investigated for building nanohybrids. Among these, gold MNP resonators and GNF resonators have been widely studied and found to have desirable properties. The structural and material differences between the two resonators make their optical properties significantly different from each other. In this stage, we aim to compare the permittivity sensing capability of a GNF resonator-based nanohybrid and a MNP resonator-based nanohybrid.

Investigating the prospect of using nanohybrids as biosensors

In the final stage, we aim to investigate the prospect of using nanohybrids as biosensors. Using a simple tumour tissue model, we plan to discuss different ways the scattering properties of nanohybrids can be utilised to obtain the underlying permittivity distribution of a tumour.

1.3 Thesis Outline

This thesis comprises eight Chapters which are organised as follows.

Chapter 1 introduces the thesis topic by presenting the background and motivation for the research followed by the research aims.

Chapter 2 introduces the main components of nanohybrids, the NR and the

QE. First, it provides a brief introduction to surface plasmons and LSPRs. Then it discusses various factors that influence the LSPRs of plasmonic resonators and introduces different NRs used in this work. Next, it provides a short overview of excitons in QEs, followed by a brief introduction to different QEs used in the study.

Chapter 3 presents a detailed analytical modelling of the scattering properties of a nanohybrid with an ellipsoidal NR coupled to a two-level QE. Then, using the developed analytical framework, it shows that scattering properties of a nanohybrid system with a gold spheroidal NR and a quantum dot are highly controllable using various system properties. Finally, the chapter also shows that the scattering properties of the nanohybrid are highly sensitive to the permittivity of the surrounding medium.

Chapter 4 analyses the scattering properties of a nanohybrid system comprises a gold nanoshell resonator and a coupled quantum dot. It shows that by selecting a suitable core to shell ratio, nanohybrids can be designed to operate in the near-infrared regime, which is important for biosensing applications. It also discusses how core to shell ratio, bath permittivity, and choice of shell and core materials affect the scattering properties of the nanohybrid.

Chapter 5 presents a novel all-carbon nanohybrid design where a monolayer GNF resonator is coupled to a CNT. It shows that the scattering properties of all-carbon nanohybrids have better tunability compared to that of nanohybrid systems with conventional MNP resonators. It discusses how different system parameters can be used to manipulate the scattering properties of the all-carbon nanohybrid. Chapter 6 compares the permittivity sensing capability of all-carbon nanohybrids and conventional MNP resonator-based nanohybrids.

Chapter 7 discusses the prospect of using proposed nanohybrids in biosensing applications. It shows how to exploit the frequency separation between the peaks in the scattering spectrum and the scattering intensities of the nanohybrid to re-

construct permittivity profile of a skin tumour. Finally, Chapter 8 summarises the research contributions and provide directions for future research work.

Chapter 2

Components of Nanohybrids

The main constituents of a nanohybrid are the nanoresonator (NR) and the coupled quantum emitter (QE). When the nanohybrid is excited using an external light source, surface plasmons are generated at the NR and excitons are generated at the QE. The interaction between these surface plasmons and excitons is the main reason for the unique properties of nanohybrids. Therefore, to understand the research presented in this thesis, it is crucial to understand the background and basic properties of these components. This chapter provides the essential introduction to surface plasmons, excitons and their properties.

2.1 Surface Plasmons

Surface plasmons are collective oscillations of conduction band electrons at the surfaces of plasmonic materials [1,3]. Surface plasmons have attracted significant research interest due to their remarkable optical properties. Plasmonics, the field dedicated to the study of surface plasmons and related sciences, has emerged as an important field with an enthusiastic research community [13]. Although the popularity of Plasmonics as a scientific field is quite recent, first uses of surface plasmons dates to ancient Romans, where they used noble metal nanoparticle (MNP) embedded glass to manufacture beautiful, colour-changing effects in windows and cups. One of the classic examples is the Lycurgus cup, shown in figure

2.1, which changes colour when illuminated differently. Researchers have found that the main reason behind this colour variation is the nanometre-sized gold and silver particles embedded in the glass. The Lycurgus cup is also considered as one of the earliest uses of nanocomposites by humans [14].



Figure 2.1: This figure shows the Lycurgus cup, which is made by glass embedded with noble MNPs. The glass appears red and translucent when illuminated from inside of the cup (a), and green and opaque when illuminated from outside (b).

Wood reported the first scientific observation of surface plasmons in 1902 where he observed light and dark light distribution from the light reflected from a mirror with a diffraction grating on its surface. However, Wood could not explain this phenomenon and these observations were later referred to as Wood's anomalies [15]. In 1941, Fano was able to explain these anomalies theoretically [16]. However, the term surface plasmons is first used by Stern and Ferrell in 1960 to describe plasma oscillations of a degenerate electron gas of a material surface [17]. In the past few decades, due to the advancements in computational and analytical frameworks and nanoparticle fabrication techniques, many researchers have shown an interest in the field of Plasmonics, resulting in a rapid growth, paving the way to application areas such as nanoscale optoelectronic devices [10, 18], photovoltaic devices [19], metamaterials [20, 21] and sensing [22].

In terms of their propagation characteristics, surface plasmons can be categorised into two, (1) propagating surface plasmons are known as surface plasmon polaritons (SPPs), and (2) non-propagating surface plasmons are known as localized surface plasmons (LSPs) [23]. The SPPs are propagating along the interface between the plasmonic material and the dielectric material. SPPs are excited when phase-matching conditions between the coupling light and the surface-guided mode have been met, which can be achieved by using prisms or by grating interfaces [24]. Exciting LSPs, on the other hand, require much less complexity in optics and can be done by direct illumination [25]. When the nanoparticle size is much smaller than the incident wavelength, LSPs are excited in the nanoparticle which are non-propagating excitations of the conduction band electrons [26].

2.2 Localized Surface Plasmon Resonance (LSPR)

When excited by an external electric field, as shown in figure 2.2, the conduction band electrons of the nanoparticle undergo a displacement from its equilibrium position with respect to the positively charged ions. This generates a Coulomb restoring force that pulls back these electrons to their original position, which creates collective harmonic like oscillations [10,27,28]. The maximum displacement amplitude can be obtained at the resonant frequency, which is known as the localized surface plasmon resonance (LSPR) frequency. At LSPR, the oscillation of the conduction electron cloud generates a dipolar response in the direction parallel to the external electric field [29]. Furthermore, at this frequency, the nanoparticle exhibits highly enhanced scattering and absorption properties along with a strong electric field confinement in and around the nanoparticle [26].

When nanoparticle dimensions are very small compared to the wavelength of the external electric field, an equation can be obtained for the LSP field of the nanoparticle by employing the quasistatic approximation. It has been shown that

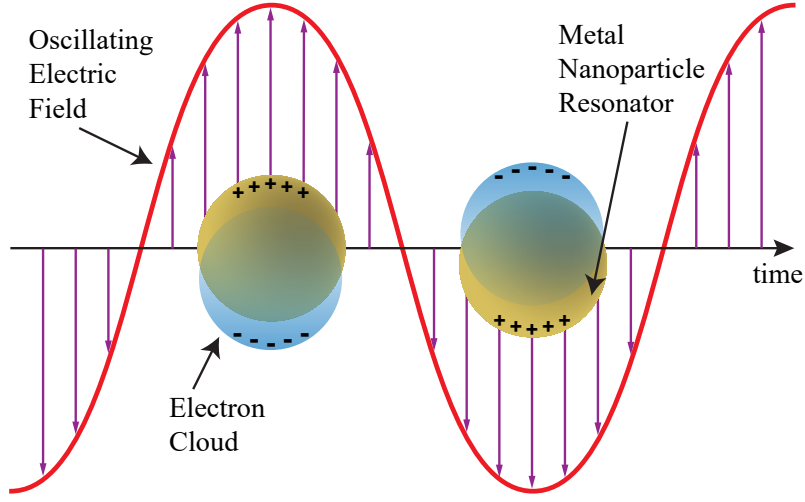


Figure 2.2: Formation of localized surface plasmons on a MNP resonator under the influence of an oscillating electrical field.

for nanoparticles with dimensions less than 100 nm this approximation can yield accurate results [30]. Within this approximation, the external field is constant over the entire nanoparticle volume, so that the system can be solved as a particle in an electrostatic field. In the presence of an external electric field $\vec{E}_0(\lambda)$ the electric field distribution for a spherical nanoparticle with radius a is given by [26],

$$\vec{E}(r) = \begin{cases} \frac{3\epsilon_b}{\epsilon_m + 2\epsilon_b} \vec{E}_0, & \text{for } r < a \\ \vec{E}_0 + \frac{\alpha}{4\pi r^3} \left[3 \left(\vec{E}_0 \cdot \hat{r} \right) \hat{r} - \vec{E}_0 \right], & \text{for } r \geq a \end{cases} \quad (2.1)$$

where ϵ_m is the optical constant of the nanoparticle, α is the polarizability of the nanoparticle, ϵ_b is the relative permittivity of the medium surrounding the nanoparticle, and r is the distance measured from the nanoparticle centre to the point in the electric field. The polarizability of the nanoparticle depends on the geometry of the nanoparticle, and for a spherical nanoparticle it is given by [1, 9],

$$\alpha = 4\pi a^3 \frac{\epsilon_m - \epsilon_b}{\epsilon_m + 2\epsilon_b}. \quad (2.2)$$

When the denominator of the Eq. (2.2) is a minimum, the polarizability un-

dergoes a resonance enhancement. The ε_m of the MNP is a complex, frequency-dependent function. Therefore, when the imaginary part of the ε_m is small, the resonance condition simplifies to the well-known Frölich condition [3]:

$$\text{Re}[\varepsilon_m(\omega)] = -2\varepsilon_b. \quad (2.3)$$

where frequency ω is the LSPR frequency of the nanoparticle. Eq. (2.1) shows that at LSPR frequency, both internal and external dipolar electric fields undergo a resonance enhancement which can be used in sensing applications to detect changes within a few nanometres. Furthermore, by inspecting Eq. (2.2) and Eq. (2.1), the LSPR depends on factors such as shape, size, composition, and the permittivity of the medium surrounding the nanoparticle. Therefore, by selecting suitable parameters, it is possible to tune the LSPR to obtain a frequency response that meets the requirements of a certain application [22, 31].

2.2.1 LSPR dependence on nanoparticle shape

The polarizability of a nanoparticle depends on the shape of the nanoparticle. Eq. (2.2) shows that there is a direct relationship between the polarizability and the LSPR field of a spherical nanoparticle. It has been shown that the nanoparticle shape can influence the position, width, and number of LSPRs of a nanoparticle [32]. The sophisticated fabrication technologies available today have made it possible to synthesise plasmonic nanoparticles with high complexities. For instance, it is possible to fabricate complex metallic nanostructures such as nanorods [33, 34], nanostars [33, 35], nanotubes [36] and nanospheres [37], with highly varying LSPR characteristics. The main motivation for using complex nanostructures is to improve LSPR quality and achieve LSPR tunability [38]. For example, particles like nanorods, spheroidal particles allow LSPR tuning by aspect ratio and the possibility of obtaining LSPR at lower frequencies compared to that of a sphere [27].

LSPR at lower frequencies, particularly in near-infrared regions, is highly useful in biosensing applications.

2.2.2 LSPR dependence on nanoparticle size

The nanoparticle size is another important factor which influences the LSPR. For example, Eq. (2.2) shows that the LSP field outside the spherical nanoparticle depends on its radius. Therefore, the LSP field of the nanoparticle can be controlled by altering the size of the nanoparticle [39]. However, at larger particle sizes, retardation effects become significant [40]. When the nanoparticle is very small compared to the incident field wavelength, the effect of the electric field over the whole volume of the nanoparticle is uniform, and the resulting LSP field has dipolar characteristics [26]. However, when nanoparticle size becomes comparable or even larger than the incident field wavelength, the influence of the electric field is non-uniform over the nanoparticle volume, which results in multipolar LSP excitations [41]. Therefore, in such cases, retardation effects must be taken into consideration. Due to retardation effects, the absorption spectrum of the nanoparticle undergoes spectral broadening and redshift in the LSPR frequency [42].

Moreover, the optical constant of metal nanoparticles has a strong relationship to the particle size [43]. When the size of the nanoparticle is reduced, it becomes comparable to the electron mean free path. This introduces additional losses such as free electron scattering at the nanoparticle surface, which in turn modifies the optical constant of the nanoparticle [44]. Such effects can be incorporated into LSP calculations by using a size-dependent relaxation frequency in the optical permittivity model of the nanoparticle. Finally, nonlocal effects become relevant when the particle size is a few nanometres. These nonlocal effects change the optical constant of the nanoparticle and blueshifts the LSPR frequency [45]. The

nonlocal effects are known as quantum effects because they can only be observed in quantum models and cannot be captured by classical models. Therefore, the LSPR dependence on the particle size is a crucial factor to consider when engineering LSPs for applications.

2.2.3 LSPR dependence on nanoparticle composition

The dielectric function of the nanoparticle depends on its composition. As mentioned earlier, and as shown in Eq. (2.3), the LSPR frequency mainly depends on the dielectric function of the nanoparticle [26]. Therefore, changing the composition of the nanoparticle is another way to control the LSPR properties of the nanoparticle. The trivial way to change the composition is to select different plasmonic materials. In terms of metals, gold and silver are considered as the best available plasmonic materials, and they are utilised in various applications [46]. It is also possible to combine several materials to obtain plasmonic materials with different compositions. The LSPR frequency for a gold-silver alloy nanoparticle would lie somewhere in between the LSPR frequency values corresponding to the pure metals [47]. By changing the percentage of each metal of the alloy, the LSPR frequency of the metal alloy nanoparticle can be tuned. Furthermore, doping is another way to change the composition of a nanoparticle. In graphene resonators, it is possible to change the LSPR by using chemical or electrostatic doping [23]. It has been shown that it is possible to enhance the absorption properties of the nanoparticle in near-infrared frequencies when gold is doped by iron [48]. Therefore, it is possible to utilise nanoparticle composition as a means to obtain a suitable LSP response for different plasmonic applications.

2.2.4 LSPR dependence on the surrounding medium

The LSPR properties are highly sensitive to the changes in the medium surrounding the nanoparticle (see Eq. (2.3)). Due to the nanoscale size of the particles, a higher fraction of the total atoms of the nanoparticle is in the surface and have direct contact with the environment [27]. This makes LSPR of the nanoparticles sensitive even to the minute changes in the surrounding medium. Some studies have found that for some types of nanoparticles, the LSPR frequency has an inverse relationship to the medium permittivity values [49]. When the permittivity value increases, the restoring force applied on the electrons reduces because of the polarisation build up at the dielectric medium surrounding the nanoparticle [50]. This leads to a frequency redshift in both the scattering and absorption spectra of the nanoparticle [49]. Because of these medium sensitive LSP properties, the nanoparticles have been suggested and explored as sensors in chemical and biological sensing applications [50, 51]. For example, in biosensing applications, nanoparticles with a functionalized surfaces can bind with specific molecules and can be used to detect the presence of biological particles, sometimes even at the single-particle level [50]. Furthermore, the medium sensitive scattering spectra of the nanoparticle are also used for imaging and detecting tumours [52, 53]. Therefore, by controlling and utilising LSPR sensitivity to the changes in the surrounding medium, it is possible to realise highly precise and efficient LSPR based sensors for sensing applications.

2.3 Different Types of Nanoresonators

This section discusses different materials that can be used for the resonator in nanohybrid designs.

2.3.1 Metal nanoparticle resonators

There is a large number of metals that are being considered for various plasmonic applications. In particular, gold (Au), Silver (Ag), Copper (Cu), and Aluminium (Al), have attracted a lot of interest due to their favourable optical properties [46]. Among these, gold, silver, and copper are noble metals which have fully occupied d-valence electron bands [54].

The dielectric losses and stability are two main factors consider when choosing a particular metal for a plasmonic application. The Ohmic losses and interband transitions are two leading causes of dielectric losses inside the metal. Among these, losses from interband transitions are caused by bound electrons, which become significant after a critical frequency. Therefore, in applications, it is recommended to operate at LSPR frequencies below this critical frequency. The losses due to electron-ion scattering, electron-electron scattering and other scattering mechanisms due to impurities are collectively identified as Ohmic losses [46]. The damping rate of the metal characterises these Ohmic losses. For plasmonic applications, it is preferable to use a metal with lower damping rate.

Gold and silver are the most frequently used metals in plasmonic applications. Silver has the lowest damping rate among these metals, which implies that it has the lowest losses [46]. Silver is widely used for applications in optical and near-infrared frequencies. However, the main limitations associated with silver are that it degrades relatively quickly compared to gold, and it is challenging to fabricate uniform continuous silver films with few nanometre thicknesses [46]. Gold is the next best metallic plasmonic material after silver, due to its excellent

chemical stability and less toxicity. These properties make gold the ideal material for biomedical applications [55].

However, the cost of these metals is very high compared to the other two metals. Copper is a noble metal which has a high electrical conductivity, inferior only to silver. Also, the cost of copper is relatively cheap compared to gold and silver. These features make copper an attractive alternative for gold and silver for plasmonic applications. The LSPR in copper is narrow and sharp compared to that of the silver and gold. Although it has many desirable properties, oxidation effects which convert Copper to CuO or Cu₂O limit its applicability in plasmonic applications [46].

Aluminium is more suited to use in LSPR applications in ultraviolet frequencies, mainly because in this frequency range, the permittivity of aluminium has a negative real part and a relatively small imaginary part. However, its onset frequency for losses from interband transitions is the lowest among other metals, making it unsuitable for LSPR applications in near-infrared and visible frequencies. Similar to copper, the applicability of aluminium is hindered by oxidation effects which form an oxidation layer (Al₂O₃) quickly when exposed to the atmosphere. Due to this oxide layer, LSPR in aluminium acquires a frequency shift which can be problematic when designing plasmonic applications [56].

Alkali metals like sodium have also been explored for plasmonic applications. The losses in sodium are comparable to that of gold and silver. However, sodium is highly reactive to environments which contain water or air. Therefore, in order to use sodium for applications, highly controlled environments are needed. Due to this reason, plasmonic applications of sodium is mostly limited to theoretical studies [46].

Nobel MNP resonators, mainly gold and silver resonators, have thoroughly studied for their potential applications in chemical and biological sensing. Such applications rely on the medium sensitive LSPR properties of the resonator. For

example, scattering signatures from functionalised gold nanoparticles were used to detect cancer cells [47, 57, 58]. Moreover, the LSPR frequency shifts are also used to detect other living cells and molecules, even at the single particle level. When LSPR changes occur in the visible regime, they can be observed as colour changes that can be used for various sensing applications. Such colorimetric sensing mechanisms are used to detect proteins, DNA, and other organic materials [59–61]. On the other hand, the absorption properties of the MNP resonators have been used in cancer therapeutic applications where the heat generated from MNP resonators is used to destroy cancer cells [62, 63].

2.3.2 Characterizing the dielectric function of metals

The optical properties of a metal are highly dependent on its dielectric function. One of the widely used dielectric functions for metals is the Drude model, where the conduction electrons in the metal are modelled as a gas or plasma which flows in a lattice with fixed positive ions. How this free electron gas responds to external electromagnetic fields governs the optical properties of the metal. The polarization density of the medium \vec{P} and the electric field \vec{E} is related to the displacement field \vec{D} through the following constitute relation

$$\vec{D}(\omega) = \varepsilon_0 \vec{E}(\omega) + \vec{P}(\omega), \quad (2.4)$$

where ε_0 denotes the vacuum permittivity and ω denotes the frequency. Assuming negligible magnetic effects, the polarization density inside the metal can be written as [64],

$$m\ddot{\vec{P}} + m\gamma_0\dot{\vec{P}} = e^2 n \vec{E} \quad (2.5)$$

where n is the electron density in the free electron gas, e is the charge of an electron, m is the effective mass of the electrons and γ_0 is introduced to account

for the damping of electron motion due to collisions with stationary ions. The Drude model do not consider the electron-electron interactions or other impurities present in the metal. By taking the Fourier transform of the Eq. (2.5), an equation for the frequency-dependent polarization density can be obtained. Substituting that in the Eq. (2.4), $\vec{D}(\omega)$ can be obtained as [65]

$$\vec{D}(\omega) = \varepsilon_0 \vec{E}(\omega) - \left(\frac{e^2 n}{m} \right) \frac{1}{\omega^2 + i\gamma_0 \omega} \vec{E} = \varepsilon_0 \overbrace{\left(1 - \frac{\omega_p^2}{\omega^2 + i\gamma_0 \omega} \right)}^{\text{Drude Model}} \vec{E} \quad (2.6)$$

where the plasma frequency (ω_p) is the natural oscillation frequency of the free electron gas, which is defined as

$$\omega_p = \sqrt{\frac{e^2 n}{\varepsilon_0 m}}. \quad (2.7)$$

The Drude model in Eq. (2.6) is derived by assuming no contribution from positive ions. However, there is a constant background electric field arising due to these stationary positive ions. This positive background field can be incorporated into the Drude model by introducing a constant ε_∞ (≥ 1), which compensates for the effects of the positive ions. The modified Drude permittivity ε_D which takes into account the background field of the ions can be written as [64,65],

$$\varepsilon_D(\omega) = \varepsilon_\infty - \frac{\omega_p^2}{\omega^2 + i\gamma_0 \omega}. \quad (2.8)$$

The complex permittivity described by the modified Drude model can be separated into the real and imaginary components as follows.

$$\varepsilon_D(\omega) = \left(\varepsilon_\infty - \frac{\omega_p^2}{\omega^2 + \gamma_0^2} \right) + i \left(\frac{\omega_p^2 \gamma_0}{\omega^3 + \omega \gamma_0^2} \right). \quad (2.9)$$

The imaginary part of the permittivity is associated with the dielectric losses

in the medium. The real part of the permittivity is an indication of the strength of the polarization in the metal caused by an external electric field. When modelling, it is possible to use the analytical equation in Eq. (2.8) or use tabulated experimental permittivity values to obtain the dielectric values of the metals. The experimental work published by Jonson and Christy [66] can be considered as one of the most well-known sources of experimental permittivity values for noble metals. When compared with experimental values, the Drude model can accurately provide permittivity values for frequencies below the interband transition onset frequency. For higher frequencies, the Drude model fails to explain large imaginary values that can be seen in experimental data. The higher imaginary component of permittivity is attributed to the contributions from interband transitions caused by bound electrons that are not included in the Drude model. The Drude-Lorentz model aims to overcome this limitation by adding Lorentz oscillators to the Drude model. The Drude-Lorentz model has the following form,

$$\varepsilon_m(\omega) = \varepsilon_\infty - \frac{\omega_p^2}{\omega^2 + i\gamma_0\omega} - \sum_{m=1}^M \frac{G_m\omega_p^2}{(\omega^2 - \omega_m^2) + i\gamma_m\omega} \quad (2.10)$$

where G_m is the strength, γ_m is the damping constant and ω_m is the resonance frequency of the m^{th} Lorentz oscillator [67]. The dielectric functions discussed so far does not change with the particle size and are fixed for a specific material. However, when particles become smaller, the free electron scattering at the surfaces of the nanoparticles becomes significant, which increases the imaginary part of the permittivity. Such contributions can be accounted for in Drude models by using a size-dependent relaxation frequency [27, 68].

2.3.3 Graphene resonators

Graphene has shown great promise for plasmonic applications since its discovery in 2004 [69]. Before that, no one imagined the possibility of stable free-standing

graphene due to inherent thermal instabilities associated with 2D materials [70]. Graphene is the two-dimensional (2D) allotrope of carbon with a 2D honeycomb lattice structure. Due to its conical band structure, the charge carriers in graphene act as massless Dirac fermions, which are in part responsible for fascinating properties of graphene [23,71]. It has been shown that LSPRs in graphene have a much stronger field confinement than LSPRs in noble MNPs, mainly due to their 2D nature [23]. Furthermore, the LSPRs in graphene are known to have lower losses and higher tunability compared to LSPRs in noble MNPs [72]. Due to its remarkable optical, mechanical, and thermal properties, graphene is being considered for many potential plasmonic applications such as sensing, light-harvesting and metamaterials [23].

A monolayer graphene nanoflake (GNF) resonator can be obtained when a graphene nanosheet is cut into a specific shape. Such resonators can produce LSPRs which are strongly confined compared to that of MNP resonators. When the frequency of the light incident on a noble metal decreases, the imaginary part of the dielectric constant, which accounts for the Ohmic losses, significantly increases [73]. In contrast, owing to the smaller imaginary part and the penetration depth, graphene is more suitable to sustain LSPRs in lower frequencies, especially the infrared regime, which is vital for biosensing applications, in comparison with noble metals [74,75]. When compared to MNP resonators, the LSPR properties of GNF resonators can be easily tuned via electrostatic gating or doping without altering any physical dimensions [76]. However, in MNP resonators, LSPR properties can only be changed by altering its physical properties like size or shape. Therefore, if an application imposes both size and LSPR requirements, GNF resonators are more suitable than MNP resonators.

2.3.4 Characterizing the dielectric function of the graphene

This section provides equations which are used to model the relative permittivity of the monolayer GNF (ϵ_g) in the numerical simulations. The GNF permittivity is related to its frequency dependent three-dimensional (3D) conductivity σ_{3D} as [76],

$$\epsilon_g(\omega) = \left(1 + \frac{i\sigma_{3D}(\omega)}{\omega\epsilon_0} \right), \quad (2.11)$$

where ϵ_0 is the permittivity of the free space. The two-dimensional (2D) conductivity ($\sigma_{2D}(\omega)$) of the GNF can be modeled using the Kubo formula. In the Kubo formalism, $\sigma_{2D}(\omega)$ has contributions from both interband and intraband processes, and can be written as

$$\sigma_{2D}(\omega) = \sigma_{\text{inter}}(\omega) + \sigma_{\text{intra}}(\omega). \quad (2.12)$$

The contribution from intraband conductivity $\sigma_{\text{intra}}(\omega)$ in Eq. (2.12) becomes dominant in the high doping regime where Fermi energy $E_F \gg \hbar\omega$ [77]. The intraband contribution to the 2D conductivity can be expressed as [78,79]

$$\sigma_{\text{intra}}(\omega) = \frac{ie_0^2|E_F|}{\pi\hbar^2(\omega + i\tau^{-1})}, \quad (2.13)$$

where e_0 is the charge of an electron, \hbar is the reduced Planck constant and τ is the intrinsic relaxation time of the carriers in graphene. The, interband conductivity $\sigma_{\text{inter}}(\omega)$ in Eq. (2.12) becomes dominant [77] in the low doping regime where Fermi energy $E_F \ll \hbar\omega$. In Kubo formalism the interband contribution to the 2D conductivity is given by [78]

$$\sigma_{\text{inter}}(\omega) = \frac{ie_0^2}{4\pi\hbar} \ln \left(\frac{2|E_F| - (\omega + i\tau^{-1})\hbar}{2|E_F| + (\omega + i\tau^{-1})\hbar} \right). \quad (2.14)$$

Finally, the three-dimensional (3D) conductivity of graphene which accounts

for the thickness of the graphene flake d can be obtained using the following formula [23,76].

$$\sigma_{3D}(\omega) = \frac{\sigma_{2D}(\omega)}{d}. \quad (2.15)$$

The conductivity equations in Eq. (2.13) and Eq. (2.14) are valid for monolayer GNFs. Various conductivity models for bilayer and multilayer graphene nanoflakes have been proposed in the literature by taking in to account the additional effects such as tunnelling between layers [80–82].

2.4 Excitons

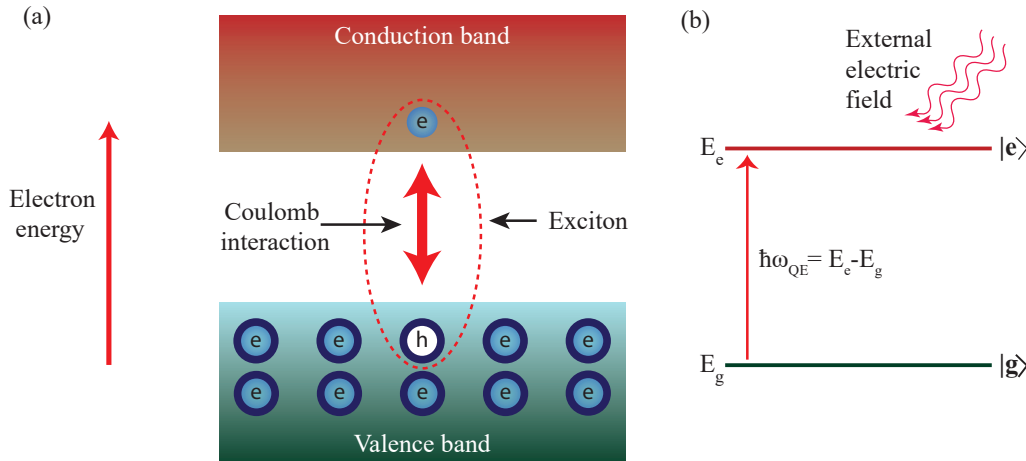


Figure 2.3: (a) Illustration of an exciton formation in a QE. The area marked by the dotted region shows the electron-hole quasiparticle where the electron and the hole are attracted to each other by a Coulomb force. (b) Effective two-level system of the QE. The excited level has E_e energy and the ground level has E_g energy.

When a QE is excited by an external electric field, an exciton is created. In general, QEs have semiconducting properties and have an electronic band structure consisting of a filled valence band and an empty conduction band. The two bands are separated by an energy band gap that prohibits electrons moving from the valence band to the conduction band [83]. If sufficient energy is provided to

the valence band electrons, they can cross the energy band gap and move to the conduction band. As shown in the figure 2.3(a), upon leaving the valence band, an electron leaves behind a hole in the valence band. The negatively charged electron in the conduction band and the corresponding positively charged hole in the valence band are attracted to each other by a Coulomb force [84]. The electrically neutral quasiparticle generated by this bound state of the electron-hole pair is called an exciton [85]. The radiative decay of the exciton leads to recombination of the electron and the hole which causes photoluminescence [86]. Such photoluminescence effects of QEs are exploited in various imaging and sensing applications. Furthermore, excitons are also being used in numerous application areas such as light-harvesting, quantum computing, optoelectronic devices, and exciton transistors [87–91].

As shown in the figure 2.3(b), the excitons in a QE can be modelled as an electronic two-level system. Even though real QEs have many energy levels, the two-level approximation for QEs is widely used in the literature and provides a simple yet extremely useful way to analytically model the excitons. As shown in the figure 2.3(b), the two states of the two-level system are defined as the excited state $|e\rangle$ and the ground state $|g\rangle$. With no excitations, the electrons are residing in the ground state. The energy required to excite an electron from the ground state to the excited state is given by $\hbar\omega_{QE} = (E_e - E_g)$ where E_g is the ground state energy and E_e is the excited state energy. These energies are related to their corresponding states as,

$$\begin{aligned}\hat{\mathcal{H}}|g\rangle &= E_g|g\rangle \\ \hat{\mathcal{H}}|e\rangle &= E_e|e\rangle\end{aligned}\tag{2.16}$$

where the system Hamiltonian, \mathcal{H} , is given by [92],

$$\hat{\mathcal{H}} = E_g|g\rangle\langle g| + E_e|e\rangle\langle e|.\tag{2.17}$$

Since the energy difference between the states is the quantity of interest, the ground state energy (E_g) can be safely set to zero, which modifies the system Hamiltonian to:

$$\hat{\mathcal{H}} = \hbar\omega_{\text{QE}}|e\rangle\langle e| \quad (2.18)$$

Finally, by defining the annihilation operator of the excited state as $\hat{\sigma} = |g\rangle\langle e|$ and its creation operator as $\hat{\sigma}^\dagger = |e\rangle\langle g|$, respectively, the Hamiltonian of the QE can be rewritten as [93],

$$\hat{\mathcal{H}} = \hbar\omega_{\text{QE}}\hat{\sigma}^\dagger\hat{\sigma}. \quad (2.19)$$

As mentioned earlier, in reality, QEs have many more energy levels, however, for closely resonant monochromatic electric fields, the two-level approximation is sufficient, as other levels are far detuned from the field and will not be populated [9].

2.5 Different Types of Emitters Used in Sensing Applications

This section discusses different materials that can be used as the quantum emitters in nanohybrid designs. Among various emitter materials studied in the literature, quantum dots (QDs) and carbon nanotubes (CNTs) have attracted much attention over the past decades for their unique optical and chemical properties.

2.5.1 Quantum dots

Quantum dots are one of the most popular emitters studied in the literature. The QDs have sizes ranging from 1 nm to 10 nm and have distinct optical properties compared to that of bulk materials [86]. The QDs are usually composed of bi-

nary compound materials which are taken from groups II-VI (e.g., CdSe, CdS and ZnSe) and III-V (e.g., GaAs, InP, InSb and GaP) [83]. The band structure of QDs can be controlled using their size, which allows one to tune their optical properties to meet application needs. In terms of fabrication, the colloidal synthesis is more frequently used and can provide QDs with smaller size and better fluorescent properties. In colloidal synthesis, reactions occurring in solutions that contain various ionic or molecular precursors are used to form QDs. Lithography techniques are also available to synthesise QDs, and in these techniques, QDs are fabricated using semiconductor substrates [94]. Unique properties such as high resistance to photobleaching and tunable optical properties make QDs more appealing for fluorescence applications compared to organic dyes which suffer from rapid photobleaching [95].

Recently, there is a significant growth of applications that use QDs for biological imaging and sensing applications [86,95]. The tunable optical properties of QDs in near-infrared frequencies have been used in various *in vivo* applications including imaging of different tissues in the body, tracking and labelling biological cells and imaging tumour cells [86,96,97]. Similarly, *in vitro* applications have used QDs to label and image fixed tissues and cells, which is vital for reliable clinical diagnostics [86]. Due to the high resistance to photobleaching, QD-based imaging techniques can produce images with high contrast and sharpness [98]. Although it is being considered for numerous biological applications, the toxicity of QDs still remains a concern. Various efforts have been made to understand the toxicity of the QDs and find materials with minimal toxicity [99]. Apart from biological applications, QDs have shown promising applications in various fields ranging from quantum computing [100] to light-harvesting [101].

2.5.2 Carbon nanotubes

Carbon nanotubes are made by rolling graphene sheets into cylindrical structures. Due to similar structural properties to graphene, CNTs also exhibit remarkable optical and mechanical properties [102]. Two types of CNTs are multi-walled carbon nanotubes (MWCNTs) and single-walled carbon nanotubes (SWCNTs). MWCNTs have two variants; the first variation is made by rolling a graphene sheet like a newspaper roll in a spiral shape, and the other variation comprises nested SWCNTs [83]. The SWCNTs are defined using chiral vector $\vec{C}_{n,m}$ where n and m are known as chiral indices. The circumference of the CNT is given by $a\sqrt{n^2 + nm + m^2}$ where a is the lattice constant [83]. The optical properties of the SWCNTs are highly dependent on the way they are rolled up, therefore, can be determined by their chiral indices. If $|n - m|$ is a multiple of 3, the CNT has metallic properties, and otherwise, it has semiconducting properties [103,104]. Semiconducting SWCNTs have wide bandgaps which facilitate the formation of excitons that make it possible to use them as QEs in nanohybrid designs [102,105,106]. The most common way to synthesise CNTs is by using carbon vapour deposition (CVD) techniques [107–109].

Due to its extraordinary physicochemical and optical properties such as photoluminescence, high absorption capabilities and tunable surface chemistry, carbon nanotubes have been thoroughly investigated for potential applications in a wide range of diagnostic and therapeutic applications [102,110]. Biosensors based on carbon nanotubes have been used to detect biological molecules, DNA, proteins, and cancer biomarkers [111–115]. Various studies have shown that CNTs can be used for *in vivo* tumour imaging and vascular imaging [116–118]. Furthermore, CNTs are also suggested for targeted drug delivery [119] and hyperthermia therapy [120] applications. Compared to QD emitters, CNTs have shown low cytotoxicity and greater resistance to photobleaching, making them suitable for biosensing applications over QDs [121–124].

Chapter 3

Analytical Modelling of a Nanohybrid With an Ellipsoidal Nanoresonator

3.1 Overview

In this chapter, we develop an analytical model for the scattering properties of a nanohybrid, which comprises an ellipsoidal NR coupled to a QE. This analytical model is used to analyse various nanohybrid designs in subsequent chapters. In this formalism, the nanohybrid system is treated as an open quantum system and take into account its interaction with the external environment. When a nanohybrid is formed by coupling a QE to a NR, it depicts scattering properties that are enhanced and tunable compared to that of its constituents [9, 11]. These unique optical properties are attributed to the exciton-plasmon interactions occurring between the QE and the NR [7]. A cavity quantum electrodynamics (cavity QED) based formalism is used when deriving the optical response of the nanohybrid. This analytical model is highly versatile and can be used to analyse various nanohybrid designs with different NRs with spherical, spheroidal and disk geometries.

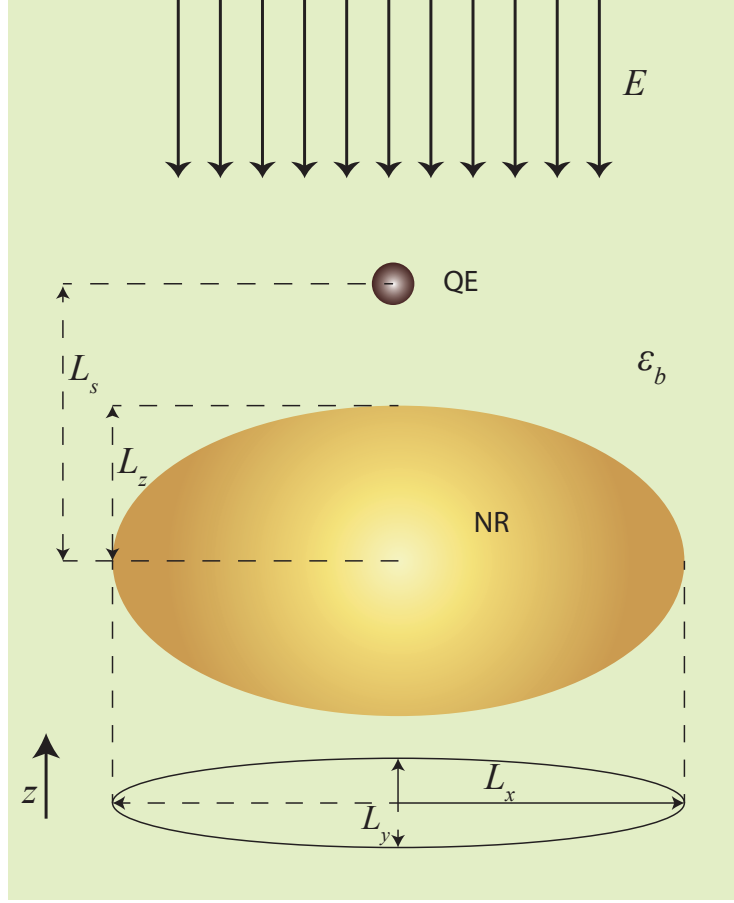


Figure 3.1: The schematic of the nanohybrid system.

3.2 Model Description

A nanohybrid system with an ellipsoidal NR and a QE is considered, as shown in figure 3.1. The system contains a tri-axial ellipsoidal NR with semi-axes dimensions L_x , L_y and L_z . The NR is coupled to a QE, which is modelled as a two-level system, placed L_s distance away from the centre of the NR. The nanohybrid system is submerged in a dielectric medium with a real positive relative permittivity ϵ_b . The minimum distance between the QE and NR surfaces is kept greater than 2 nm to avoid tunnelling effects [4, 11, 30]. A coherent, monochromatic laser beam incident along the z -axis is used to drive the nanohybrid system. The system and the submerging medium are assumed to be non-magnetic. Hence the external

illumination can be modelled with an electric field $E(\omega, t) = \hat{z}E_0(e^{-i\omega t} + e^{i\omega t})$ where ω is the angular frequency, i is the imaginary unit, E_0 is the magnitude of the electric field, t is the time and \hat{z} is the unit vector perpendicular or along the axis of the nanohybrid. It is assumed that both NR and QE undergo dipolar polarization along the direction of external illumination [7,9]. The dimensions of the nanohybrid are significantly smaller than the near-infrared and visible range wavelengths used in many sensing applications. Hence, the quasistatic approximation is used when modelling the optical response of the nanohybrid. [9,11].

3.3 Formalism

This section explains the cavity QED based approach that was used to derive quantum field operators under the influence of the external electric field. The Hamiltonian of the nanohybrid system can be written as

$$\hat{\mathcal{H}} = \hat{\mathcal{H}}_{\text{NR}} + \hat{\mathcal{H}}_{\text{QE}} + \hat{\mathcal{H}}_{\text{NR-QE}} + \hat{\mathcal{H}}_{\text{field}}, \quad (3.1)$$

where $\hat{\mathcal{H}}_{\text{NR}}$, $\hat{\mathcal{H}}_{\text{QE}}$, $\hat{\mathcal{H}}_{\text{field}}$ and $\hat{\mathcal{H}}_{\text{NR-QE}}$ are Hamiltonians for the surface plasmon field of the NR, the two-level QE, the interaction of the nanohybrid system with the external electric field and interaction between the NR and QE, respectively. Next, each of these Hamiltonians are derived separately.

First, we derive the Hamiltonian that describes the surface plasmon field of the NR. Surface plasmons are excited when NR is excited by an external electric field. Here, the surface plasmon field of the NR is quantum mechanically modelled by quantising each mode as a quantum harmonic oscillator. These quantum harmonic oscillators are defined by the corresponding number states and the number of surface plasmons in the particular mode. In the quasistatic regime where particle dimensions are much smaller than the wavelength of the external

electric field, dipole mode corresponds to the LSPR of the NR [4, 125]. Therefore, in calculations, we only consider the dipole mode of the surface plasmon field. Assuming that the energy of the vacuum state is zero, the Hamiltonian for the dipole mode of the surface plasmon field of the NR ($\hat{\mathcal{H}}_{\text{NR}}$) can be written as

$$\hat{\mathcal{H}}_{\text{NR}} = \hbar\omega_{\text{NR}}\hat{a}^\dagger\hat{a}, \quad (3.2)$$

where \hat{a} and \hat{a}^\dagger are the annihilation and creation operators of the dipole mode [93], respectively, and ω_{NR} is the LSPR frequency.

Next, the Hamiltonian is derived for the two-level QE. Excitons are created when the QE is excited using an external electric field with a frequency nearly equal to the frequency separation of the two energy levels. By labelling two energy levels as ground state $|g\rangle$ and excited state $|e\rangle$, the Hamiltonian of the isolated QE ($\hat{\mathcal{H}}_{\text{QE}}$) can be written as $\hat{\mathcal{H}}_{\text{QE}} = E_g |g\rangle \langle g| + E_e |e\rangle \langle e|$ where energy of the ground state is considered to be zero and the energy of the excited state is given by $E_e = \hbar\omega_{\text{QE}}$ with ω_{QE} being the resonant frequency related to the transition between the two states. The raising and lowering operators for the QE can be defined as $\hat{\sigma}^\dagger = |e\rangle \langle g|$ and $\hat{\sigma} = |g\rangle \langle e|$, respectively [93]. Then the Hamiltonian for the two-level QE can be rewritten as

$$\hat{\mathcal{H}}_{\text{QE}} = \hbar\omega_{\text{QE}}\hat{\sigma}^\dagger\hat{\sigma}. \quad (3.3)$$

Let us now obtain an expression for the Hamiltonian describing the dipole-dipole interaction between the NR and the QE. The charge oscillations between the ground state and the excited state, which occur from decays and excitations, create a transition dipole moment in QE. Assuming that the QE transition dipole moment element μ_{QE} is real, the dipole operator for the QE, \hat{d}_{QE} , can be represented as

$$\hat{d}_{\text{QE}} = \hat{d}_{\text{QE}}^- + \hat{d}_{\text{QE}}^+, \quad (3.4)$$

where $\hat{d}_{\text{QE}}^- = \mu_{\text{QE}}\hat{\sigma}^\dagger$ and $\hat{d}_{\text{QE}}^+ = \mu_{\text{QE}}\hat{\sigma}$ denote the negative and positive frequency components that will oscillate as $e^{i\omega t}$ and $e^{-i\omega t}$, respectively, in the interaction picture [126]. The dipole moment in the QE interacts with the dipole mode of the surface plasmon field of the NR. It is assumed that the surface plasmon field radiated by the NR resembles that of a plasmonic cavity [11, 30]. In the cavity QED approach, the positive frequency component of the surface plasmon field operator \hat{E}_{NR}^+ experienced at the centre of the QE can be written as

$$\hat{E}_{\text{NR}}^+ \approx i\mathcal{E}\hat{a}, \quad (3.5)$$

where \mathcal{E} is the electric field amplitude coefficient of the dipole mode of surface plasmon field [11, 127, 128]. Then, the interaction Hamiltonian for QE and the NR, $\hat{\mathcal{H}}_{\text{NR-QE}}$, can be expressed as, $\hat{\mathcal{H}}_{\text{NR-QE}} = -\hat{d}_{\text{QE}} \cdot \hat{E}_{\text{NR}}$ [129, 130]. Substituting \hat{E}_{NR} and \hat{d}_{QE} from Eq. (3.5) and Eq. (3.4), and applying the rotating wave approximation [93], $\hat{\mathcal{H}}_{\text{NR-QE}}$ can be written as

$$\hat{\mathcal{H}}_{\text{NR-QE}} = i\hbar g \left(\hat{\sigma}\hat{a}^\dagger - \hat{\sigma}^\dagger\hat{a} \right), \quad (3.6)$$

where coupling constant for the interaction between the QE and the NR is defined as,

$$g = \frac{\mu_{\text{QE}}\mathcal{E}}{\hbar}. \quad (3.7)$$

The last term of the Hamiltonian in Eq. (3.1) describes the interaction of the external electric field with the induced electric dipole moments of both NR and the QE. The dipole moment operator of the QE is already defined in Eq. (3.4). The induced electric dipole moment in the NR is a result of the displaced charge on its surface. The electric dipole moment operator of the NR \hat{d}_{NR} is given by

$$\hat{d}_{\text{NR}} = \hat{d}_{\text{NR}}^- + \hat{d}_{\text{NR}}^+, \quad (3.8)$$

where $\hat{d}_{\text{NR}}^- = \mu_{\text{NR}} \hat{a}^\dagger$ and $\hat{d}_{\text{NR}}^+ = \mu_{\text{NR}}^* \hat{a}$ denote the negative and positive frequency components of the dipole moment operator of the NR, respectively, with μ_{NR} being the dipole moment element of the NR.

Using dipole moment operators of the NR and the QE, under the dipole approximation, the Hamiltonian for the interaction between the nanohybrid and the external electric field $\hat{\mathcal{H}}_{\text{field}}$ can be written as $\hat{\mathcal{H}}_{\text{field}} = -E(\hat{d}_{\text{NR}} + \hat{d}_{\text{QE}})$. By substituting relevant values and applying the rotating wave approximation, $\hat{\mathcal{H}}_{\text{field}}$ obtained as

$$\hat{\mathcal{H}}_{\text{field}} = -E_0 \left(\mu_{\text{NR}} \hat{a}^\dagger e^{-i\omega t} + \mu_{\text{NR}}^* \hat{a} e^{i\omega t} \right) - \mu_{\text{QE}} E_0 \left(\hat{\sigma}^\dagger e^{-i\omega t} + \hat{\sigma} e^{i\omega t} \right). \quad (3.9)$$

Now we have obtained expressions for all four terms in the system Hamiltonian. Next, this system Hamiltonian is transformed to the interaction picture Hamiltonian. Detunings of the QE and the NR from the external driving field are defined as $\Delta_{\text{NR}} = (\omega_{\text{NR}} - \omega)$ and $\Delta_{\text{QE}} = (\omega_{\text{QE}} - \omega)$, respectively. Using standard transform methods [131], the Hamiltonian in Eq. (3.1) can be transformed to interaction picture Hamiltonian $\hat{\mathcal{H}}_{\text{I}}$ which is in a frame rotating at frequency ω as [4, 132]:

$$\hat{\mathcal{H}}_{\text{I}} = \hbar \Delta_{\text{NR}} \hat{a}^\dagger \hat{a} + \hbar \Delta_{\text{QE}} \hat{\sigma}^\dagger \hat{\sigma} + i\hbar g(\hat{a}^\dagger \hat{\sigma} - \hat{a} \hat{\sigma}^\dagger) - E_0 (\hat{d}_{\text{NR}} + \hat{d}_{\text{QE}}). \quad (3.10)$$

The eigenstates of $\hat{\mathcal{H}}_{\text{I}}$ are dressed states [93, 133] which correspond to the behaviour of the composite system.

The interaction Hamiltonian $\hat{\mathcal{H}}_{\text{I}}$ treats the nanohybrid system as a closed system and it does not take in to account the interactions with the external environment. However, the aim of the nanohybrid based sensors is to sense the surrounding environment. Therefore, it is essential to incorporate effects from the external environment into the model. Furthermore, the steady-state dynamics of the nanohybrid system is mainly dependent on the dielectric properties of the

submerged medium [131]. Therefore, to incorporate dielectric bath effects in the model, the nanohybrid system is modelled as an open quantum system using the Lindblad master equation where interactions with environments are treated as Markovian processes [134]. The Lindblad master equation for the nanohybrid system which takes in to account the effects of external environment can be written as [135]:

$$\frac{\partial}{\partial t}\hat{\rho} = \frac{i}{\hbar} [\hat{\rho}, \hat{\mathcal{H}}_I] + \hat{\mathcal{L}}_{\text{NR}} + \hat{\mathcal{L}}_{\text{QE}}, \quad (3.11)$$

where $\hat{\rho}$ is the density matrix of the nanohybrid system and square brackets denote the commutation operation between the operators. The Liouvillian terms $\hat{\mathcal{L}}_{\text{NR}}$ and $\hat{\mathcal{L}}_{\text{QE}}$ account for the bath induced decays in NR and QE, respectively. Defining γ_{NR} and γ_{QE} as decay rates of the surface plasmon and exciton, respectively, the Liouvillian terms can be derived as [11]:

$$\hat{\mathcal{L}}_{\text{NR}} = \gamma_{\text{NR}} \left(2\hat{a}\hat{\rho}\hat{a}^\dagger - \hat{a}^\dagger\hat{a}\hat{\rho} - \hat{\rho}\hat{a}^\dagger\hat{a} \right) / 2, \quad (3.12)$$

$$\hat{\mathcal{L}}_{\text{QE}} = \gamma_{\text{QE}} \left(2\hat{\sigma}\hat{\rho}\hat{\sigma}^\dagger - \hat{\sigma}^\dagger\hat{\sigma}\hat{\rho} - \hat{\rho}\hat{\sigma}^\dagger\hat{\sigma} \right) / 2. \quad (3.13)$$

Now expectation values are obtained for the quantum operators \hat{a} and $\hat{\sigma}$. In quantum mechanics, the expectation value of any observable ($\hat{\mathcal{O}}$) can be calculated by using the following formula,

$$\langle \hat{\mathcal{O}} \rangle = \text{tr} (\hat{\rho} \hat{\mathcal{O}}), \quad (3.14)$$

where tr denotes the trace of the matrix. In the interaction picture, the time derivative of the expectation value of an operator can be obtained as [131]:

$$\frac{\partial}{\partial t} \langle \hat{\mathcal{O}} \rangle = \text{tr} \left(\hat{\mathcal{O}} \frac{\partial}{\partial t} \hat{\rho} \right). \quad (3.15)$$

Substituting $\hat{\rho}$ from Eq. (3.11) to Eq. (3.15) and assuming that $\langle \hat{\sigma} \rangle$ and $\langle \hat{a} \rangle$ commute with each other [11, 30], the equation of motion for operators \hat{a} and $\hat{\sigma}$

can be obtained as :

$$\frac{\partial}{\partial t} \langle \hat{a} \rangle = \mathcal{M}_{\text{NR}} + g \langle \hat{\sigma} \rangle - \mathcal{D}_{\text{NR}}, \quad (3.16)$$

$$\frac{\partial}{\partial t} \langle \hat{\sigma} \rangle = (2 \langle \hat{\sigma}^\dagger \hat{\sigma} \rangle - 1)(g \langle \hat{a} \rangle - \mathcal{M}_{\text{QE}}) - \mathcal{D}_{\text{QE}}. \quad (3.17)$$

where \mathcal{M}_{NR} , \mathcal{M}_{QE} , \mathcal{D}_{NR} and \mathcal{D}_{QE} are given by

$$\mathcal{M}_{\text{NR}} = i\mu_{\text{NR}}E_0/\hbar, \quad (3.18)$$

$$\mathcal{M}_{\text{QE}} = i\mu_{\text{QE}}E_0/\hbar, \quad (3.19)$$

$$\mathcal{D}_{\text{NR}} = (i\Delta_{\text{NR}} + \gamma_{\text{NR}}/2), \quad (3.20)$$

$$\mathcal{D}_{\text{QE}} = (i\Delta_{\text{QE}} + \gamma_{\text{QE}}/2). \quad (3.21)$$

To derive an expression for the steady state solution for the expectation value of \hat{a} , we make the Eq. (3.16) equal to zero and obtain:

$$\langle \hat{a} \rangle = \frac{\mathcal{M}_{\text{NR}} + g \langle \hat{\sigma} \rangle}{\mathcal{D}_{\text{NR}}}. \quad (3.22)$$

Similarly, to derive an expression for the steady state solution for the expectation value of $\hat{\sigma}$, we make Eq. (3.17) equal to zero and use the fact that in the weak field regime, the excited state population of QE denoted by $\langle \hat{\sigma}^\dagger \hat{\sigma} \rangle$ is negligible [6, 136]. Then, we obtain:

$$\langle \hat{\sigma} \rangle = \frac{\mathcal{M}_{\text{QE}} - g \langle \hat{a} \rangle}{\mathcal{D}_{\text{QE}}}. \quad (3.23)$$

Substituting for $\langle \hat{a} \rangle$ in Eq. (3.23) from Eq. (3.22), the steady state expectation values of $\hat{\sigma}$ can be obtained as,

$$\langle \hat{\sigma} \rangle = \frac{\mathcal{D}_{\text{NR}} \mathcal{M}_{\text{QE}} - g \mathcal{M}_{\text{NR}}}{\mathcal{D} + g^2}. \quad (3.24)$$

where \mathcal{D} is defined as $\mathcal{D}_{\text{QE}}\mathcal{D}_{\text{NR}}$.

Similarly, substituting for $\langle\hat{\sigma}\rangle$ in Eq. (3.22) from Eq. (3.23), the steady state expectation values of \hat{a} can be obtained as,

$$\langle\hat{a}\rangle = \frac{\mathcal{D}_{\text{QE}}\mathcal{M}_{\text{NR}} + g\mathcal{M}_{\text{QE}}}{\mathcal{D} + g^2}. \quad (3.25)$$

3.3.1 Calculation of the NR dipolar response

In this section, expressions for the electric dipole moment element of the NR (μ_{NR}) and the coupling constant for the interaction between the QE and NR (g) are obtained. In the derivation, we use the fact that the expectation values of quantum electric field operators equal to their classical electric field values [137]. First, the electric field components of the NR and QE are classically obtained. In the quasistatic regime, the surface plasmon field generated by the NR is purely electric at the resonance [138]. The QE can be considered as a point dipole source with dipole moment d_{QE} located at a L_s distance from the NR. Therefore, the positive frequency component of the electric field produced by the QE at the NR position is given by

$$E_{\text{QE}}^+ = \frac{s_k d_{\text{QE}}^+}{4\pi\epsilon_0\epsilon_b L_s^3}, \quad (3.26)$$

where s_k is the orientation parameter, d_{QE}^+ is the positive frequency component of the dipole moment of the QE and ϵ_0 is the dielectric permittivity of the free space. The orientation parameter s_k is a scalar whose value depended on the direction of the polarization of the external electric field and the separation vector between the NR and the QE. When the external field is perpendicular to the separation vector $s_k = -1$ and when it is parallel to separation vector $s_k = 2$. Furthermore, k denotes the direction of the external field which can take values x, y or z . For the system shown in figure 3.1, k is equal to z as the external field is parallel to the z -axis.

Similarly, the positive frequency component of the classical electric field produced by the NR at the QE position can be expressed as

$$E_{\text{NR}}^+ = \frac{s_k d_{\text{NR}}^+}{4\pi\epsilon_0\epsilon_b L_s^3}, \quad (3.27)$$

where d_{NR}^+ is the positive frequency component of the dipole moment of the NR. The dipole moment of the NR can be classically obtained using the polarizability of the NR (α_k) as,

$$d_{\text{NR}}^+ = \epsilon_0\epsilon_b\alpha_k E_{\text{i,NR}}^+, \quad (3.28)$$

where $E_{\text{i,NR}}$ is the total electric field at the NR centre, which is given by,

$$E_{\text{i,NR}} = E + E_{\text{QE}}, \quad (3.29)$$

and has contributions from both external electric field and the QE dipole electric field [6,7]. Substituting Eq. (3.29) in Eq. (3.28) and applying relevant values, we obtain,

$$d_{\text{NR}}^+ = \epsilon_0\epsilon_b\alpha_k \left(E_0 + \frac{s_k d_{\text{QE}}^+}{4\pi\epsilon_0\epsilon_b L_s^3} \right). \quad (3.30)$$

In the nanohybrid design, we use an ellipsoidal shaped NR. The advantage of using an ellipsoidal NR is that the resulting analytical model can be used to analyse a wide variety of nanohybrid systems with different NR shapes. For example, the analytical model developed in this section can be directly applied to analyse the optical response of nanohybrid systems with spherical and spheroidal nanoparticles, as shown in the next chapters. Furthermore, the polarizability equation of an ellipsoidal nanoparticle can be used to analyse optical properties of metallic nanodisks [139,140] and graphene nanoflakes [7,141], and the results were found to be in good agreement with experiments [7,139]. The polarizability

of an ellipsoidal NR is defined as,

$$\alpha_k = \frac{4\pi L_x L_y L_z [\varepsilon_{\text{NR}}(\omega) - \varepsilon_b]}{3N_k \varepsilon_{\text{NR}}(\omega) + 3\varepsilon_b [1 - N_k]}, \quad (3.31)$$

where $\varepsilon_{\text{NR}}(\omega)$ is the dielectric permittivity of the NR and N_k is the depolarization (geometrical) factor given by [26, 125, 142, 143]

$$N_k = \frac{L_x L_y L_z}{2} \int_0^\infty \frac{ds}{(L_k^2 + s) \sqrt{(L_x^2 + s)(L_y^2 + s)(L_z^2 + s)}}. \quad (3.32)$$

The three depolarization factors corresponding to the x , y and z axes must satisfy the relation, $N_x + N_y + N_z = 1$. For the special case of a spheroid where L_x and L_y are equal, the depolarization factor along the z -axis can be written as

$$N_z = \frac{1 - e_{\text{NR}}^2}{e_{\text{NR}}^2} \left[\frac{1}{2e_{\text{NR}}} \ln \left(\frac{1 + e_{\text{NR}}}{1 - e_{\text{NR}}} \right) - 1 \right], \quad (3.33)$$

where the eccentricity of the spheroidal NR (e_{NR}) is defined as $1 - 1/r^2$ with the aspect ratio (r) is given by L_z/L_x . For a spheroid, the depolarization factors for x -axis and y -axis directions are equal and given by [7, 125],

$$N_x = N_y = \frac{1 - N_z}{2}. \quad (3.34)$$

Eq. (3.33) and Eq. (3.34) are valid for both prolate ($L_x < L_z$) and oblate ($L_x > L_z$) spheroids.

The classical electric fields which were derived in this section are equal to the expectation values of the quantum field operators [137, 144]. Therefore, by comparing the classical electric field of the NR at the QE position (Eq. 3.27) with the expectation value of the relevant surface plasmon field operator (Eq. 3.5), E_{NR}^+ can be obtained as

$$E_{\text{NR}}^+ = \langle \hat{E}_{\text{NR}}^+ \rangle = i\mathcal{E} \langle \hat{a} \rangle. \quad (3.35)$$

Similarly, by comparing the expectation value of the dipole moment operator for the QE (Eq. 3.4) with its classical counterpart (Eq. 3.26), d_{QE}^+ can be obtained as

$$d_{\text{QE}}^+ = \langle \hat{d}_{\text{QE}}^+ \rangle = \mu_{\text{QE}} \langle \hat{\sigma} \rangle. \quad (3.36)$$

Let us now derive an equation for the coupling constant between the NR and QE. An equation for the positive frequency component of the classical electric field produced by the NR at the QE position E_{NR}^+ can be derived as

$$E_{\text{NR}}^+ = \frac{s_k}{4\pi L_s^3} \left[\alpha_k \left(E_0 + \frac{s_k \mu_{\text{QE}}}{4\pi \epsilon_0 \epsilon_b L_s^3} \langle \hat{\sigma} \rangle \right) \right] \quad (3.37)$$

by substituting Eq. (3.28), Eq. (3.29) and Eq. (3.36) in Eq. (3.27). Another equation for E_{NR}^+ can be obtained as

$$E_{\text{NR}}^+ = \frac{i\mathcal{E}}{\mathcal{D}_{\text{NR}}} \left(\frac{i\mu_{\text{NR}}}{\hbar} E_0 + g \langle \hat{\sigma} \rangle \right), \quad (3.38)$$

by substituting for $\langle \hat{a} \rangle$ in Eq. (3.35) using Eq. (3.25). Comparing the field coefficients of $\langle \hat{\sigma} \rangle$ in Eq. (3.37) and Eq. (3.38), the coupling constant between the NR and the QE can be obtained as,

$$g = \frac{s_k \mu_{\text{QE}}}{4\pi L_s^3} \sqrt{\frac{\alpha_k \mathcal{D}_{\text{NR}}}{i\epsilon_0 \epsilon_b \hbar}}. \quad (3.39)$$

Similarly, by comparing the field components of the external field E_0 in Eq. (3.37) and Eq. (3.38) the dipole moment element of the NR can be obtained as

$$\mu_{\text{NR}} = -\sqrt{i\hbar \epsilon_0 \epsilon_b \alpha_k \mathcal{D}_{\text{NR}}}. \quad (3.40)$$

Using the value of μ_{NR} from above equation and $\langle \hat{a} \rangle$ from Eq. (3.25), an expres-

sion for $\mu_{\text{NR}}\langle\hat{a}\rangle$ can be derived as,

$$\mu_{\text{NR}}\langle\hat{a}\rangle = -\varepsilon_0\varepsilon_b\alpha_k \left(E_0 + \frac{s_k d_{\text{QE}}^+}{4\pi\varepsilon_0\varepsilon_b L_s^3} \right). \quad (3.41)$$

By comparing Eq. (3.41) with Eq. (3.30), it can be seen that $d_{\text{NR}}^+ = -\mu_{\text{NR}}\langle\hat{a}\rangle$. However, an expression for the same quantity can be obtained from Eq. (3.8) as

$$d_{\text{NR}}^+ = \langle\hat{d}_{\text{NR}}^+\rangle = \mu_{\text{NR}}^*\langle\hat{a}\rangle. \quad (3.42)$$

Therefore, the consistency condition for the NR to satisfy the cavity QED model is [11, 30]:

$$\mu_{\text{NR}}^* = -\mu_{\text{NR}}. \quad (3.43)$$

Next, an expression is obtained for μ_{NR} which satisfy this consistency condition. First, we define the real part of the NR permittivity as $\varepsilon'_{\text{NR}}(\omega)$ and the imaginary part of the NR permittivity as $\varepsilon''_{\text{NR}}(\omega)$. In order to have pronounced surface plasmons, the real and imaginary parts of the NR permittivity should satisfy $\varepsilon_{\text{NR}}(\omega)' < 0$ and $\varepsilon''_{\text{NR}}(\omega) \ll -\varepsilon_{\text{NR}}(\omega)'$ conditions. At the LSPR, the polarizability of the NR undergoes a resonant enhancement. When $\varepsilon''_{\text{NR}}$ is small, from the denominator of Eq. (3.31), the real part of the permittivity at LSPR frequency (Ω) can be obtained as,

$$\varepsilon'_{\text{NR}}(\Omega) = -\frac{1 - N_k}{N_k}\varepsilon_b. \quad (3.44)$$

Therefore, if the depolarization values are known, the LSPR can be calculated given that the dielectric permittivity values of the NR are known. For example, for spherically shaped NR, due to the symmetry, N_k in every direction is equal to 1/3. When this value is applied to Eq. (3.44), we obtain $\varepsilon'_{\text{NR}}(\Omega) = -2\varepsilon_b$, which is the well-known Frölich condition [3, 26]. The resonance enhancement of the polarizability at the LSPR is mainly restricted by the magnitude of the imaginary part of the NR permittivity.

Furthermore, the rate of energy loss from the surface plasmon mode is proportional to $\varepsilon''_{\text{NR}}(\omega)$. Due to this energy loss, surface plasmons have a finite lifetime which corresponds to a decay rate (γ_{NR}) at the LSPR frequency. The decay rate can be obtained as [3, 11],

$$\gamma_{\text{NR}} = 2\eta\varepsilon''_{\text{NR}}, \quad (3.45)$$

where $\eta = (d\varepsilon'_{\text{NR}}(\omega)/d\omega)^{-1}|_{\omega = \Omega}$. When dielectric losses in the NR are relatively small, η is positive [3]. When surface plasmons in the NR and external electric field are near resonance, the corresponding detuning value $\Delta_{\text{NR}} \approx 0$. Then Eq. (3.39) and Eq. (3.40) can be simplified using Eq. (3.44) and Eq. (3.45) as,

$$g = \frac{s_k\mu_{\text{QE}}}{L_s^3} \sqrt{\frac{\eta L_x L_y L_z}{4\pi\varepsilon_0\hbar N_k}}, \quad (3.46)$$

$$\mu_{\text{NR}} = -i\varepsilon_b \sqrt{\frac{4\pi\varepsilon_0\hbar\eta L_x L_y L_z}{N_k}}. \quad (3.47)$$

With these analytical results, we have the full analytical model for the nanohybrid system. We emphasise that μ_{NR} , now satisfies the consistency condition in Eq. (3.43). Furthermore, if dielectric permittivity of the NR is known, this analytical model can be used to analyse a range of nanohybrids consisting of NRs with different shapes such as disk-shaped nanoparticles, spherical nanoparticles and spheroidal nanoparticles. In order to demonstrate this, we substitute depolarization values for a spherical NR ($N_k = 1/3$) and $L_x = L_y = L_z = r$ to Eq. (3.46) and Eq. (3.47), and obtain $\mu_{\text{NR}} = -i\varepsilon_b \sqrt{12\pi\varepsilon_0\eta r^3\hbar}$ and $\mathcal{E} = (s_k/L_s^3) \sqrt{3\hbar\eta r^3/4\pi\varepsilon_0}$, which agree with the relevant expressions for a nanohybrid comprising a spherical NR which were obtained in previous studies [4, 11, 30].

Finally, we derive an equation for the Rayleigh scattering from the nanohybrid system. In the quasistatic regime, where Eq. (3.46) and Eq. (3.47) are valid, the coherent Rayleigh scattering component corresponding to the elastic scattering becomes dominant. The scattering intensity of the coherent part of the Rayleigh

scattering from the nanohybrid is proportional to [11, 12]:

$$I \approx |d_{\text{QE}}^+ + d_{\text{NR}}^+|^2 = |\mu_{\text{QE}} \langle \hat{\sigma} \rangle + \mu_{\text{NR}}^* \langle \hat{a} \rangle|^2. \quad (3.48)$$

These analytical equations are used to analyse sensing capabilities of different nanohybrid designs in the following chapters.

3.4 Importance of Using Ellipsoidal NRs in Nanohybrid Designs

The nanohybrid system studied in this chapter comprises an ellipsoidal NR which is coupled to a QE. The ellipsoidal shape is a generalised shape which can represent spheres, spheroids, and even disk-shaped particles. The LSPR of a NR is mainly dependent on its shape and composition. For a spherical NR, due to its symmetry, the depolarization factor (N_k) is 1/3 in any direction. Therefore, according to Eq. (3.44), the LSPR is fixed for a sphere of specific material. However, for a generalised ellipsoidal NR, the axial symmetry is absent, and different N_k values are obtained depending on the dimensions. Therefore, the LSPR frequency of such NR can be changed by varying its aspect ratio.

In order to understand how aspect ratio affects the LSPR frequency of the NR, the LSPR frequency of a gold spheroidal NR was calculated for various L_z values. Spheroid is a special case of an ellipsoidal where two axes have equal lengths. Even though our model can be used to analyse any general type of ellipsoidal NR, we focus our analysis on spheroidal NRs because that makes understanding the physics and relationships much easier. The same analysis can be done for any general ellipsoidal NR as well. When $L_z > L_x, L_y$ the spheroid is called an prolate spheroid and when $L_z < L_x, L_y$ the spheroid is called a oblate spheroid. A sphere is a variant of a spheroid where all dimensions are equal in length ($L_z = L_x = L_y$).

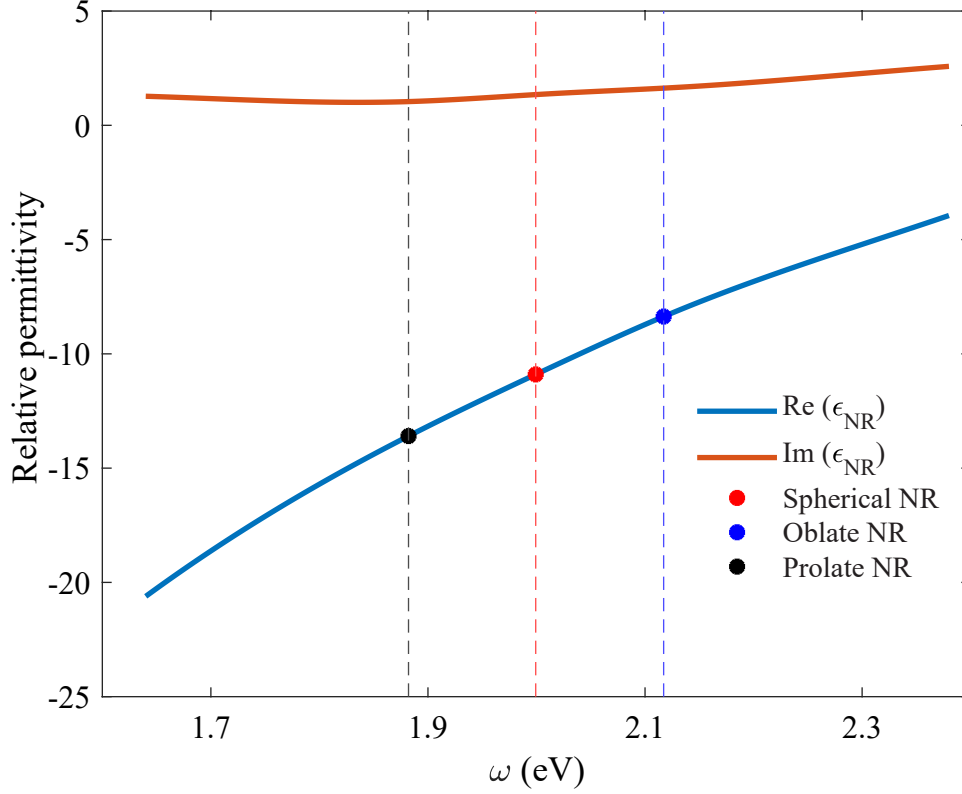


Figure 3.2: The LSPR frequency variation of a gold spheroidal NR ($L_x = L_y = 10$ nm) for various aspect ratios. The black, red and blue markers show LSPR frequencies for prolate spheroidal NR ($L_z = 12$ nm), spherical NR ($L_z = 10$ nm) and oblate spheroidal NR ($L_z = 8$ nm), respectively. The red and blue lines correspond to real and imaginary parts of the gold permittivity, respectively. The NR is submerged in a medium with permittivity of $\epsilon_b = 5.45$.

Figure 3.2 shows the LSPR frequency variation with the L_z for a spheroidal gold NR. Here we have used a spheroid NR with two equal axes $L_x = L_y = 10$ nm which is submerged in a dielectric bath with $\epsilon_b = 5.45$. The experimental permittivity values of gold were used in the simulation [66]. The NR is excited by an external electric field in the z -direction.

The lowest LSPR frequency is obtained for the prolate spheroidal NR which has $L_z = 12$ nm. For these dimensions, N_z is equal to 0.39. If L_z is increased and the NR is made highly prolate, LSPR frequency can be redshifted even further. With its lower N_z value of 0.29, the oblate spheroidal NR has its LSPR frequency

closer to 2.1 eV, which is the highest observed value among these NRs. The N_z value can be decreased even further by reducing L_z , which leads to a further blueshift of the LSPR frequency. The LSPR frequency of the spherical NR lies in the middle. Due to axial symmetry, N_z remains at 0.33 for a sphere of any radius, which makes the LSPR frequency invariant to the size of the NR.

Therefore, the LSPR properties of the ellipsoidal NR can be controlled by changing its aspect ratio. Hence, when an ellipsoidal NR used in a nanohybrid design, the aspect ratio of the NR can be used to control the optical properties of the nanohybrid system. This tunability is not present in the nanohybrid systems which use spherical NRs as they have size invariant LSPR frequencies. Therefore, by using ellipsoidal NRs, nanohybrid systems with tunable optical properties can be constructed. In the next section, we show how various system parameters affect the scattering properties of the nanohybrid.

3.5 Nanohybrid Scattering Properties

The analytical model developed in the previous section can be used to analyse the sensitivity of the nanohybrid scattering properties to various system changes. In this section, we numerically analyse how the scattering properties of the nanohybrid can be controlled by changing different system parameters. This analysis uses the prolate spheroidal NR from the previous section with dimensions $L_x = L_y = 10$ nm and $L_z = 12$ nm. The experimental permittivity of gold is used in the analysis. Quantum dot with decay rate $\gamma_{QE} = 50$ meV and dipole moment $\mu_{QE} = 33.62$ D is used as the QE of the nanohybrid system. The distance between the NR and QE is taken as $L_s = 16$ nm and the orientation parameters is set to $s_k = 2$. The nanohybrid system is excited by an external electric field with an amplitude of 100 Vm^{-1} . The relative permittivity of the submerging medium is $\epsilon_b = 5.45$. In the analysis that follows, these are used as the default parameters

unless mentioned otherwise.

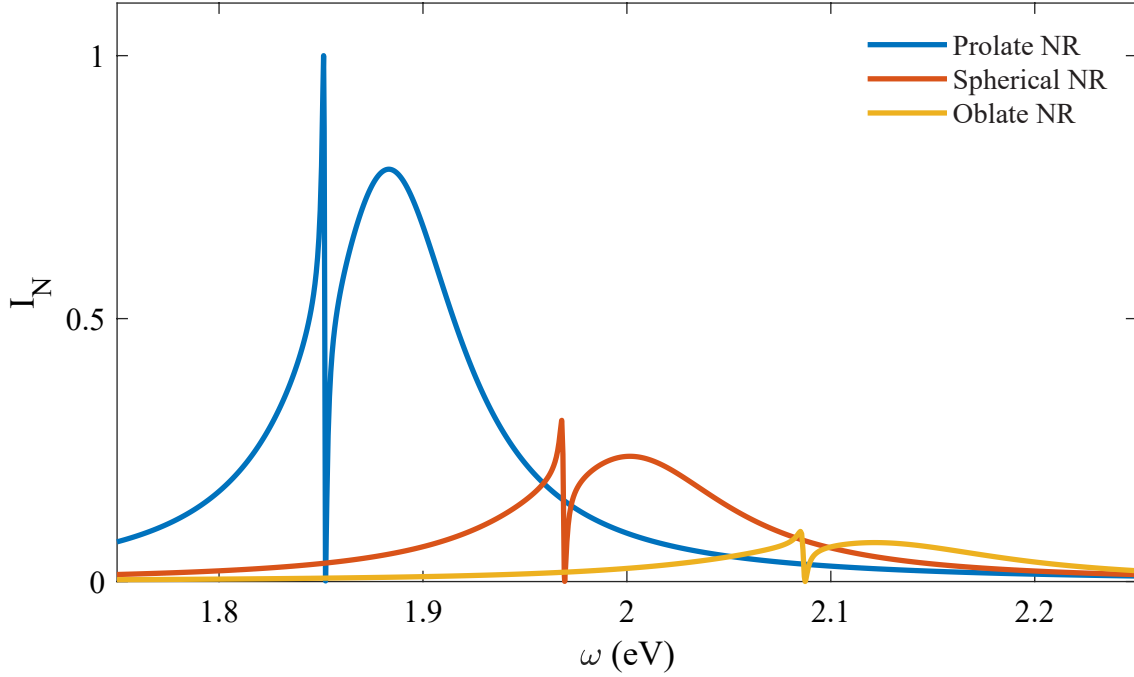


Figure 3.3: The normalized scattering spectra for nanohybrid systems with different NRs. The blue, red and orange lines show scattering spectra for nanohybrids with prolate spheroidal NR, spherical NR, and oblate spheroidal NR, respectively. The dimensions of each NRs are the same as that were used to obtain figure 3.2. All plots are normalized by the maximum scattering intensity value in the figure.

3.5.1 Dependence on the aspect ratio of the NR

Figure 3.3 compares the normalized scattering spectra of three nanohybrid systems which contain the NRs discussed in section 3.4. The blue, red and orange lines show normalized scattering spectra for nanohybrids comprising the prolate spheroidal NR, the spherical NR and the oblate spheroidal NR, respectively.

All scattering spectra show a similar shape, where a Fano-like line shape can be observed around the QE excitation frequency. The asymmetric Fano-like scattering spectrum of the nanohybrid is caused by dipole-dipole interactions between the excitons and the dipole mode of the surface plasmons. The strength

of dipole-dipole interaction is characterized by the coupling constant g , which is defined by Eq. (3.7). Due to these interactions, constructive and destructive interference patterns can be observed in the scattering spectrum of the nanohybrid. The constructive interference causes the scattering enhancement near QE excitation frequency, and the destructive interference causes the suppression of scattering intensity near the QE excitation frequency.

The largest scattering peak intensity is obtained from the nanohybrid with the prolate spheroidal NR. The lowest scattering intensity values are observed from the nanohybrid with oblate spheroidal NR. The nanohybrid with the spherical NR shows a moderate scattering intensity peak compared to the other configurations. With the largest negative real part of dielectric constant at LSPR, the LSPR of the prolate spheroidal NR are more pronounced compared to other NRs which lead to higher scattering intensity values.

Therefore, by changing the aspect ratio of the NR, the scattering peak positions and the corresponding intensity values in the scattering spectrum can be controlled. When the L_z is increased and the NR is made more prolate, the scattering peak not only redshift but has a higher scattering intensity value. Hence, nanohybrid systems which can operate in lower frequencies such as near-infrared frequencies can be achieved with prolate spheroidal NR, which can be useful in various sensing applications.

3.5.2 Dependence on the polarization of the external electric field

The scattering spectrum variations of the nanohybrid with prolate spheroidal NR for different polarizations is shown in figure 3.4. The blue line shows the normalized scattering spectrum when external electric field incident along the axis of the nanohybrid ($s_k = 2$) and the red line shows the scattering spectrum when the incident field is perpendicular to the axis of the nanohybrid ($s_k = -1$). Other than

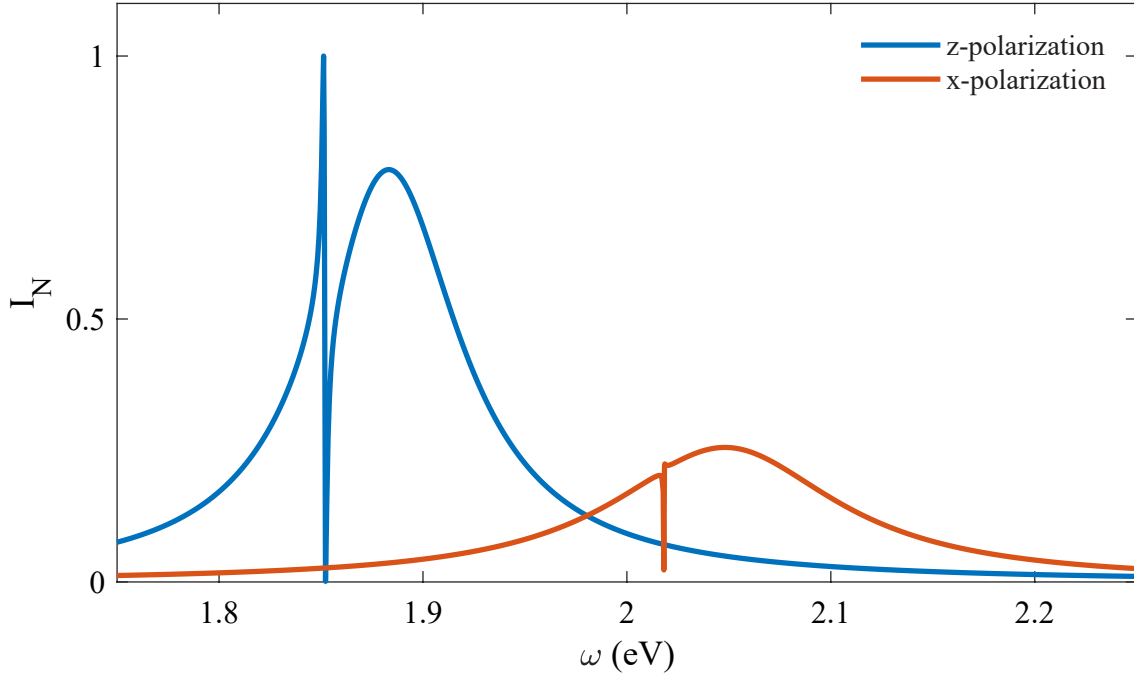


Figure 3.4: The normalized scattering spectra of the nanohybrid for different polarizations. The blue line shows the scattering spectrum for the parallel polarization and the red line shows the scattering spectrum for the perpendicular polarization. All plots are normalized by the maximum scattering intensity value in the figure.

the polarization, all the other parameters take values specified at the beginning of the section 3.5.

It can be observed that the Fano-like line shape, which originates from the dipole-dipole interactions between the QE and the NR is affected by the polarization change. When polarization is parallel to the axis of the nanohybrid, the effect of constructive and destructive interference is clearly visible in the scattering spectrum where a sharp and enhanced scattering intensity peak can be observed. In contrast, when the polarization is perpendicular to the axis of the nanohybrid, the effect from constructive interference is barely visible, and the scattering enhancement is significantly suppressed. Although the effect from destructive interference is present, the dip of the intensity is not significant nor complete compared to the case of parallel polarization.

When perpendicularly polarised, the nanohybrid scattering spectrum undergoes a significant blueshift compared the parallel polarization. This happens because the prolate spheroidal NR has different depolarization factors for the two polarizations ($N_z > N_x, N_y$) which correspond to different LSPR frequencies. The frequency blueshift is absent in nanohybrids with spherical NRs as LSPR frequencies of spherical NRs are invariant to the direction of polarization due to the axial symmetry.

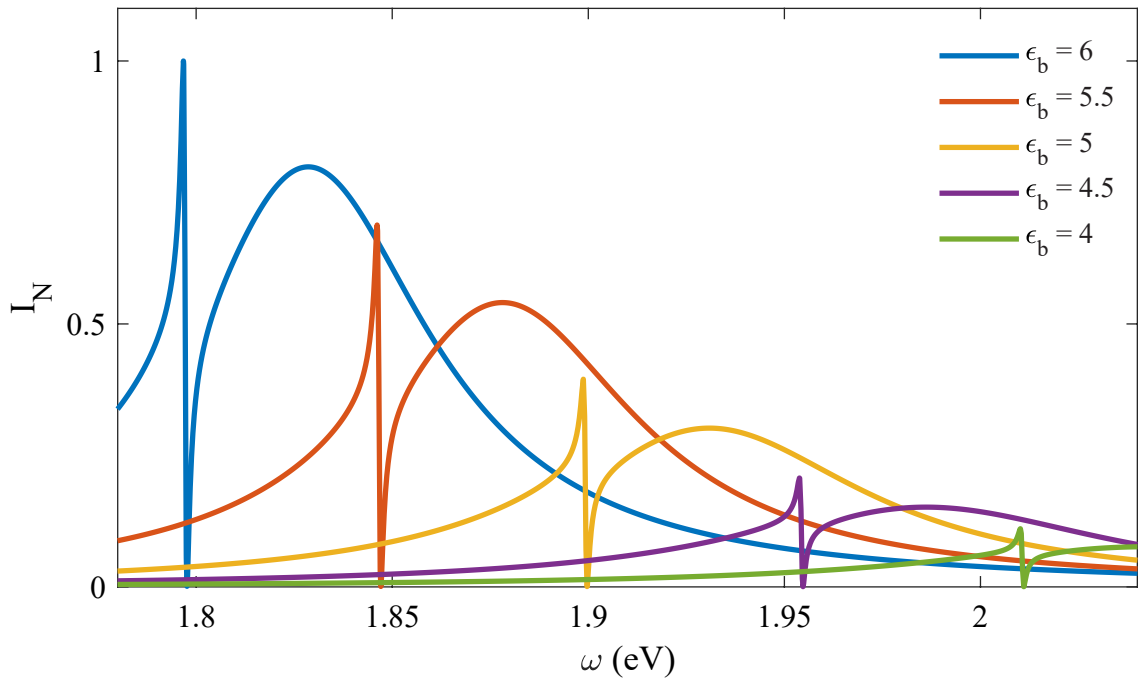


Figure 3.5: The normalized scattering intensity variation of the nanohybrid at different external medium permittivities. The blue, red, orange, purple and green lines correspond to scattering spectra for submerging permittivity values $\epsilon_b = 6$, $\epsilon_b = 5.5$, $\epsilon_b = 5$, $\epsilon_b = 4.5$ and $\epsilon_b = 4$, respectively. All plots are normalized by the maximum scattering intensity value in the figure.

3.5.3 Dependence on the submerging medium permittivity

Figure 3.5 shows how the normalized scattering intensity of the nanohybrid affected by the permittivity variations of the submerging medium permittivity. It

can be observed that when the medium permittivity value increases, the frequency that corresponds to the peak intensity of the scattering spectrum shifts towards lower frequencies. The permittivity change of the submerging medium also affects the magnitude of the peak scattering intensity value that gets amplified with the increasing medium permittivity.

These changes arise due to NR LSPR sensitivity to the medium permittivity. According to Eq. (3.44), the LSPR frequency of the NR highly depends on the submerging medium permittivity. Therefore, as external medium permittivity increases, the LSPR frequency of the NR shifts to lower frequencies which explain the analogous frequency redshift observed in the nanohybrid. Furthermore, as shown in figure 3.2, at lower frequencies, the magnitude of the real part of the gold dielectric constant becomes larger. This leads to more pronounced surface plasmons at the NR that amplify the scattering intensities of the nanohybrid.

The medium sensitive frequency and magnitude variations of the scattering signatures can be used to detect changes in the environment around the nanohybrid. For example, in biosensing, the scattering signatures from nanohybrids can be used to detect the presence of a tumour in a patient. The tumour regions have a higher permittivity value compared to healthy regions of the body that redshift and amplify scattering signatures compared to the scattering signatures coming from healthy parts of the body. If the relationship of the scattering intensity and the medium permittivity is known, the permittivity profile of the tumour can be reconstructed from the scattering signatures that can be used for tumour detection and classifications.

3.5.4 Dependence on the separation distance and the QE dipole moment

Figure 3.7 shows how the scattering spectrum of the nanohybrids changes with the separation distance between the NR and QE. The subfigures 3.7(a), 3.7(b),

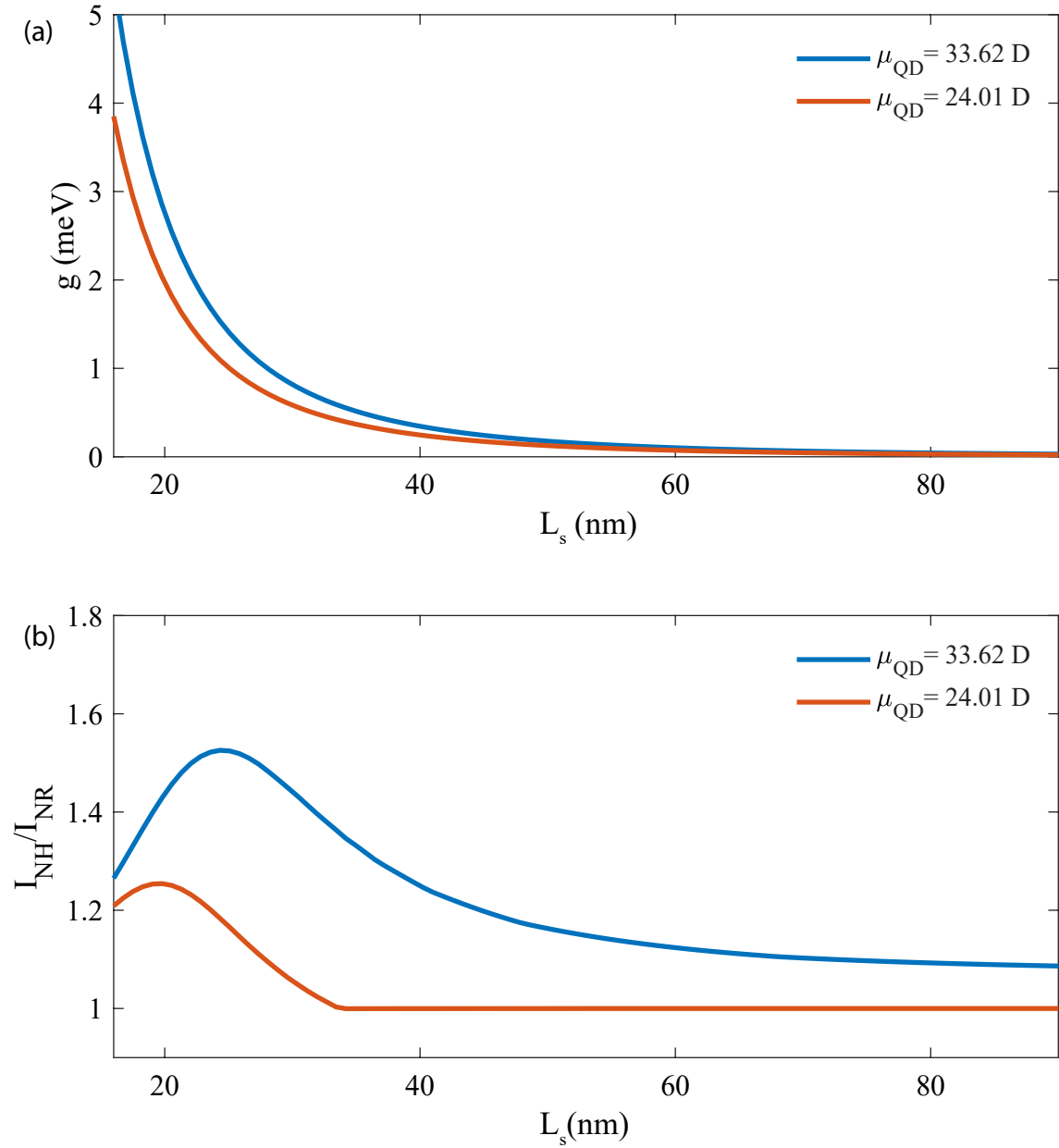


Figure 3.6: (a) Variation of the interaction energy between the NR and the QE (g) for various separation distances. (b) Scattering intensity of the nanohybrid compared to that of the isolated NR for varying separation distances. The y-axis of the graph shows the ratios of the maximum scattering intensity of the nanohybrid to that of the isolated NR at specific distances. The blue line and red line correspond to the values obtained for the nanohybrids comprising QEs with dipole moments $\mu_{\text{QE}} = 33.62 \text{ D}$ and $\mu_{\text{QE}} = 24.01 \text{ D}$, respectively.

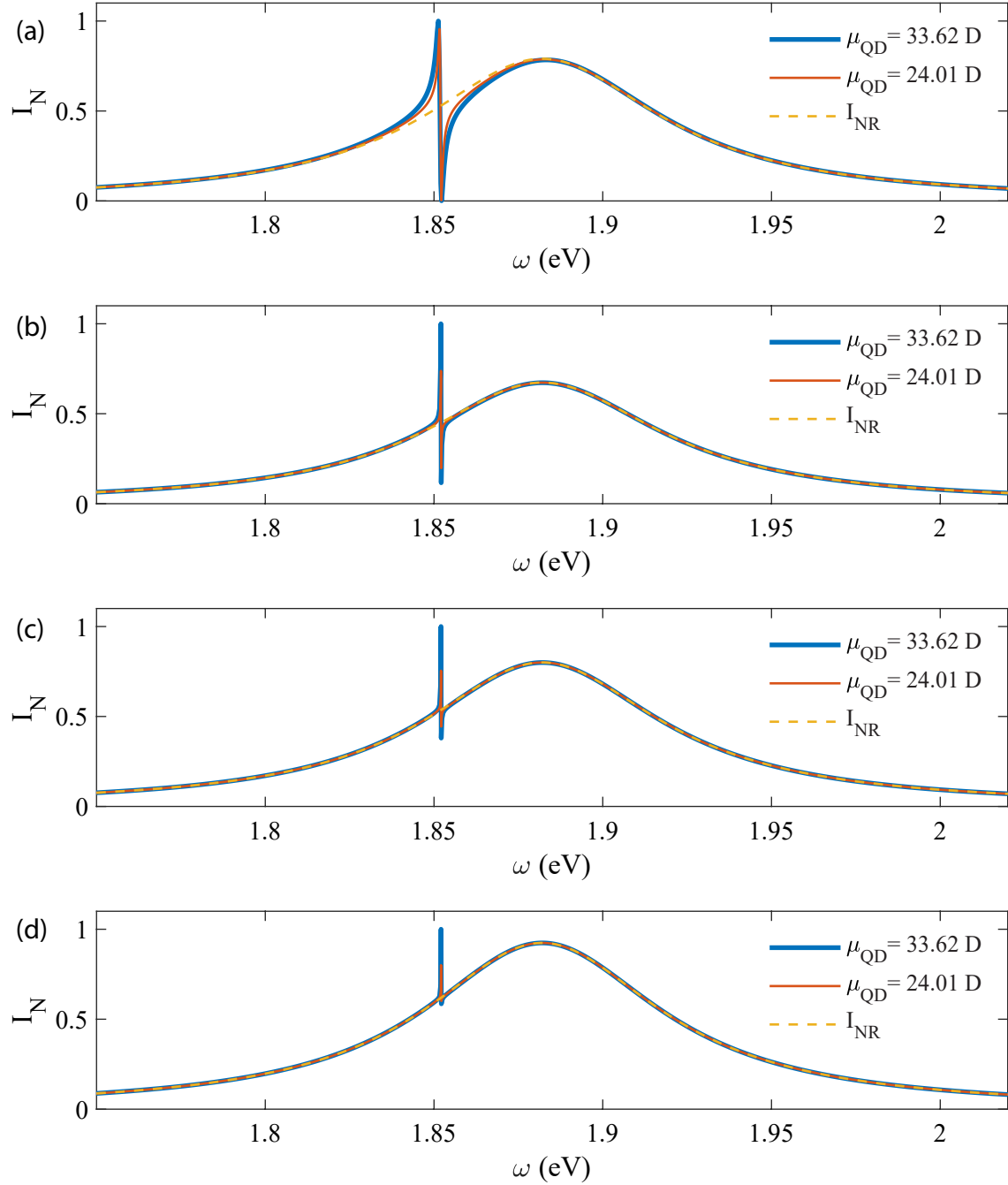


Figure 3.7: The normalized scattering intensity of the nanohybrid for different separation distances (L_s). The blue line and red line correspond to the scatterings intensity of the nanohybrids comprising QEs with dipole moments $\mu_{\text{QE}} = 33.62$ D and $\mu_{\text{QE}} = 24.01$ D. The dashed orange line shows the scattering intensity from the isolated NR. (a) $L_s = 16$ nm (b) $L_s = 28$ nm (c) $L_s = 40$ nm (d) $L_s = 100$ nm.

3.7(c) and 3.7(d) show the scattering spectra for separation distances $L_s = 16$ nm, $L_s = 28$ nm, $L_s = 40$ nm and $L_s = 100$ nm, respectively. Figure 3.6(a) shows how the separation distance affects the interaction energy between the NR and QE. Figure 3.6(b) shows the scattering enhancement of the nanohybrid when compared with the scattering intensity of the isolated NR. The scattering enhancement at a given separation was calculated by taking the ratio of the peak intensity value of scattering spectra of the nanohybrid and the isolated NR at that specific separation distance. The blue and red lines in figure 3.7 and figure 3.6 correspond to values calculated for a nanohybrid containing a QE with a dipole moment $\mu_{QE} = 33.62$ D and a nanohybrid containing a QE with a dipole moment $\mu_{QE} = 24.01$ D, respectively.

The interaction energy has an inverse third power relationship to the separation distance between the NR and QE. Therefore, as shown in figure 3.6(a), the interaction energy reduces significantly when the separation between the NR and QE increases. Figure 3.7(a-c) shows how the scattering spectrum of the nanohybrid changes for different separation distances. When NR and QE are close to each other, the destructive interference dominates the constructive interference, which leads to a larger, broader kink in the scattering spectrum. However, as separation distance increases, constructive interference becomes more substantial compared to its counterpart, which leads to a narrower kink in the scattering spectrum. However, at larger separation distances, the negligible interaction between the NR and the QE results in a scattering spectrum similar to that of the summation of isolated QE and the NR scattering spectra. This is evident from figure 3.6(b) which shows that the scattering enhancement from nanohybrid increases up to an intermediate distance value and beyond that value, it continues to decline to a constant value. Therefore, positioning of the QE and NR controls the scattering enhancement from the nanohybrid and is a crucial factor to consider when designing nanohybrids for applications.

The QE dipole moment (μ_{QE}) has a linear relationship with the interaction energy (g) between the QE and NR. Therefore, as shown in figure 3.6(a), for a given separation distance, QE with the larger dipole moment leads to more interaction energy between the NR and QE. The stronger interactions resulting from the QE with larger dipole moment cause a broader kink in the scattering spectrum, as shown in figure 3.7(a) compared to that for the other QE. Figure 3.6(b) shows that when a QE with a lower dipole moment is used, the maximum scattering enhancement from the nanohybrid can be observed at a shorter distance. In contrast, the much stronger destructive interference originates from the QE with the larger dipole moment is capable of suppressing the scattering enhancement for longer distances. Therefore, this shows that by varying the dipole moment of the QE, the amount and type of interference effects in the nanohybrid scattering spectrum can be controlled.

3.6 Summary and Conclusion

In this chapter, we analytically modelled the scattering properties of a nanohybrid consisting of an ellipsoidal NR and a QE. The nanohybrid system was modelled as an open quantum system, and a cavity QED formalism was used to derive the analytical expressions for the dipole moment operator of the NR and the coupling constant for the interaction between the QE and NR. Then, the derived analytical equations were used to characterise the Rayleigh scattering spectrum of the nanohybrid. The final analytical equations are highly versatile and can be used to analyse scattering properties of nanohybrids with different NRs such as ellipsoidal, spheroidal, spherical and disk-shaped NRs. Next, we performed through numerical simulations to investigate the scattering properties of a nanohybrid with a gold metal spheroidal NR. It was shown that the scattering spectrum of the nanohybrid has an asymmetric Fano-like spectrum as a conse-

quence of the exciton plasmon interactions in the nanohybrid. It was also shown that the nanohybrid scattering signatures are highly sensitive to various parameters like separation distance, QE dipole moment, and the aspect ratio of the NR, which can be used to tune scattering properties of the nanohybrid. Moreover, it was demonstrated that the scattering spectrum is also sensitive to the changes in the medium surrounding the nanohybrid, which can be exploited in sensing applications.

This page intentionally left blank.

Chapter 4

Scattering Properties of a Nanohybrid with a Spheroidal Nanoshell Resonator

The solid, homogeneous metal NRs studied in the previous chapter have limited LSPR tunability as their LSPR can only be varied by changing the aspect ratios and the materials of the NRs, which limits their usability in applications which imposes both size and resonance requirements.

In contrast, the LSPR properties of nanoshell resonators can be changed by varying the core to shell ratio of the resonator. Furthermore, LSPRs of nanoshell resonators can be designed to operate in the near-infrared regime, which is highly relevant in biological applications because of the high tissue penetration observed in these frequencies. Due to these reasons, gold metal nanoshells have been used in numerous *in vivo* biomedical applications. The highly tunable scattering properties of the nanoshells have been used for *in vivo* imaging and sensing applications, and their absorption properties have been used in photothermal cancer therapy applications [145–148]. Therefore, nanohybrids with highly tunable optical properties and operate in the near-infrared regime can be made by incorporating nanoshell resonators in the nanohybrid designs.

This chapter investigates the scattering properties of a nanohybrid with a spheroidal metal nanoshell resonator. The resonator is coupled to a QD which acts as the QE. First, the polarization and the effective permittivity of the nanoshell

resonator is modelled using internal homogenization. Then various numerical simulations are performed to identify key scattering characteristics of the nanohybrid, which can be exploited when designing nanoshell resonator-based nanohybrids for sensing applications.

4.1 Polarizability and Effective Permittivity of an Ellipsoidal Nanoshell Resonator

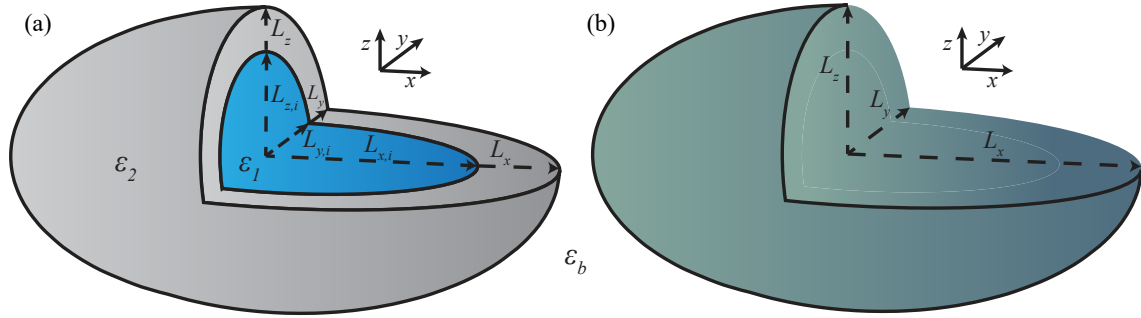


Figure 4.1: (a) The ellipsoidal nanoshell resonator. The permittivity values of the core and shell of the resonator are ϵ_1 and ϵ_2 , respectively. The semi-axes dimensions of the core are $L_{x,i}$, $L_{y,i}$ and $L_{z,i}$, and the dimensions of the shell are L_x , L_y and L_z . (b) The effective homogeneous NR with semi-axes dimensions L_x , L_y and L_z .

The ellipsoidal nanoshell resonator is shown in the figure 4.1(a). The permittivity values of the core and shell of the resonator are ϵ_1 and ϵ_2 , respectively. The semi-axes dimensions of the core are $L_{x,i}$, $L_{y,i}$ and $L_{z,i}$, and the dimensions of the shell are L_x , L_y and L_z . The nanoshell resonator is submerged in a medium with permittivity ϵ_b . In the quasistatic approximation, the polarizability in the k ($k = x, y$ or z) direction of the nanoshell resonator is given by [142],

$$\alpha_k = \frac{4\pi a_2 b_2 c_2 \left((\epsilon_2 - \epsilon_b) \left[\epsilon_2 + (\epsilon_1 - \epsilon_2) \left(N_k^{(i)} - f N_k \right) \right] + f \epsilon_2 (\epsilon_1 - \epsilon_2) \right)}{3 \left(\left[\epsilon_2 + (\epsilon_1 - \epsilon_2) \left(N_k^{(i)} - f N_k \right) \right] [\epsilon_b + (\epsilon_2 - \epsilon_b) N_k] + f N_k \epsilon_2 (\epsilon_1 - \epsilon_2) \right)}, \quad (4.1)$$

where depolarization factors of the inner and outer ellipsoids are given by $N_k^{(i)}$ and N_k , respectively. The f is the core to shell volume ratio of the nanoshell resonator and is given by

$$f = \frac{L_{x,i}L_{y,i}L_{z,i}}{L_xL_yL_z}.$$

Next, the effective permittivity of the ellipsoidal nanoshell resonator is derived using internal homogenization [149]. In the quasistatic regime, where the wavelength of the external electric field is much larger than the dimensions of the NR, the scattered field from the nanoshell resonator is similar to that of an electric dipole. Therefore, the nanoshell resonator can be replaced by a homogeneous NR with an effective permittivity ϵ_{eff} with the same outer dimensions whose polarizability is equivalent to that of the nanoshell resonator [149]. Figure 4.1(b) shows the parameters of the effective homogeneous NR. The dipolar responses of the two NRs are identical as long as they operate in the quasistatic regime. The polarizability of the effective NR is given by

$$\alpha_{k,\text{eff}} = \frac{4\pi L_x L_y L_z [\epsilon_{\text{eff}} - \epsilon_b]}{3N_z \epsilon_{\text{eff}} + 3\epsilon_b [1 - N_k]}, \quad (4.2)$$

which is similar to the Eq. (3.31). By equating the polarizability of the nanoshell resonator to that of the effective NR, the effective permittivity ϵ_{eff} can be obtained as

$$\epsilon_{\text{eff}} = \epsilon_2 \left(1 + \frac{f(\epsilon_1 - \epsilon_2)}{\epsilon_2 + (\epsilon_1 - \epsilon_2) \left(N_k^{(i)} - fN_k \right)} \right). \quad (4.3)$$

Next, the analytical model developed in chapter 3 is used to investigate scattering properties of a nanohybrid with a spheroidal nanoshell resonator and a quantum dot.

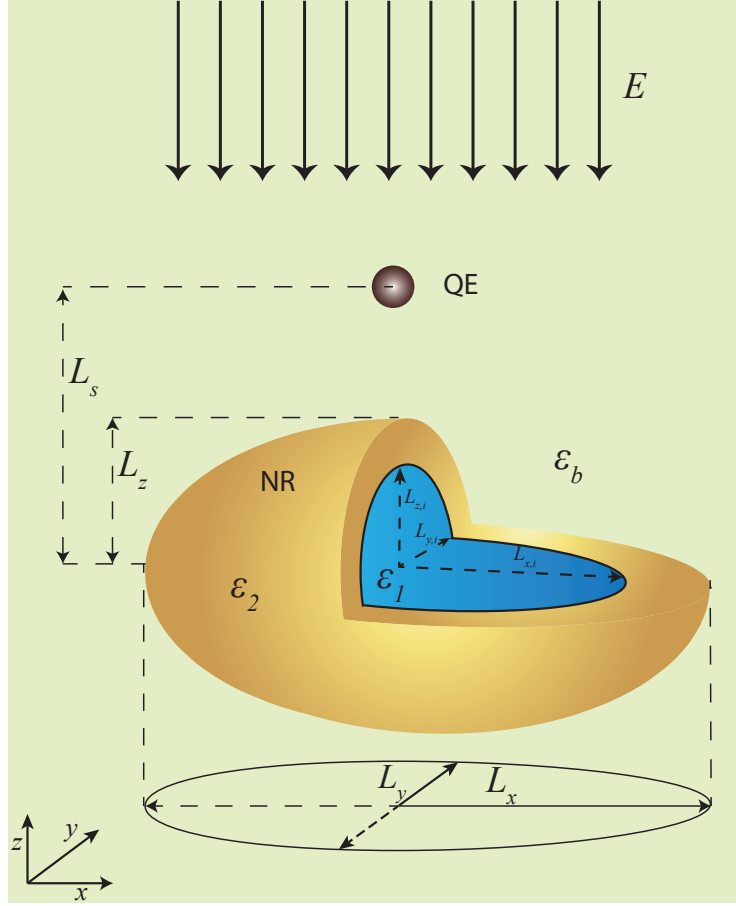


Figure 4.2: The nanohybrid system with the gold spheroidal nanoshell resonator and the QD. The nanohybrid system is submerged in a medium with relative permittivity $\epsilon_b = 5.45$.

4.2 Numerical Model Overview

Figure 4.2 shows the nanohybrid system with the coupled gold spheroidal nanoshell resonator and the QD. The outer dimensions of the NR are $L_x = L_y = 10$ nm and $L_z = 12$ nm. The dimensions of the core are calculated using the core to shell ratio (r), defined as

$$r = \frac{L_{x,i}}{L_x} = \frac{L_{y,i}}{L_y} = \frac{L_{z,i}}{L_z},$$

where $r = 0.7$. The permittivity of the gold is calculated using Drude model (Eq. 2.8) using $\omega_p = 8.7694 \text{ eV}$, $\gamma_0 = 0.0871 \text{ eV}$ and $\epsilon_\infty = 6.2137$ [150]. The QD has a decay rate $\gamma_{QE} = 50 \text{ meV}$ and a dipole moment $\mu_{QE} = 33.62 \text{ D}$. The detuning between the QD and NR is taken as -30 meV . The nanohybrid system is under the influence of an external electric field (E) with an amplitude 100 Vm^{-1} along the z -axis. The distance between the NR and QD is $L_s = 16 \text{ nm}$ and the orientation parameter is $s_k = 2$. The relative permittivity of the submerging medium is $\epsilon_b = 5.45$. In the analysis that follows, these values are used as the default parameter values unless mentioned otherwise.

4.3 Scattering Spectrum Dependence on the Core to Shell Ratio

Figure 4.3(a) shows how core to shell ratio (r) can alter the scattering spectrum of the nanohybrid. The effective permittivity variations of the nanoshell resonator for ratio changes is shown in figure 4.3(b), where solid and dotted lines in the graph represent the real ($\text{Re}(\epsilon_{\text{eff}})$) and the imaginary ($\text{Im}(\epsilon_{\text{eff}})$) parts of the effective permittivity. Figure 4.3(c) shows the maximum scattering value obtained for each of the ratios. Finally, figure 4.3(d) depicts the LSPR frequency variation of the nanoshell resonator for a range of ratio values.

When the core size increases (higher ratio value), the scattering spectrum red-shifts, and the scattering peaks are observed at lower frequencies. However, simultaneously the maximum scattering intensity magnitude obtainable from the nanohybrid decreases, as shown in figure 4.3(c). When the ratio value is increasing, the metallic shell becomes thinner, and the dielectric core size increases. As shown in figure 4.3(b), the ratio change has a substantial effect on the effective permittivity. The $\text{Im}(\epsilon_{\text{eff}})$ is not significantly affected by the ratio changes. However, for a given frequency, the magnitude of the $\text{Re}(\epsilon_{\text{eff}})$ is larger for nanoshell

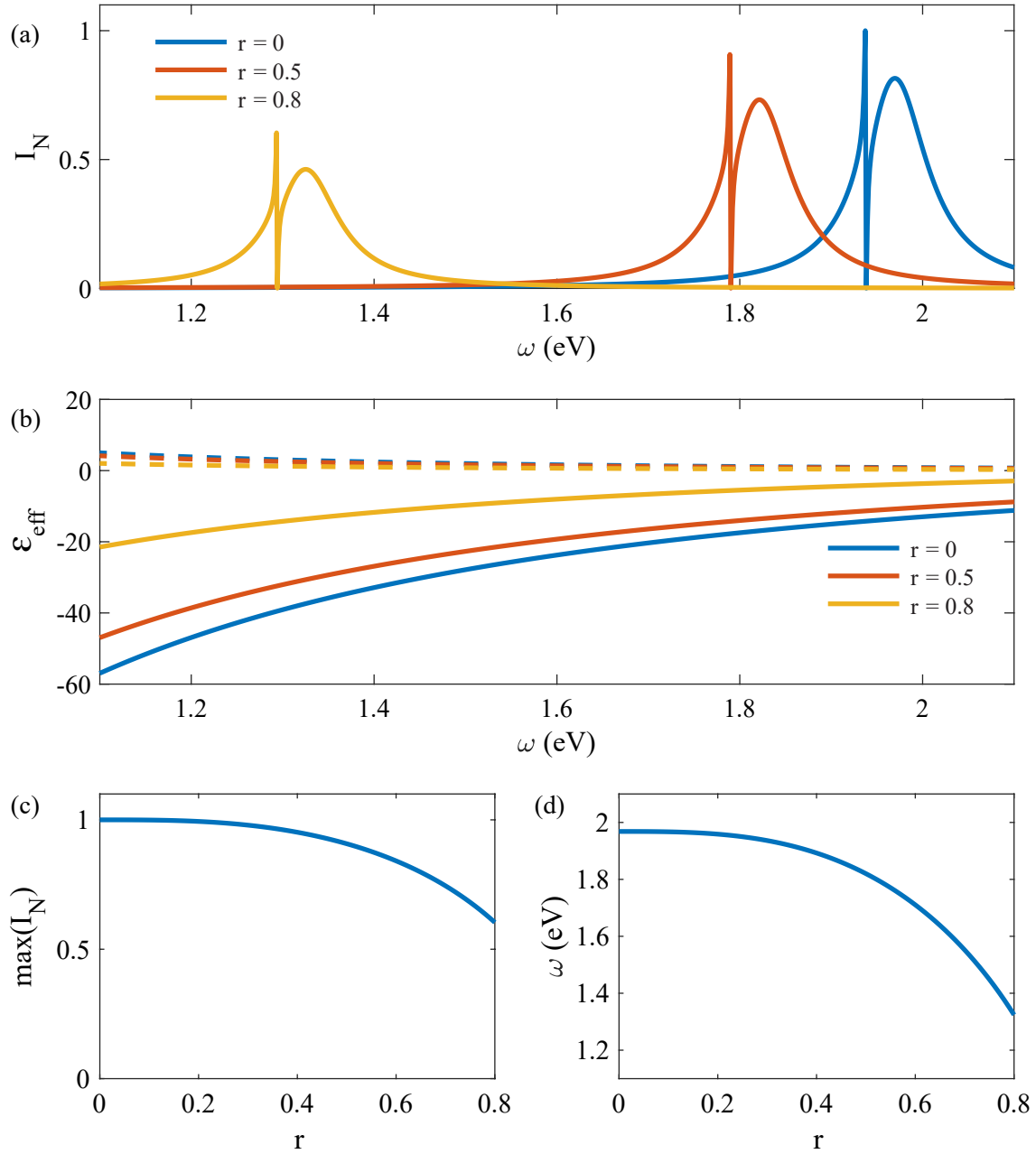


Figure 4.3: (a) and (b) show normalized scattering spectra and ϵ_{eff} variation for different ratio values. The dotted and solid lines in (b) represent the imaginary and real parts of the ϵ_{eff} . The blue, red and orange lines correspond to the core to shell ratio values $r = 0$, $r = 0.5$ and $r = 0.8$, respectively. (c) The maximum scattering intensity values obtained for a range of ratio values. (d) The LSPR frequency variation of the gold nanoshell resonator for different ratio values.

resonators with a thicker shell. The largest negative $\text{Re}(\epsilon_{\text{eff}})$ is observed for the homogeneous NR where the dielectric core is absent. As shown in figure 4.3(d), the LSPR frequency of the nanoshell resonator is susceptible to the changes in the core to shell ratio. When shell thickness is large (smaller ratios), the LSPR frequency is weakly sensitive to the ratio changes. However, when the shell becomes thinner (larger ratios), LSPR frequency becomes highly sensitive to the ratio changes.

The frequency redshift of the intensity peaks in the scattering spectrum shown in figure 4.3(a) can be explained by plasmon hybridization theory. According to plasmon hybridization theory, the nanoshell resonator supports two surface plasmon modes, a low-frequency mode with symmetric charge distribution and a high-frequency mode with antisymmetric charge distribution on the inner and outer surfaces of the metal-dielectric interfaces [151]. When the thickness of the metal shell decreases (r increases), the antisymmetric mode shifts towards higher frequencies and the low-frequency symmetric mode shifts towards lower frequencies. Therefore, when excitons of the QD are coupled to the symmetric plasmon mode of the nanoshell resonator, the nanohybrid scattering spectrum acquires a redshift with the increasing core to shell ratio. By varying the ratio value, it is possible to tune the scattering response of the nanohybrid to lower frequencies such as near-infrared frequencies, which is quite useful in biosensing applications.

As shown in Chapter 3, the only way to tune the LSPR of a homogeneous NR (of a specific material) is by changing its shape or size. However, the LSPR properties of a nanoshell resonator are highly sensitive to the changes of the core to shell ratio. Therefore, it is possible to build nanohybrid systems with tunable scattering properties using nanoshell resonators.

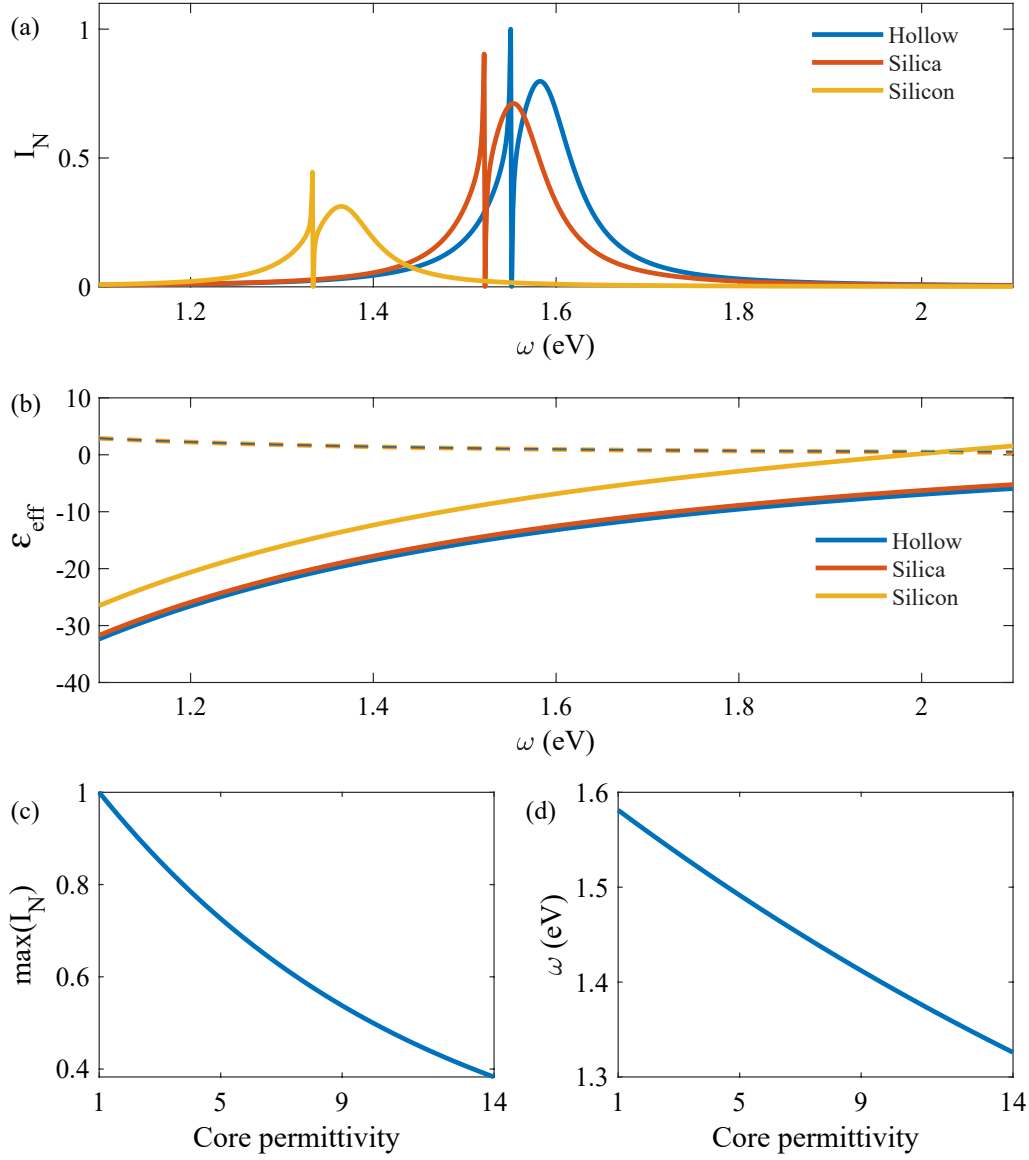


Figure 4.4: (a) and (b) show normalized scattering spectra and ϵ_{eff} variation for different core materials. The dotted and solid lines in (b) represent the imaginary and real parts of the ϵ_{eff} . The blue, red and orange lines correspond to core materials air (hollow), silica and silicon. (c) The maximum scattering intensity variation of the nanohybrid for a range of core permittivity values. (d) The LSPR frequency variation of the gold nanoshell resonator for different core permittivity values.

4.4 Scattering Spectrum Dependence on the Core Material

Variations of the scattering spectra for different core materials are shown in figure 4.4. Subplots (a) and (b) show normalized scattering spectra and ϵ_{eff} variations

when hollow ($n = 1$), silica ($n \approx 1.5$) and silicon ($n \approx 3.4$) used as the core of the nanohybrid. The dotted and solid lines in subplot (b) correspond to the imaginary and real part of the ϵ_{eff} , respectively. Figure 4.3(c) and 4.3(d) show the maximum scattering values of the nanohybrid and the LSPR frequency variation of the NR for a range of core permittivity values.

As shown in the figure 4.4(a), nanohybrid comprising the NR with the hollow core has the highest scattering intensity followed by nanohybrids with silica and the silicon cores. Besides scattering intensity variation, with the increasing core permittivity, a frequency redshift of the scattering spectrum can also be observed. As core materials with real dielectric values are used in the simulation, when the core material is changed, $\text{Im}(\epsilon_{\text{eff}})$ is unaffected. However, the magnitude of the $\text{Re}(\epsilon_{\text{eff}})$ reduces with the increasing core permittivity value. Owing to these changes, as shown in figure 4.3(c), suppression of scattering intensities is observed at larger core permittivity values. Figure 4.3(d) shows that the LSPR frequency of the NR has an approximately inverse linear relationship with the core permittivity. This explains the spectrum redshift observed for larger core permittivity values.

Selecting a suitable core material is an important decision to make when designing a nanohybrid with a nanoshell resonator. If maximum scattering enhancement is the main requirement, hollow nanoshell resonator can be used in the nanohybrid. However, by using core materials with higher permittivity values, the scattering spectrum can be shifted to lower frequencies without changing the core to shell ratio. As both core and shell materials affect the magnitude and the peak positions of the scattering spectrum, they should be carefully selected when designing nanohybrid systems with nanoshell resonators.

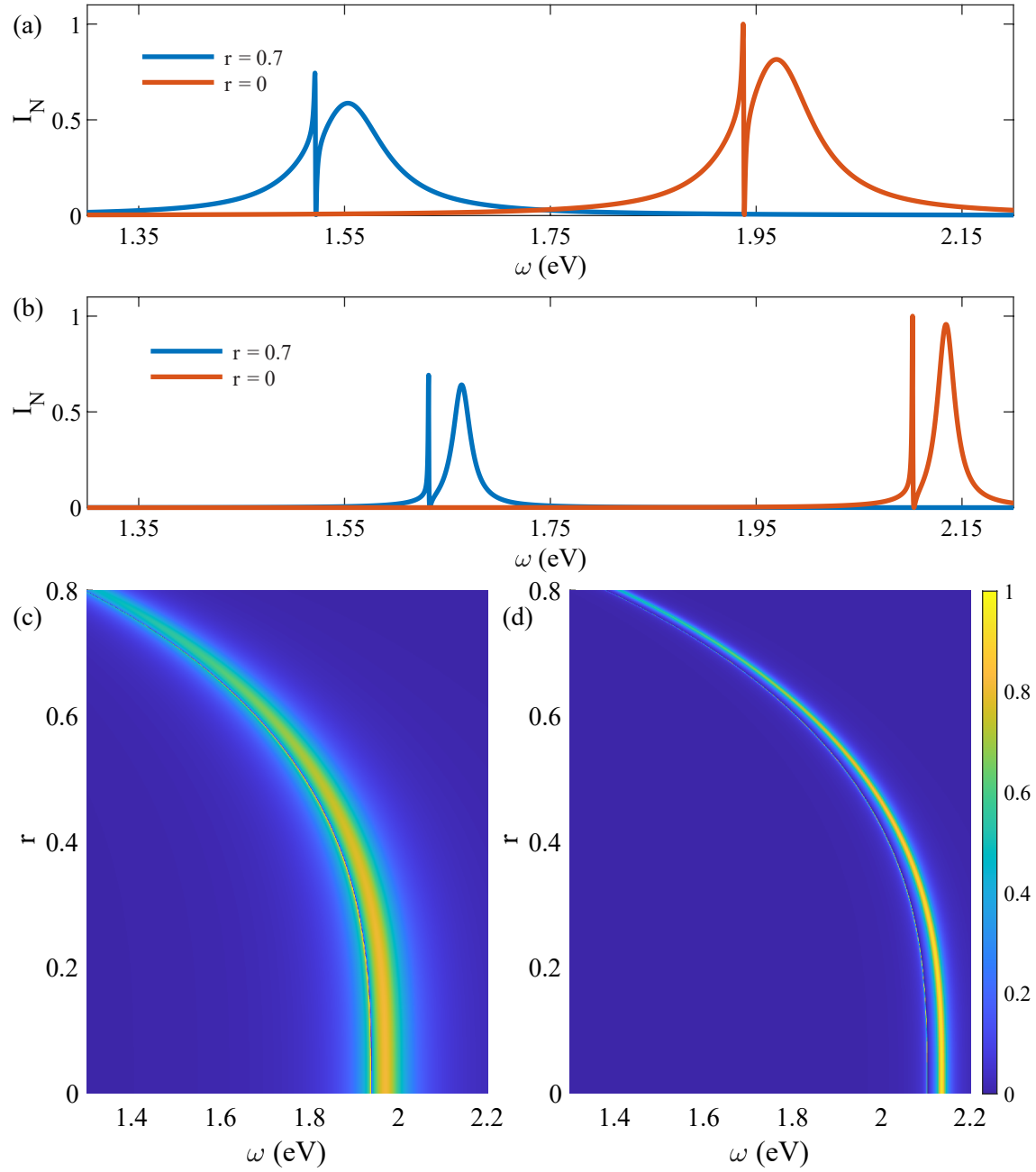


Figure 4.5: The normalized scattering spectra of the nanohybrid for different shell materials. (a) and (c) show the normalized scattering spectra when gold nanoshell resonator is used. (b) and (d) show the normalized scattering spectra when silver nanoshell resonator is used. (c) and (d) depict the scattering intensity surface plots for the entire r and frequency range. All plots are normalized by the maximum intensity peak in the relevant subplot.

4.5 Scattering Spectrum Dependence on the Shell Material

Figure 4.4 compare the scattering properties of nanohybrids that have NRs with different shell materials. The permittivity of the silver is calculated using the Drude model (Eq. (2.8)) using $\omega_p = 9.2 \text{ eV}$, $\gamma_0 = 0.0212 \text{ eV}$ and $\epsilon_\infty = 65$ [149]. As shown figure 4.4(a) and figure 4.4(b), the nanohybrid with the gold nanoshell resonator have broader scattering spectra compared to that of the nanohybrid with the silver nanoshell resonator. Silver is well known for its better plasmonic properties, and it can exhibit more pronounced surface plasmons compared to gold. For the chosen QD detuning, the two peaks in the gold nanoshell based nanohybrid have different intensity values, where the scattering peak at the QD excitation frequency is larger compared to the other peak. In contrast, the intensity peaks in the silver nanoshell-based nanohybrid have approximately equal magnitudes. However, peak scattering intensity magnitudes of the silver nanoshell-based nanohybrid are much larger compared to their gold counterparts.

Moreover, as shown in figure 4.4 (c), due to the broader line shape of the LSPRs of the gold nanoshell resonator, there is a large spectral overlap between the gold nanoshell resonator and QD. This makes it hard to separate the two peaks in the scattering spectrum. However, as LSPRs in the silver nanoshell resonator have a much narrower line shape, the frequency overlap between the NR and the QD is small. As shown in figure 4.4 (d) this makes it easier to distinguish the two peaks in the scattering spectrum of the silver nanoshell based nanohybrid. It is possible to obtain more distinguishable scattering peaks in the gold nanoshell based nanohybrid by increasing the detuning between the NR and the QD.

Due to the high biocompatibility of the gold, the gold nanoshell resonator-based nanohybrids are more suitable for biosensing applications. However, if biocompatibility is not an issue, silver nanoshell resonator-based nanohybrids

can be used to obtain much brighter scattering intensities, and the peaks in the scattering spectrum are more detectable compared to those in the gold nanoshell based nanohybrids.

4.6 Scattering Spectrum Dependence on the Medium Permittivity

This section discusses how the scattering spectrum of the nanohybrid is affected by the medium permittivity variations. Figure 4.6(a) is obtained by keeping the QD detuning from the NR fixed at -30 meV for each permittivity value. When the medium permittivity increases, the maximum scattering intensity of the nanohybrid also increases. This result is similar to the one obtained for the nanohybrid with homogeneous gold NR, except for the positions of scattering peaks. However, in a practical sensing application, it is difficult to change the QD excitation frequency to maintain the detuning at a fixed value.

Figure 4.6(b) shows scattering spectrum variations when the QD excitation frequency is fixed at 1.43 eV. When medium permittivity value is 5, the overlap between the NR and the QD is minimal. Therefore, the magnitude of the scattering peak at the QD excitation frequency is relatively small. However, with the increasing medium permittivity, the detuning between the QD and NR decreases and the NR dipolar electric field magnitude increases. This leads to increased dipole-dipole interactions between the NR and the QD, which causes larger scattering enhancement at the QD excitation frequency. The highest scattering intensity value at the QD excitation frequency is observed when the medium permittivity value is 6.

When compared to the fixed detuning scenario, the varying detuning scenario shown in figure 4.6(b) is more practical. Because after a nanohybrid is fabricated, it is not possible to change the QD excitation frequency. When the QD excitation

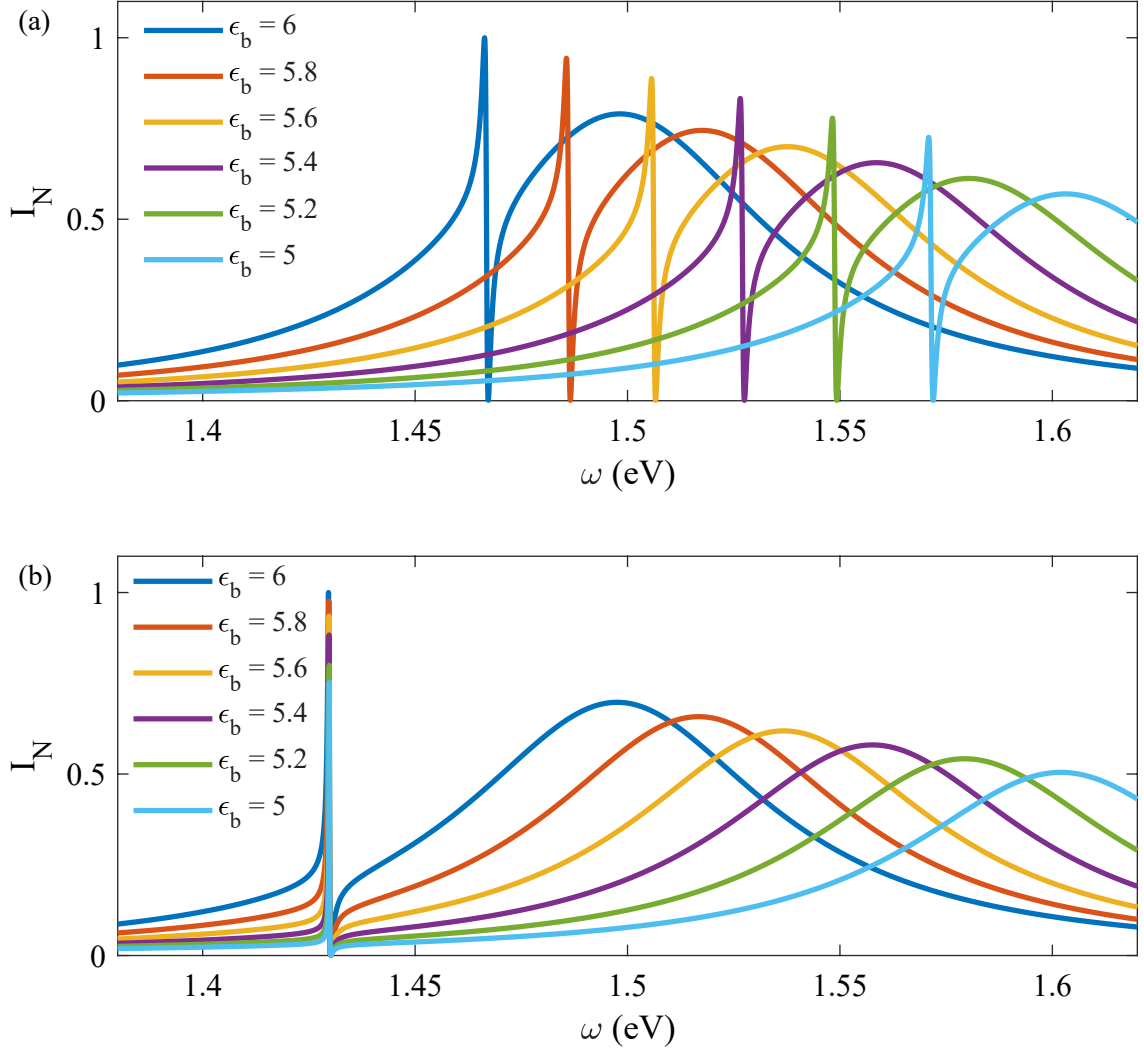


Figure 4.6: The normalized scattering spectra for various medium permittivity values. (a) The normalized scattering spectra when the detuning between the QD and NR is fixed at -30 meV. (b) The normalized scattering spectra when the QD excitation frequency is fixed at 1.43 eV. All plots are normalized by the maximum intensity peak in the relevant subplot.

frequency is fixed, scattering enhancement at the QD excitation frequency can be used to find the underlying medium permittivity. This is more convenient as it is guaranteed that one of the scattering peaks always occurs close to the QD excitation frequency. And as QD excitation frequency is fixed, it is easier to measure the scattering intensity of the peak, unlike the case shown in the Figure

4.6(a) where QD excitation frequency is varying. Therefore, when designing a nanohybrid, it is essential to find a QE with an excitation frequency which is suitable for the requirements of the sensing application.

Chapter 5

Scattering Properties of an All-Carbon Nanohybrid

5.1 Introduction

In Chapter 3 and Chapter 4, optical properties of nanohybrid designs with MNP resonators were analysed. However, the only way available us to change the LSPR of an MNP resonator is to change its size, shape, material or other structural properties. Furthermore, MNP resonators suffer from relatively large ohmic losses [23]. This is evident at lower frequencies, where the imaginary part of the dielectric constant of MNP resonators which accounts for the ohmic losses, becomes significant [73]. These limitations of MNP resonators can restrict the usability and tunability aspects of MNP-QD nanohybrids.

Graphene nanoflake (GNF) resonators, due to their remarkable optical and mechanical properties, are a promising alternative to MNP resonators in nanohybrid systems [23]. In the THz frequency range, GNF resonators are more suited for surface plasmon applications than MNP resonators [74, 152]. It is possible to change the LSPR properties of a GNF resonator via electrostatic or chemical gating [74, 153] without altering its dimensions. These features combined with the high biocompatibility [123, 154] make GNF resonator an ideal candidate for the resonator in nanohybrid systems. When compared to QD emitters used in conventional MNP-QD nanohybrids, carbon nanotubes have shown low cytotoxic-

ity issues, making them suitable for biosensing applications over QDs [121–123]. Furthermore, both graphene and CNTs have also shown greater resistance to photobleaching compared to MNPs and QDs [123, 124].

There is an increasing experimental research interest in fabricating nanohybrids made by combining graphene flakes to CNTs. The first experimental realisation of graphene-CNT nanohybrids was reported by Kondo, where a multilayered graphene sheet is self-assembled perpendicularly to multi-walled CNTs using chemical vapour deposition (CVD) [155]. Similarly, vertically aligned CNTs have been grown on top of a monolayer or few-layer graphene using CVD [156]. Among various fabrication methods [157–160] that can be used to create graphene-CNT nanohybrids, CVD approaches provide structures with better stability and mechanical strength [161]. The ability to create highly aligned graphene-CNT nanohybrids [162, 163] with tunable electrical and mechanical properties [155, 156, 164] enables a wide range of potential applications.

In this chapter, we analyse the optical properties of an all-carbon nanohybrid system comprising a monolayer GNF resonator and a single-walled semiconducting CNT. As shown in figure 5.1, an elliptically shaped monolayer GNF resonator is considered, and its polarizability is approximated to an ellipsoidal NP using Eq. (3.31). This approximation is used in several previous works to calculate the polarizability of GNF resonators [4, 7, 141], and the results were found to be in good agreement with experiments [7, 139]. Furthermore, the CNT is modelled as a two-level quantum system [165, 166], considering only the lowest electronic excitation in its energy bands, and the relevant parameters are obtained using the density matrix theory-based study outlined in [102]. With these approximations, the generalised optical model derived in chapter 3 can be used to study the scattering spectrum of the all-carbon nanohybrid.

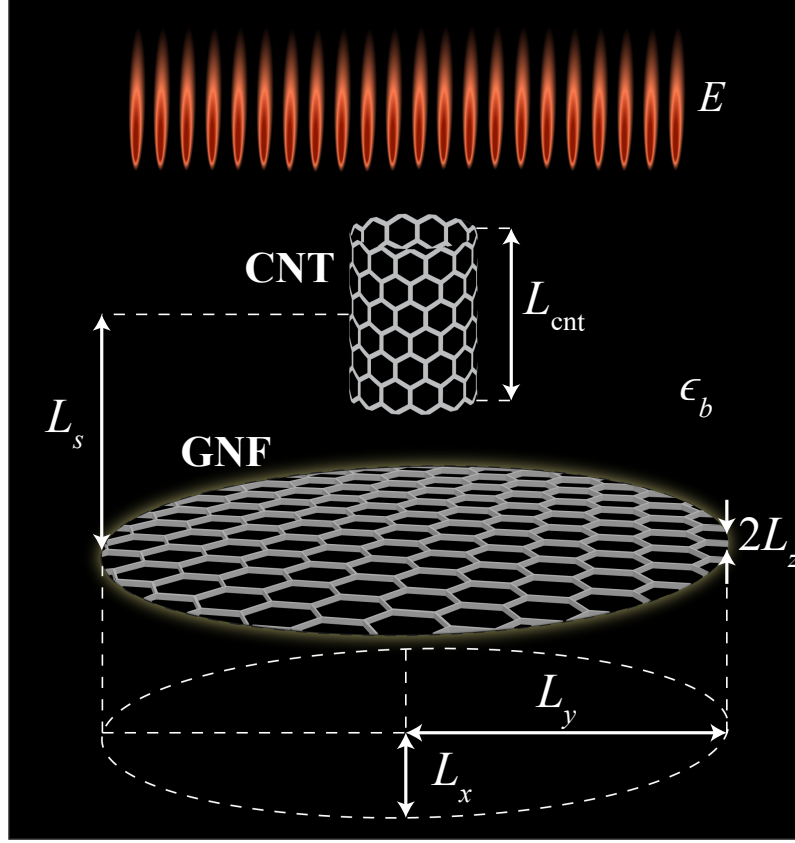


Figure 5.1: The schematic diagram of the GNF-CNT nanohybrid system.

5.1.1 Overview of the GNF-CNT nanohybrid system

As shown in figure 5.1, we consider a nanohybrid system comprising an elliptical GNF resonator with semi-axes L_x and L_y and thickness $2L_z$, coupled to a single-walled semiconducting CNT with length L_{cnt} . It is submerged in a dielectric medium with a real positive relative permittivity ϵ_b . The GNF and CNT are separated by a distance of L_s , which is measured from the midpoint of the CNT to the midpoint of the GNF, as shown in figure 5.1. In this nanohybrid system, the surface separation between the GNF and the CNT is greater than 2 nm where tunnelling effects are negligible [11, 30]. The nanohybrid system is driven by an external coherent laser beam in the z -axis.

5.1.2 Numerical simulation parameters

This section defines the parameter values used in the numerical simulations. In order to neglect the edge effects, the GNF diameter should exceed 10 nm [7]. Furthermore, it needs to be 25 nm-100 nm in size for the conductivity model to be accurate [76]. Therefore, an elliptical GNF with semi-axes, $L_y = 18$ nm and $L_x = 14$ nm is used. The monolayer GNF is considered to have a thickness of 0.35 nm which makes $L_z = 0.175$ nm [7]. The electron relaxation time and the Fermi energy of GNF are taken as $\tau = 10$ ps [76] and $E_F = 0.956$ eV, respectively. The permittivity values of the GNF are calculated using the equations introduced in the section 2.3.4. We are using a semiconducting CNT of type (8,0) which has a squared exciton transition dipole matrix element per unit length of 2.8 au, intrinsic exciton radiative lifetime of 8.1 ps and an excitation energy of 1.55 eV. These CNT parameters are calculated using density functional theory in [102]. The length of the CNT is taken as $L_{\text{cnt}} = 4$ nm. The centres of GNF and CNT are separated by $L_s = 10$ nm and the orientation parameter s_k is set to 2. The permittivity value of the submerging medium is taken as $\varepsilon_b = 5.45$. In the analysis that follows these are used as the default parameters unless mentioned otherwise.

5.2 Results and Discussion

In this section, we show that the exciton-plasmon interactions between the GNF and the CNT give rise to a Fano-like scattering spectrum. We then show that the scattering amplitudes and the shape of this spectrum are tunable using various parameters.

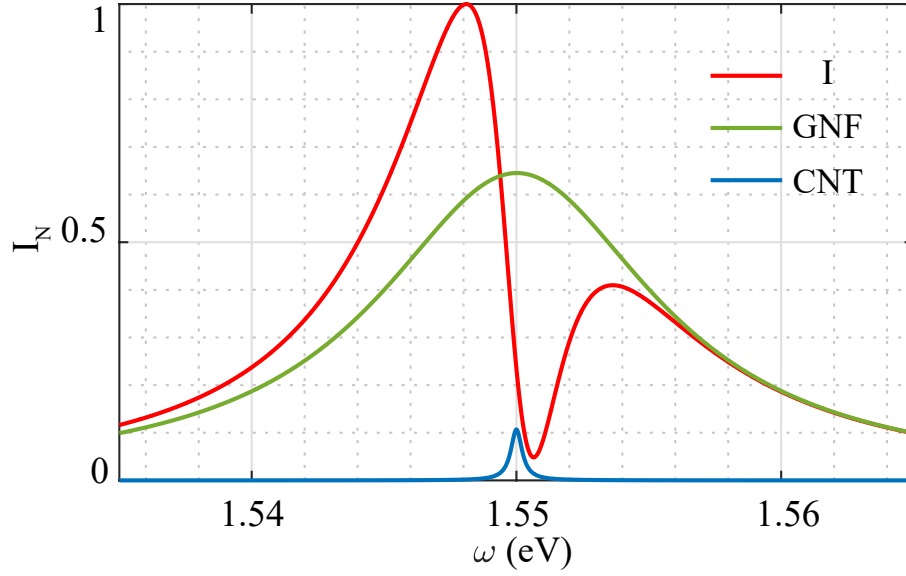


Figure 5.2: The normalized scattering intensity calculated for the parameters specified in section 5.1.2. Red, green and blue solid lines indicate scattering intensities for the GNF-CNT nanohybrid, isolated GNF and isolated semiconducting CNT, respectively.

5.2.1 Enhanced scattering intensities of the nanohybrid

Figure 5.2 compares the isolated scattering intensity spectra of the GNF and the CNT with the scattering spectrum of the GNF-CNT nanohybrid. The spectra of the isolated GNF and CNT are centred around their common resonance frequency 1.55 eV, with the GNF having a larger and broader spectrum compared to the CNT. The nanohybrid has a larger maximum scattering intensity than both isolated GNF and CNT due to interference and self-feedback effects. The intensity spectrum of the nanohybrid shows an asymmetric Fano-like signature with two intensity peaks separated by a clear minimum. For the chosen parameters, there is a significant intensity difference between the two peaks, while isolated GNF peak intensity lies somewhere in between. Constructive interference effects can be observed at frequencies below the CNT excitation frequency, while destructive interference effects reduce the intensity values above it. The minimum point of the nanohybrid scattering spectrum is closer to the CNT excitation en-

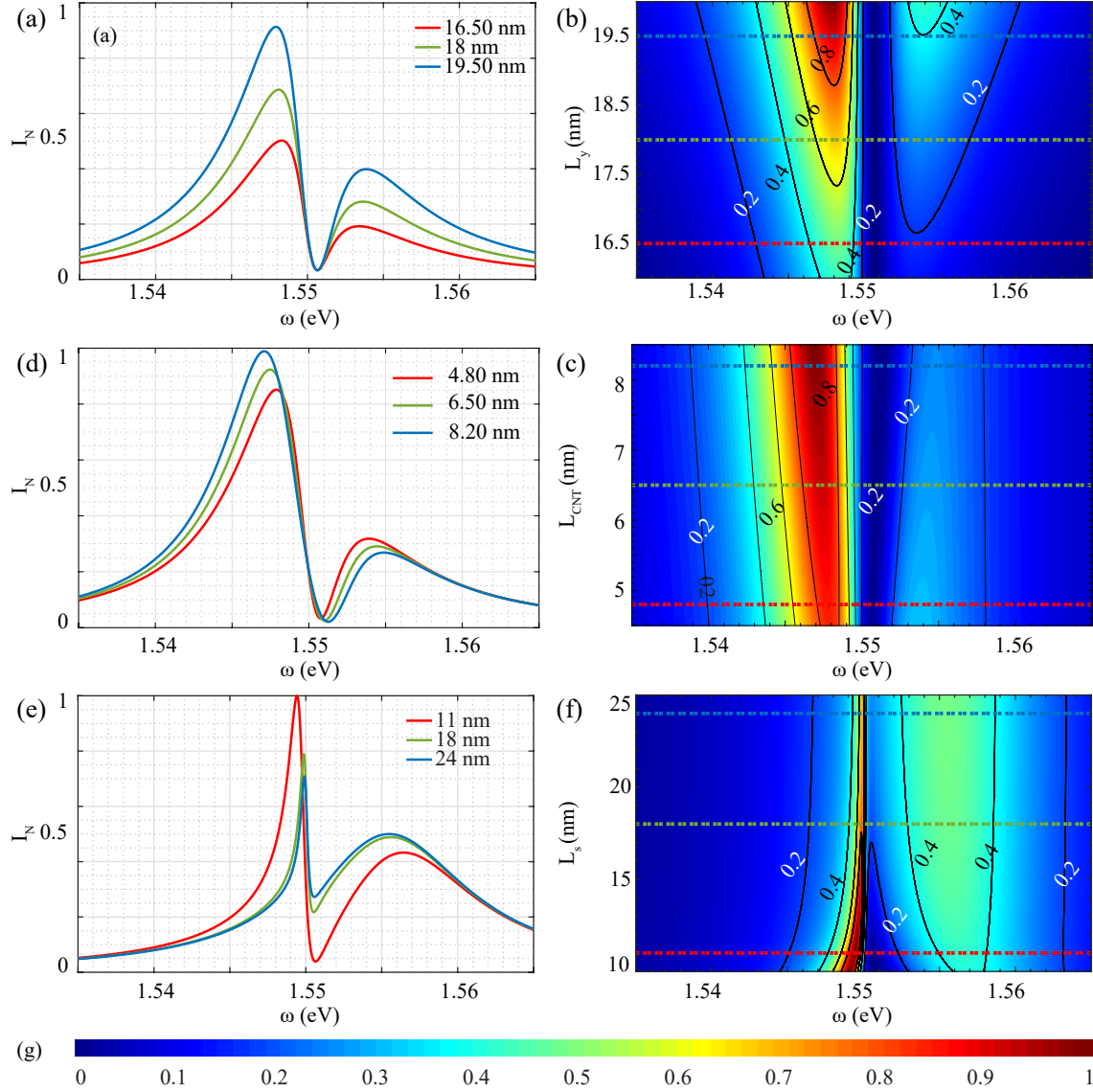


Figure 5.3: (a) and (b) show the normalized scattering intensities calculated by varying L_y from 16 nm to 20 nm. The initial L_x/L_y ratio 7/9 is kept constant during this analysis. (c) and (d) show the normalized scattering intensity calculated by varying the length of the CNT L_{CNT} from 4.5 nm to 8.5 nm. (e) and (f) show the normalized scattering intensity calculated by varying the separation distance L_s between CNT and GNF from 10 nm to 25 nm (Fermi energy maintained at $E_F = 0.96$ eV, which corresponds to a detuning of 5 meV). (g) The colour bar used in the surf plots. (a), (c) and (e) are the line plots of normalized scattering intensities at different values of L_y , L_{CNT} and L_s , respectively. (b), (d) and (f) depict the top view of the colour coded scattering intensity surface plots for the entire L_y , L_{CNT} and L_s range. The dotted lines correspond to the relevant coloured line plots depicted in (a), (c) and (e). All plots are normalized by the maximum intensity peak in the relevant subplot.

ergy. The spectrum of the nanohybrid seems to follow the isolated GNF spectra for frequencies far away from the CNT excitation frequency due to negligible interference originating from the CNT.

5.2.2 Scattering spectrum dependence on GNF size, CNT size and interparticle distance

Next, we will investigate how different system parameters affect the nanohybrid scattering spectrum. As shown in Eq. (3.7), increasing the GNF and CNT dipole moments increases the system coupling constant g . As g increases, so does the amount of system interference due to the increasing exciton-plasmon interactions. The presence of system interference governs the properties of the scattering spectra shown in figure 5.3(a-f). The observed behaviour of the normalised scattering intensity (I_N) with varying GNF size and CNT length is shown in figure 5.3(a-b) and figure 5.3(c-d), respectively. It is noted that increasing the size of the GNF and extending the length of the CNT increases the dipole moment of each individual element. Furthermore, it is observed that as g increases, the frequency separation between the scattering peaks also increases. However, the larger and the smaller peaks of the spectra behave differently in the two scenarios as depicted in figure 5.3(a) and figure 5.3(c). As the GNF size increases (figure 5.3(a)), both the larger and smaller peaks depict amplification characteristics. However, when the CNT length increases (figure 5.3(c)), the larger peak depicts amplification characteristics, whereas the smaller peak depicts diminishing characteristics. As seen in Eq. (3.46), the separation distance between the GNF and the CNT (L_s) has an inverse cubic relationship with the coupling constant. This explains the scattering intensity behaviour shown in figure 5.3(d) where the larger and the smaller peaks approach each other as the separation distance increases. Furthermore, it is observed that as the coupling constant reduces, the larger peak diminishes, and the smaller peak amplifies. Increasing L_s further will result in

negligible interference in the nanohybrid, rendering the scattering spectrum to a summation of the isolated GNF and CNT scattering spectra. It is important to note that changing L_s or L_{cnt} will not alter the resonance frequency of either the GNF or the CNT. Therefore, the observed changes in the scattering spectra are mainly due to the variations of the system coupling constant.

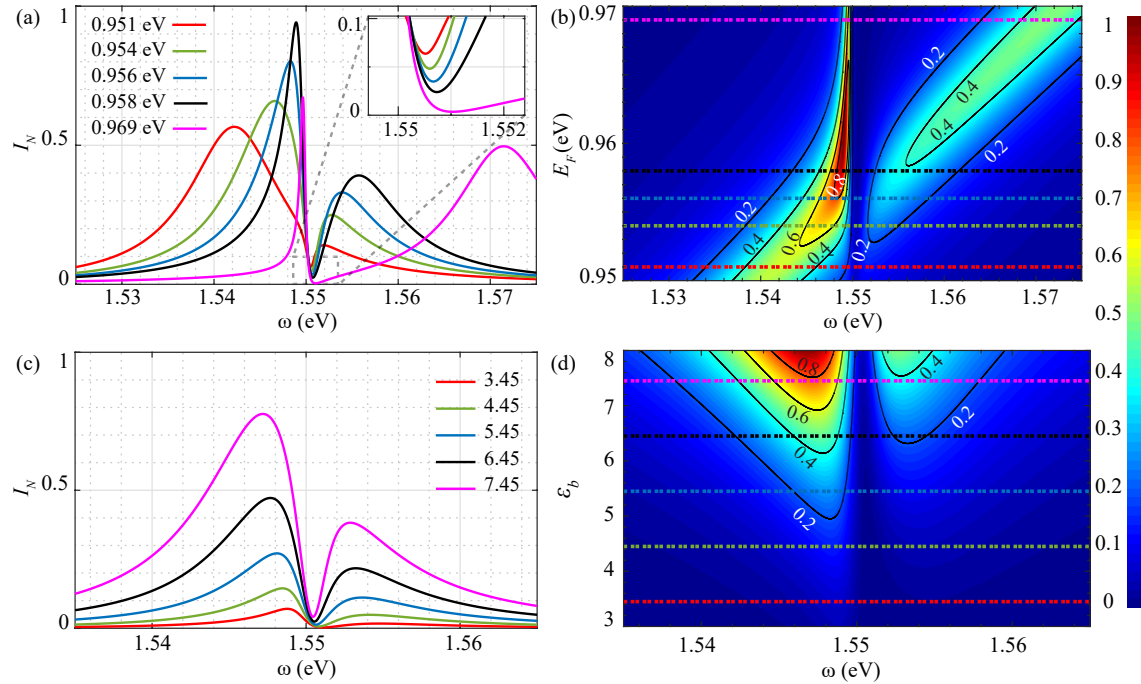


Figure 5.4: (a) and (b) show the normalized scattering intensities calculated by varying Fermi energy of the GNF E_F from 0.95 eV to 0.97 eV. (c) and (d) show the normalized scattering intensities calculated by varying the bath permittivity ϵ_b from 3 to 8. (a) and (c) are the line plots of normalized scattering intensities at different values of E_F and ϵ_b . (b) and (d) depict the top view of the colour coded scattering intensity surface plots for the entire E_F and ϵ_b range. The dotted lines correspond to the relevant coloured line plots depicted in (a) and (c). All plots are normalized by the maximum intensity peak in the relevant subplot.

5.2.3 Tailoring the scattering properties using Fermi energy level

The optical properties of the GNF are easily controllable using the Fermi energy level, which can be changed at the fabrication process using chemical or elec-

trostatic gating [23]. In conventional MNP resonators, the only way to change the LSPR frequency is to change its size or material. Therefore, the conventional MNP-QD nanohybrids inhibit the ability to tune both resonator size and LSPR frequency simultaneously, making them less suitable in applications which impose both size and resonance requirements. For example, in biosensing applications, the size of the nanohybrid may be restricted by cell penetration requirements [167]. When attempting to meet such size requirements, the LSPR might deviate away from the desired region as it is strictly determined by the MNP size. However, in GNF resonators, the desired LSPR frequency can be easily obtained by selecting the relevant Fermi energy level at the fabrication process for any size requirement.

Figure 5.4(a) and 5.4(b) demonstrate the tunability of the scattering spectrum using the Fermi energy level of the GNF while keeping the dimensions of the nanohybrid unchanged. For the GNF dimensions specified in section 5.1.2, it was found that the GNF needs to have $E_F = 0.956$ eV to be resonant with the selected CNT. LSPR frequency and corresponding LSPR amplitude of the GNF resonator increase with the increasing E_F value. When Fermi energy level has a lower value than its value at resonance (i.e. $E_F < 0.956$ eV), GNF has a negative detuning with the CNT. With the increasing E_F value, LSPR frequency blueshifts and detuning decreases. When E_F increases beyond 0.956 eV, GNF acquires a positive detuning with the CNT. As shown in figure 5.4(b), with the decreasing detuning between the GNF and CNT, the frequency separation between the two scattering intensity peaks in the spectrum diminishes. Inset in figure 5.4(a) shows that the minimum point in between the two peaks reduces at higher Fermi level.

5.2.4 The sensitivity of the scattering properties to the medium permittivity

Finally, the way bath permittivity variations can change the scattering spectrum of the nanohybrid is analysed. The value of ϵ_b depends on the medium submerging the nanohybrid. For the case of an *in vivo* therapeutic procedure, the relevant ϵ_b is the tissue permittivity. Figure 5.4(c) and figure 5.4(d) show the normalized scattering intensity spectrum for various ϵ_b values. Increasing ϵ_b alters the intensity spectrum in two ways. First, the scattering intensity values of the whole spectrum increases as the GNF dipole moment is linearly proportional to ϵ_b according to Eq. (3.47). Second, spectrum acquires a small redshift as the GNF resonance frequency depends linearly on $-\epsilon_b$ from Eq. (3.44).

5.3 Summary and Conclusion

In this chapter, we studied the scattering characteristics of an all-carbon exciton-plasmon nanohybrid in which an elliptical monolayer GNF resonator is coupled to a semiconducting CNT gain element. A detailed numerical analysis was performed to demonstrate that the proposed nanohybrid possesses a Fano-like spectrum. This spectrum was shown to be highly tunable using various system parameters such as the Fermi energy of the GNF, component dimensions, GNF-CNT separation distance and the permittivity of the submerging medium. The GNF surface plasmon properties are highly tunable using the Fermi energy and the size of the flake. Furthermore, the emission wavelength of the CNT is easily controllable via its length and chiral indices. Thus, the scattering spectrum of the proposed GNF-CNT nanohybrid possesses much higher tunability than that of the conventional MNP-QD nanohybrid. The Fano-like scattering spectrum is inherently sensitive to the variations in the local environment. Small changes of the refractive index of the submerging medium can induce dramatic variations

in scattering intensities which render the proposed nanohybrid attractive for a range of applications [168] such as optoelectronic devices and nanosensors.

This page intentionally left blank.

Chapter 6

Comparison of the Permittivity Sensing Capabilities of Graphene-based Nanohybrids and Metal Nanoparticle-based Nanohybrids

6.1 Overview

The results of the previous Chapters (3-5) show that the scattering properties of the proposed nanohybrids are highly sensitive to the permittivity changes in the surrounding medium. Nanohybrids inherit this property from their NRs which have LSPRs that are sensitive to even the minute changes in the surrounding medium. Therefore, the permittivity sensing capability of a nanohybrid is mostly dependent on the properties of the associated NR. Investigating how the choice of NR affects the sensing capability of the nanohybrid can help to choose the right NR depending on the application. Among the large number of NR types that are being investigated for building nanohybrids, gold MNP resonators and GNF resonators have widely been studied and found to have desirable properties [11, 169, 170]. The structural and material differences between these resonators make their optical properties significantly different from each other. The sensing capabilities of a MNP resonator-based nanohybrid against a GNF resonator-

based nanohybrid are compared in this Chapter.

6.2 Simulation Parameters

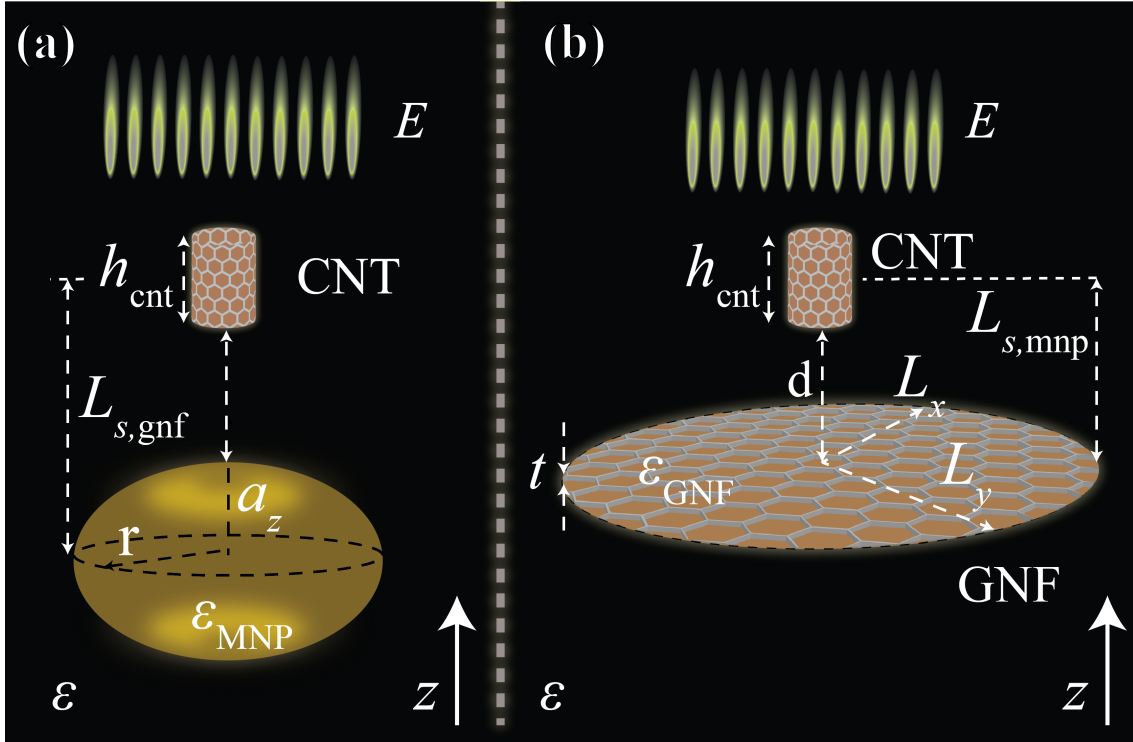


Figure 6.1: Nanohybrid systems used in the comparison. (a) MNP-CNT nanohybrid (b) GNF-CNT nanohybrid. Both systems are using the same CNT and are submerged in a dielectric medium with real positive relative permittivity ϵ and excited by a coherent external laser beam E .

Figure 6.1 shows the nanohybrid systems used for the comparison. As the QE in both nanohybrid designs, a single-wall semiconducting CNT of type (8,0) is used. The CNT length is (h_{cnt}) is 4 nm and the radiative lifetime of its excitons (γ_{cnt}) is 8.1 ps [102]. The nanohybrid systems are excited by a coherent external laser beam with an electric field magnitude of (E) 100 V m^{-1} . A gold spheroidal MNP resonator is used in the nanohybrid system shown in figure 6.1(a). It has semi-axes dimensions $r = 5 \text{ nm}$ and $a_z = 10 \text{ nm}$. The permittivity values for

the gold are obtained from [66]. The GNF resonator-based nanohybrid is an all-carbon nanohybrid which was studied in the previous chapter. An elliptical monolayer GNF with dimensions $L_x = 20$ nm, $L_y = 24$ nm is used as the GNF resonator. The thickness (t), Fermi energy level and the electron relaxation time (τ) of the GNF are taken as 0.956 eV, 0.35 nm [7] and 10 ps, respectively. The dielectric function of the GNF resonator is modelled using Eq. 2.11. For both nanohybrid designs, the surface separation between the corresponding NR and QE (d) is kept at 8 nm. The separation distance for the GNF resonator-based nanohybrid ($L_{s,gnf}$) is calculated as $d + h_{cnt}/2 + t/2$ and the separation distance for the MNP based nanohybrid is calculated as $d + h_{cnt}/2 + a_z$. The analytical model from Chapter 3 is used to compare the scattering properties of the two nanohybrid systems. During the numerical simulations, the medium permittivity value is varied at around $\epsilon = 5$ to investigate how scattering characteristics of each nanohybrid is affected by the medium permittivity change.

6.3 Numerical Results and Discussion

As shown in figure 6.2(a) and figure 6.2(b), the scattering spectra of both nanohybrid systems have a Fano-like line shape. The brown line plots show the scattering spectrum of the isolated CNT, which has its excitation frequency at 1.55 eV. As shown by the solid green lines in figure 6.2, when medium permittivity value is 5, NRs and QEs from both nanohybrids are nearly resonant with each other. This leads to strong exciton-plasmon interactions inside the nanohybrids that make their scattering intensities enhanced compared to their constituents.

The solid and dotted purple lines in figure 6.2 show scattering spectra of nanohybrids and their isolated NRs when medium permittivity value is 4. When the medium permittivity decreases, the LSPR frequency of the MNP resonator acquires significant blueshift from its original position. Therefore, the MNP res-

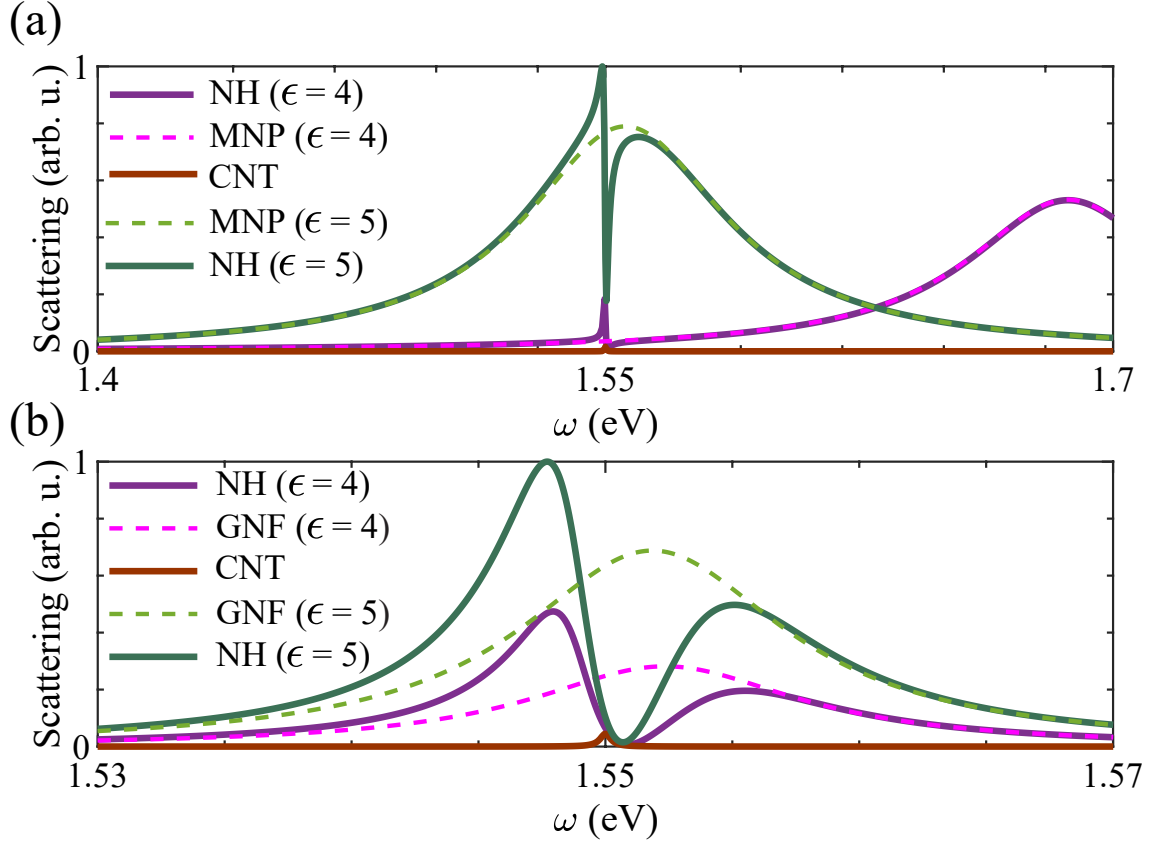


Figure 6.2: Scattering spectra of each nanohybrid compared to that of their isolated components. (a) Scattering spectrum of the MNP-CNT nanohybrid for medium permittivity values 4 (solid green line) and 5 (solid purple line). When $\epsilon = 4$, the scattering intensities from the MNP-CNT nanohybrid has no significant enhancement over the isolated MNP resonator scattering intensity values. (b) Scattering spectrum for the GNF-CNT nanohybrid for medium permittivity values 4 (solid green line) and 5 (solid purple line). For both values, scattering intensity values from the GNF-CNT nanohybrid show improvement over that of the isolated GNF resonator. Dotted lines in (a) and (b) show the scattering spectra for the isolated resonators at the corresponding permittivity values. The solid brown lines in (a) and (b) show the scattering spectra for the isolated CNT.

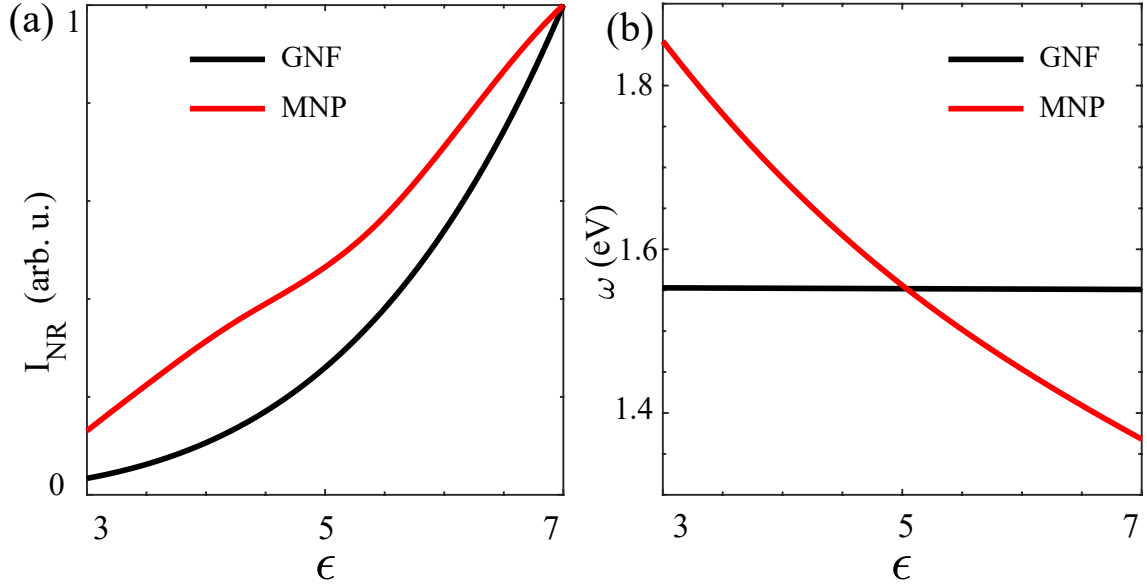


Figure 6.3: The response of the isolated MNP and the isolated GNF resonators to the medium permittivity variations. (a) The maximum scattering amplitude variation for different medium permittivity values. (b) LSPR frequency variation for different medium permittivity values.

onator and the CNT have a large frequency detuning from each other. This causes weaker exciton-plasmon interactions between the MNP resonator and the CNT that decrease the scattering enhancement of the MNP resonator-based nanohybrid. As shown in figure 6.2(a), when compared to scattering intensities of the isolated MNP resonator, scattering intensities of the MNP resonator-based nanohybrid fails to show a significant improvement. In contrast, the change in the permittivity has a minimal impact on the LSPR frequency of the GNF resonator. As shown in figure 6.2(b), even at $\epsilon = 4$, the GNF resonator and the CNT are nearly resonant with each other. Therefore, the scattering intensities of the GNF resonator-based nanohybrid have enhanced scattering intensities compared to its constituents, even for the lower permittivity value.

Figure 6.3(a) shows the variation of the maximum scattering intensity values of each of the isolated NRs with the medium permittivity value. It shows similar behaviour in both NRs where the maximum scattering obtainable from the iso-

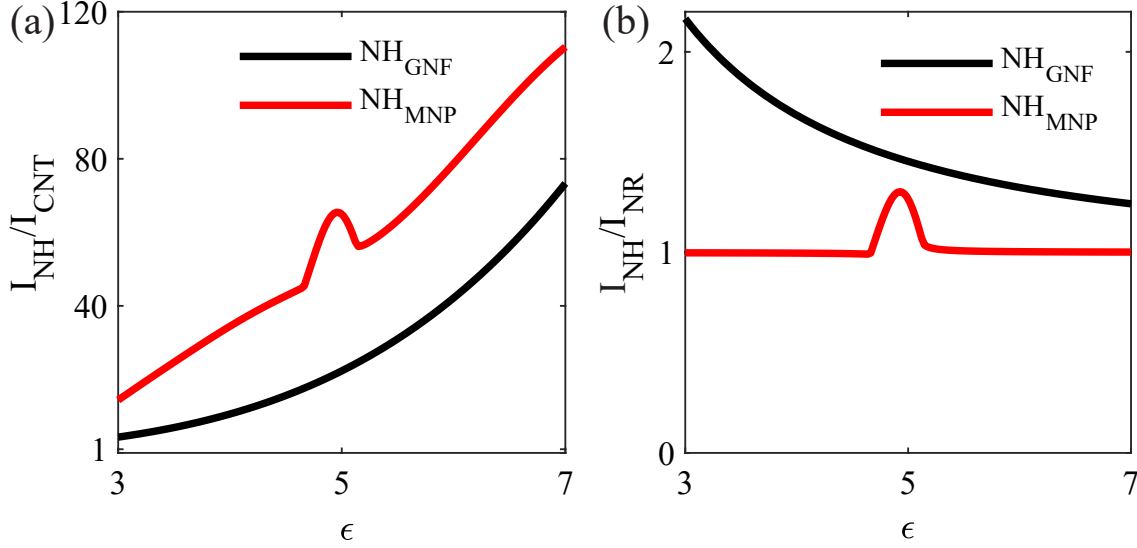


Figure 6.4: Comparison of the maximum scattering intensity values from the nanohybrid systems (I_{NH}) to that of their constituents for different medium permittivity values, ϵ . (a) and (b) Nanohybrid scattering intensity values compared to that of their isolated CNT (I_{CNT}) and isolated NRs (I_{NR}), respectively. The red lines correspond to the MNP resonator-based nanohybrid (NH_{MNP}) and the black lines correspond to the GNF resonator-based nanohybrid (NH_{GNF}).

olated NR increases with the increasing medium permittivity. However, as shown in figure 6.3(b) the LSPR frequency of the NRs respond differently to the medium permittivity changes. It shows that the LSPR frequency of the GNF resonator has a minimal impact from the permittivity variation, whereas the LSPR frequency of the MNP resonator decreases with the increasing medium permittivity. Therefore, for the selected medium permittivity range, as the GNF resonator and CNT emitter are in resonance, the GNF resonator-based nanohybrid can provide higher scattering enhancement compared to the MNP resonator-based nanohybrid.

Figure 6.4 compares the scattering intensity enhancement of nanohybrids to that of their constituents. As shown in figure 6.4(a), when compared to the scattering intensities of isolated QEs, both nanohybrids provide higher scattering intensities. However, figure 6.4(b) shows that the maximum scattering intensities

of the MNP-CNT nanohybrid are mostly similar to that of the isolated MNP. The only exception is when the medium permittivity is closer to 5 at which the CNT and the MNP resonator are in resonance. It also shows that the maximum scattering intensities of the GNF-CNT nanohybrid are always higher than its constituents for the entire permittivity range.

Besides the scattering enhancement, the LSPR properties of the GNF resonator have greater tunability than those in MNP resonators, which provides us with exceptional control over the nanohybrid scattering properties. As shown in Chapter 3 and Chapter 4, to change the LSPR properties of MNP resonators, in both solid homogeneous and nanoshell types, their structure has to be changed in some way (changing size, shape, material, core to shell ratio). However, using electrostatic gating, the LSPR properties of the GNF resonators are easily tunable without altering its physical size [23].

The GNF resonator-based nanohybrid can provide scattering enhancement over a broader permittivity range and have greater tunability than MNP resonator-based nanohybrids. Therefore, for sensing applications that depend on scattering intensities, the GNF resonator-based nanohybrids are more suitable.

This page intentionally left blank.

Chapter 7

Nanohybrids for Biosensing Applications

This chapter discusses the prospect of using nanohybrids for biosensing applications. By using a simple tissue model and nanohybrid designs from previous chapters, we demonstrate how scattering properties of nanohybrids can be used to detect tumours and reconstruct tumour permittivity profiles.

7.1 Nanohybrid-based *in vivo* Tumour Detection Procedure

In this section, we describe the general procedure of nanohybrid-based *in vivo* tumour detection. The main stages of sensing application are shown in figure 5.1. As shown in figure 5.1(a), we have a patient with a tumour, and we aim to use scattering signatures of the nanohybrids to detect the presence of the tumour in the patient. As the first step, we inject a nanohybrid sample into the patient's body. After injecting, the nanohybrids can reach to any part of the body through the vascular system [171, 172].

When compared to healthy parts of the body, tumours have different biological characteristics. For example, tumour cells grow and multiply rapidly compared to healthy cells. To grow quickly, tumours need more blood, and they get it by increasing the growth of blood vessels around the tumour. Because

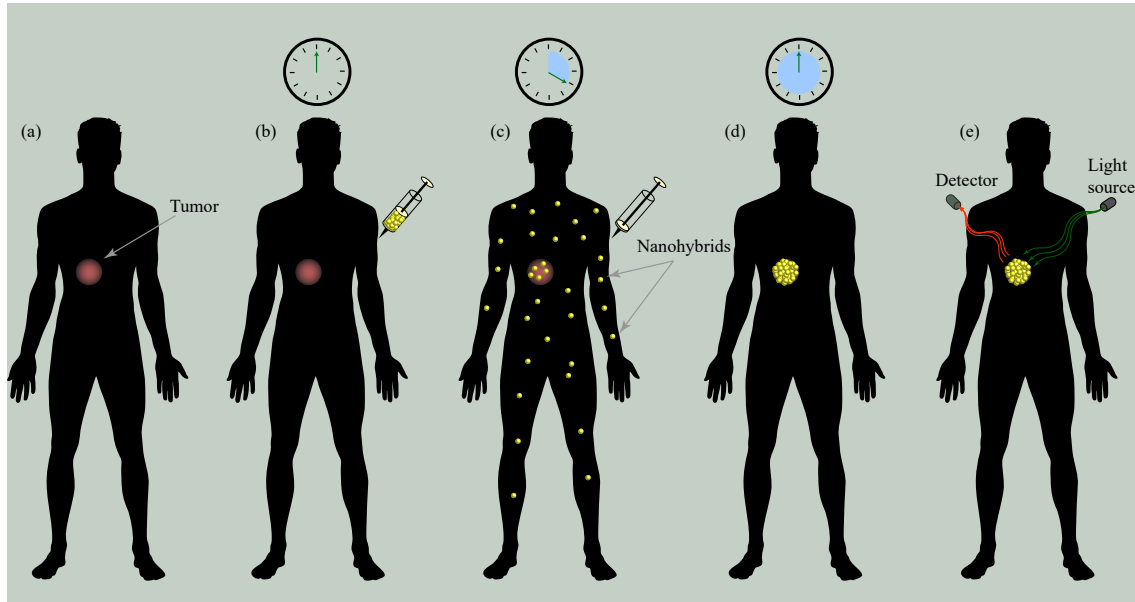


Figure 7.1: Nanohybrid based *in vivo* tumour detection procedure. (a) Patient with the tumour. (b) Injecting nanohybrid sample to the patient. (c) Nanohybrids are starting to accumulate inside the tumour due to the EPR effect. (d) After some time, most of the nanoparticles are accumulated inside the tumour. (e) The nanohybrids are excited by a light source, and the detected scattering intensities are used for tumour detection.

of poorly aligned cells, the muscular layers of blood vessels at the tumour are not smooth and have openings. These openings allow small particles such as nanohybrids to leak into the tumour and accumulate inside it. This is known as the enhanced permeability and retention (EPR) effect, which is widely used in nanomedicine [172,173]. Therefore, due to the EPR effect, the injected nanohybrids will passively accumulate inside the tumour [171,174].

The accumulated nanohybrids can be excited using an external light source, and the scattering signatures of which will have a high correlation to the corresponding tumour characteristics. It is known that the dielectric permittivity inside a tumour is higher than that of the surrounding healthy tissues [175]. Therefore, if the relationship between the scattering intensity and the medium permittivity is known, the presence of tumours in the body can be detected. Fur-

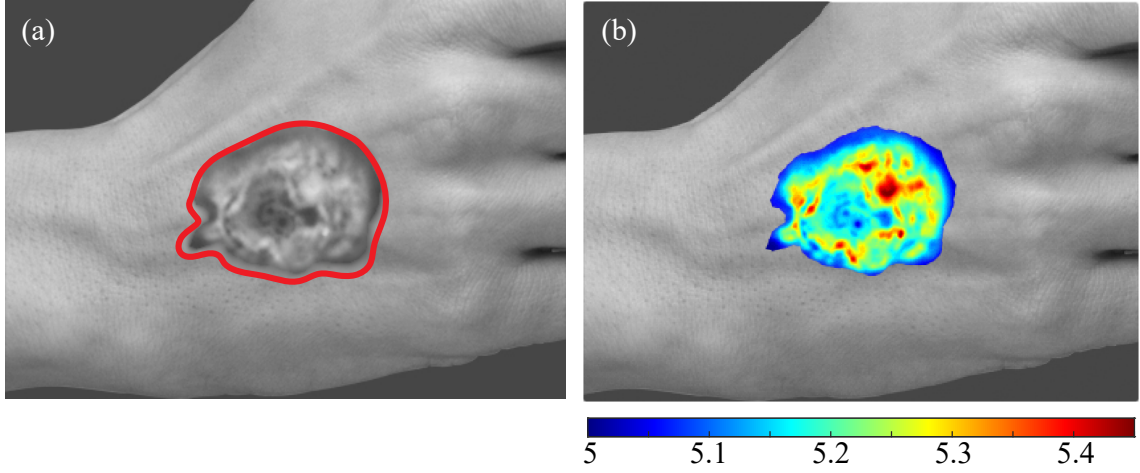


Figure 7.2: (a) Artistically illustrated skin cancer on a hand. The tumour area is marked using the red outline. (b) The grayscale pixel intensity values of the tumour region are linearly mapped to permittivity values (5-5.45) and colour coded.

thermore, the scattering intensity values can be used to reconstruct the permittivity profile of the tumour, which can be used for tumour classification. The nanohybrid-based approaches provide localized imaging of tumours with minimal damage to the healthy tissues around the tumour. The same approach is even suitable for detecting tumours in multiple places in the body.

7.2 Exploiting Nanohybrid Scattering Properties in Biosensing

As discussed in the previous chapters, nanohybrids possess unique and tunable scattering properties compared to their individual components. Nanohybrids with different NRs and QEs have distinctly tunable scattering characteristics. This section discusses how the scattering intensities and frequency separation of the two peaks in the scattering spectra of nanohybrids can be used for tumour detection.

In the numerical simulations, a simple tumour model is used to demonstrate

the prospect of using the nanohybrid scattering properties in tumour detection. We consider a skin tumour that is two-dimensionally distributed in the epidermis and dermis (E-D) layer. Figure 7.2(a) shows the artistically illustrated skin tumour on a hand where the boundary of the skin tumour is marked using the red outline. It is known that tumour tissues have a higher optical permittivity compared to healthy tissues. The optical permittivity of the healthy E-D tissue is found to lie between values 5 and 5.12 [175]. The skin tumour tissues have an optical permittivity value of 5.45, which is higher than that of the healthy tissues [175]. The permittivity values of cells immediately adjacent to the tumour are higher than the normal healthy cells but lower than tumour cells [176]. Therefore, in the simulation, it is assumed that the permittivity values of the skin tumour model range from 5 to 5.45 and the greyscale pixel intensity values of the tumour region have a linear relationship with the underlying tumour permittivity values. Following these assumptions, the colour coded permittivity distribution of the tumour region is drawn, as shown in figure 7.2(b). Although this is an artificial setup, this tumour model demonstrates the prospect of using the nanohybrid as a biosensor. When the nanohybrid sample is intravenously injected into the patient body, most of them localized in the tumour because of the EPR effect described earlier. In the simulations, we assume a uniform distribution of nanohybrids inside the tumour region, and the scattering intensity values are calculated for the localized nanohybrids under a perpendicular excitation from an external electric field. Next, the techniques of reconstructing the permittivity distribution of the tumour using the received scattering spectra are discussed.

7.2.1 Tumour detection from the frequency separation of the two peaks

This section discusses how the frequency separation between the peaks in the scattering spectrum of the nanohybrid can be used to reconstruct the permittiv-

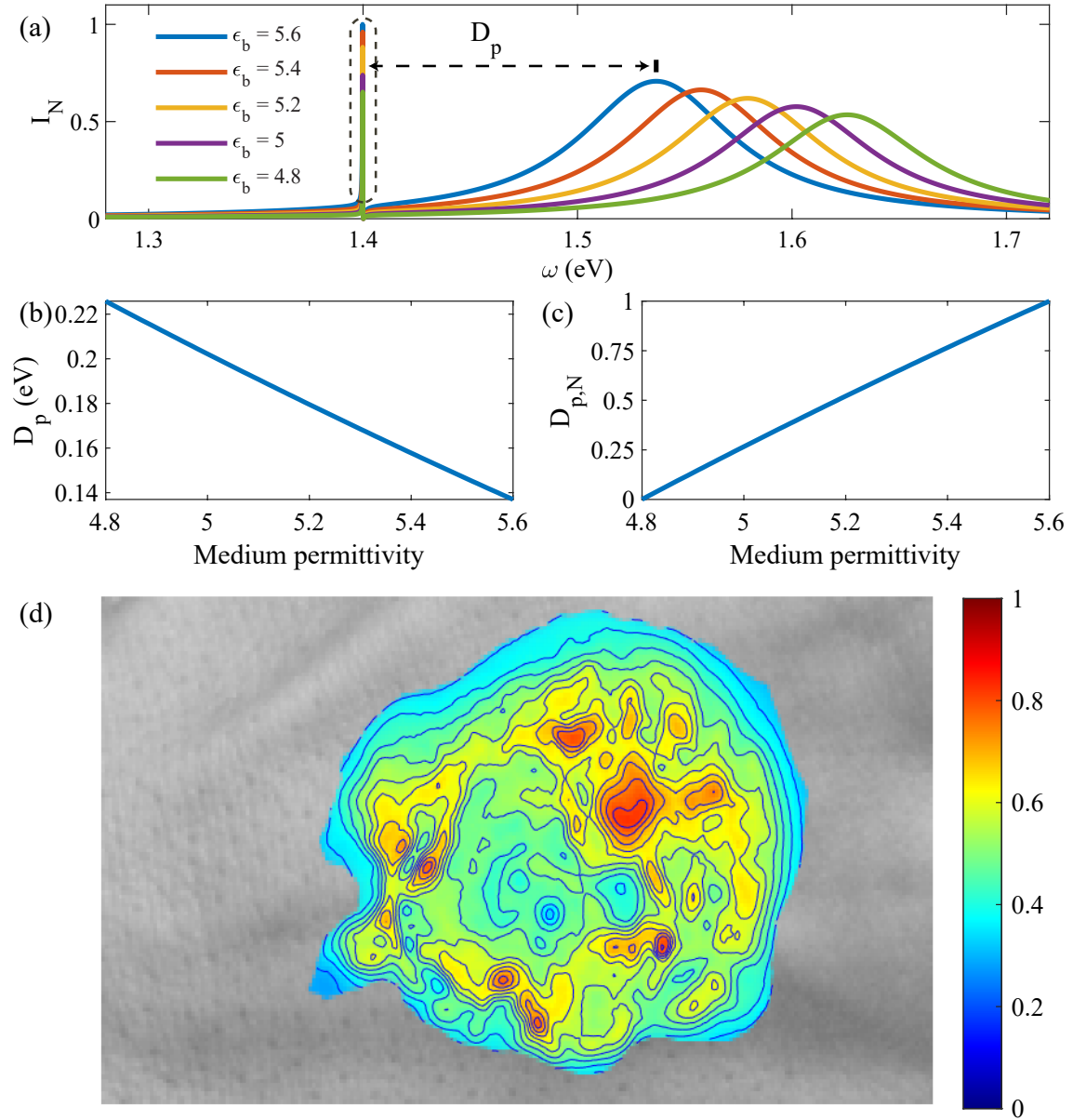


Figure 7.3: Tumour permittivity reconstruction using the frequency separation of the two peaks in the scattering spectrum of a nanohybrid with a nanoshell resonator and a QD. (a) Scattering spectra of the nanohybrid for medium permittivity values 4.8, 5, 5.2, 5.4 and 5.6. D_p is the frequency separation of the two peaks in the scattering spectrum. The dotted line shows the scattering enhancement at the QD excitation frequency. (b) Variation of the peak frequency separation D_p with the medium permittivity value. (c) Normalized peak frequency separation $D_{p,N}$ variation with the medium permittivity. (d) Reconstruction of the tumour permittivity profile shown in figure 7.2(b) using the externally measurable $D_{p,N}$ values.

ity profile of the tumour. The results in figure 7.3 are obtained for the nanoshell resonator-based nanohybrid discussed in Chapter 4. The nanohybrid has the default system parameters defined in the section 4.2 except for the excitation frequency of the QD which was taken as 1.4 eV. As shown in figure 7.3(a), the frequency separation of the peaks in the scattering spectrum is highly sensitive to the medium permittivity changes. For different medium permittivity values, the location of the scattering peak at the QD excitation is stationary (enclosed by the dotted lines), while the location of the other peak varies. The frequency separation between the peaks D_p decreases with the increasing medium permittivity. It is assumed that the nanohybrid can be used to sense medium permittivity values from 4.8 to 5.6, which includes permittivity range of the tumour model.

Figure 7.3(b) shows how frequency separation between the peaks changes with medium permittivity values. We can normalize the D_p value as

$$D_{p,N}(\epsilon_b) = \frac{D_p^+ - D_p(\epsilon_b)}{D_p^+ - D_p^-}, \quad (7.1)$$

where $D_p(\epsilon_b)$, D_p^+ and D_p^- are peak frequency separation values obtainable for medium permittivity value ϵ_b , for the largest medium permittivity measurable from the nanohybrid and for the smallest medium permittivity value measurable from the nanohybrid. The $D_{p,N}(\epsilon_b)$ variation with medium permittivity is shown in figure 7.3(c). This graph can be thought of as a reference graph for this particular nanohybrid. For example, once we measure frequency separation between the peaks, we can use Eq. 7.1 to obtain the $D_{p,N}(\epsilon_b)$ and from it the underlying permittivity value.

Figure 7.3(d) shows the simulated $D_{p,N}$ values for the nanohybrids accumulated in the tumour. The reconstructed profile has a high resemblance to the tumour permittivity profile shown in figure 7.2(b). This shows that the frequency separation between the two peaks in the scattering spectrum can be used for tu-

tumour permittivity profile reconstruction. Several design considerations should be taken when designing nanohybrid for this type of sensing application. First, the excitation frequency of the QD should always be less than the LSPR frequency of the NR at the highest permittivity value. If this condition is violated the reference graph can become multivalued as the LSPR frequency of the NR becomes lower than the QD excitation frequency. Next, it is important to use a NR whose LSPR frequency has a higher sensitivity to the medium permittivity variations. When these conditions are satisfied, the measured $D_{p,N}$ values from nanohybrids can be used for detection and reconstruction of tumour permittivity profiles. Next, we discuss how scattering intensity values of nanohybrids can be used for tumour detection.

7.2.2 Tumour detection from the magnitude of the scattering intensity

This section explains how to use the scattering intensities of nanohybrids to reconstruct the permittivity profile of the tumour. The proposed all-carbon nanohybrid from Chapter 5 is used, and the same system parameters specified in section 5.1.2 are used for the simulation. Similar to the previous section, it is considered that this nanohybrid is used to sense the medium permittivity values from 4.8 to 5.6. This permittivity range covers the permittivity values of the tumour model. Figure 7.4(a) shows the scattering spectra of the nanohybrid for various medium permittivity values. For the all-carbon nanohybrid, a significant variation of D_p cannot be observed; however, the scattering intensities are profoundly affected by the permittivity change. Therefore, in sensing applications, these magnitude variations can be used to find the underlying medium permittivity values.

The dotted line in figure 7.3(b) shows the variation of the maximum scattering intensity of the nanohybrid ($\max(I_N)$) for the entire permittivity range. The

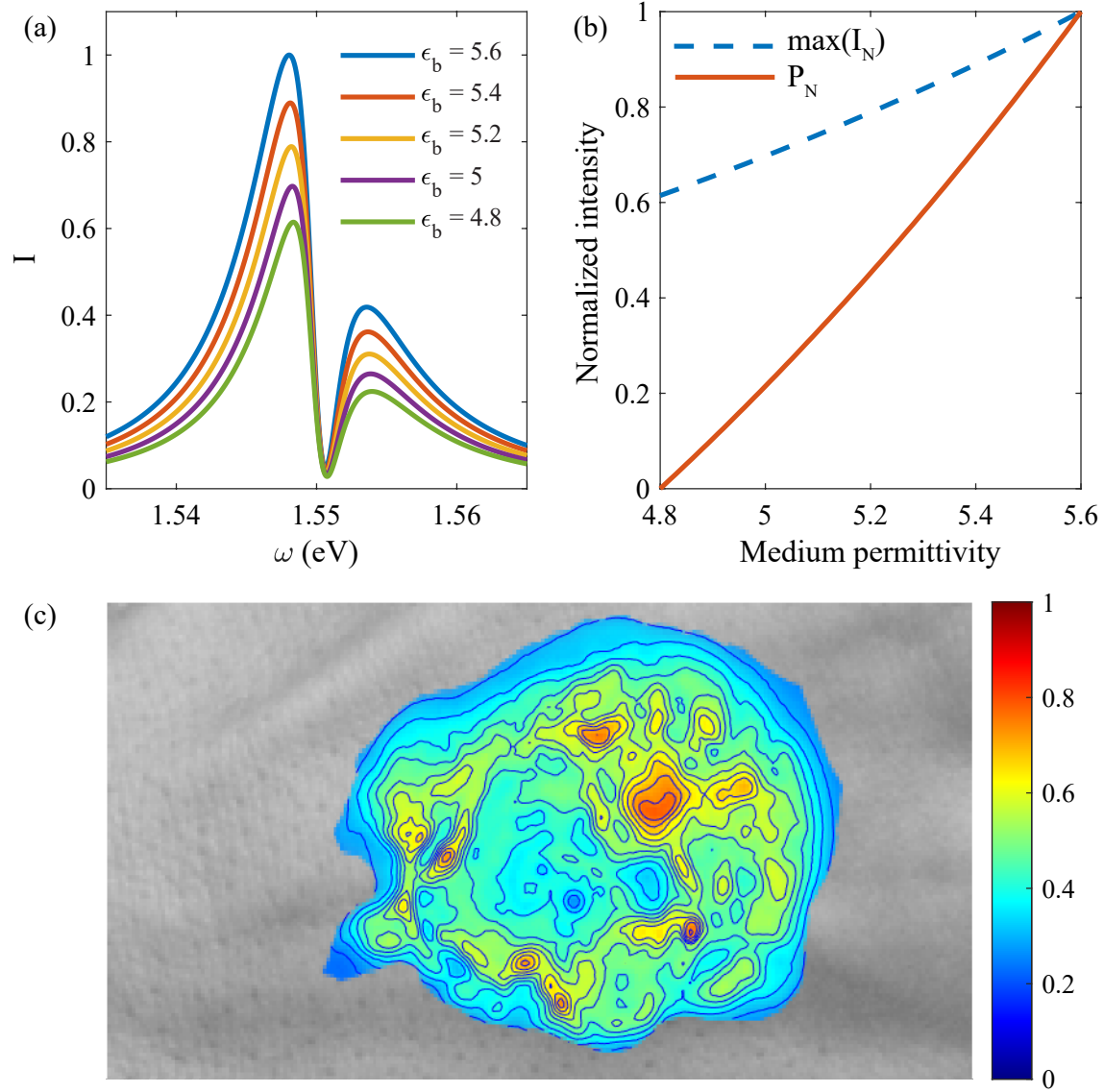


Figure 7.4: Tumour permittivity reconstruction using the scattering intensity from an all-carbon nanohybrid. (a) Normalized scattering spectra of the nanohybrid for medium permittivity values 4.8, 5, 5.2, 5.3, 5.4 and 5.6. (b) Red line shows the normalized peak scattering intensity magnitude (P_N) variation with the medium permittivity value. P_N was calculated using the Eq. (7.2). The dotted line shows $\max(I_N)$ variation with medium permittivity value. (c) Reconstruction of the tumour permittivity profile shown in figure 7.2(b) using the externally measurable scattering intensity values.

normalized peak scattering intensity magnitude (P_N) can be defined as

$$P_N(\varepsilon_b) = \frac{I_{\varepsilon_b}^{\max} - I^+}{I^+ - I^-}, \quad (7.2)$$

where $I_{\varepsilon_b}^{\max}$, I^+ and I^- are maximum scattering intensity values obtainable for medium permittivity value ε_b , for the largest medium permittivity measurable from the nanohybrid and for the smallest medium permittivity value measurable from the nanohybrid. Figure 7.3(b) shows the P_N variation of the nanohybrid and provides the relationship between the nanohybrid scattering intensity value and the medium permittivity.

Assuming a uniform distribution of nanohybrids inside the tumour region, the scattering intensity values were calculated for the accumulated nanohybrids. The externally measurable normalized peak scattering intensity variation for the accumulated nanohybrids is shown in figure 7.3(c). Comparing with figure 7.2(b), it can be seen that the reconstructed profile has a close resemblance to the tumour permittivity profile. This shows that the scattering intensity values of the accumulated nanohybrids can be used to detect tumour regions.

7.3 Summary and Conclusion

In this chapter, the prospect of using scattering properties of nanohybrids in the EPR effect-based tumour detection applications was demonstrated using two different approaches. First, the frequency separations of the peaks in the scattering spectrum of gold nanoshell-QD nanohybrids were used to reconstruct the tumour permittivity profile and identify tumour regions. Next, the various aspects that should be taken into consideration when designing nanohybrids for such applications were discussed. Finally, the techniques for exploiting the scattering intensities of all-carbon nanohybrids in tumour detection were explained. The

scattering-based nanohybrid sensors are highly versatile as their scattering properties are easily tunable using various system parameters. Therefore, nanohybrids show great potential as biosensors in extremely accurate and minute imaging and sensing applications.

Chapter 8

Contributions and Future work

This chapter summarises the contributions of the work presented in the thesis and recommendations for future research work.

8.1 Summary of Contributions

Research objective 1 - Developing an analytical model to describe the scattering properties of a nanohybrid comprising an ellipsoidal nanoresonator coupled to a quantum emitter

In this stage, the scattering properties of a nanohybrid with an ellipsoidal NR and a coupled QE were analytically modelled using a cavity QED based approach. The nanohybrid system was modelled as an open quantum system, and equations were obtained for the dipole moment operator of the NR and the interaction energy between the NR and QE. Then, an equation was derived for the Rayleigh scattering spectrum of the nanohybrid. The developed analytical model is highly versatile and can be used to analyse scattering properties of nanohybrid designs with different NRs such as ellipsoidal, spheroidal, spherical and disk-shaped NRs. It was shown that by changing the aspect ratio of the ellipsoidal NR, the scattering properties of the nanohybrid could be changed; a feature that is not present when spherical NRs are used. Numerical simulations were performed to investigate how different system parameters affect the scattering spectra of a

nanohybrid with a gold spheroidal NR and a coupled QD. The results showed that the scattering properties of the nanohybrid could be controlled by changing the polarisation direction and interparticle distance, and they are extremely sensitive to the permittivity changes of the local environment.

Research objective 2 - Studying the scattering properties of a nanohybrid with a spheroidal metal nanoshell resonator

In this stage, we improved the tunability of the scattering properties of the nanohybrid design from the previous stage, where we used a homogeneous solid metal NR. The LSPR of the homogeneous solid metal NR can only be changed by altering its size or material. Therefore, if an application imposes both size limitations and resonance requirements, using a solid metal NR-based nanohybrid might not be feasible. In this stage, it was found that it is possible to overcome this limitation by using metal nanoshell resonators in the nanohybrid designs. An effective permittivity model based on internal homogenization was used to model the polarizability of a spheroidal metal nanoshell resonator. Then the scattering properties of a nanohybrid system comprising a gold nanoshell resonator and a QD were numerically analysed. The results show that the nanoshell resonator-based nanohybrids possess highly versatile scattering properties that can be easily tuned by changing the core to shell ratio of the NR and without changing the overall system size. It was also shown that higher scattering intensities could be obtained by using hollow metal nanoshell resonators than using NRs with filled dielectric cores. Furthermore, it was also shown that it is possible to design a nanohybrid which operate in the near-infrared frequency regime, which is useful for biosensing applications, using metal nanoshell resonators.

Research objective 3 - Investigating the scattering characteristics of an all-carbon nanohybrid

In this stage, a novel all-carbon nanohybrid design was proposed where a monolayer GNF resonator is coupled to a single-walled semiconducting CNT. Due to their remarkable optical and mechanical properties and high biocompatibility, CNTs and GNFs are extensively considered for biological applications. Therefore, by combining them, we can create a nanohybrid that is highly suitable for biosensing. Thorough numerical simulations were performed to find out how different system parameters affect the scattering properties of the proposed nanohybrid. Results showed that system parameters such as CNT and GNF dimensions, the distance between the GNF and CNT affect the scattering properties of the nanohybrid. It was shown that the scattering properties of the nanohybrid could be easily controlled using the Fermi energy level of the GNF resonator without changing any of its physical dimensions. Therefore, all-carbon nanohybrid systems have a higher tunability than conventional metal NR based nanohybrids. It was also shown that the scattering intensity of the all-carbon nanohybrid is highly sensitive to the refractive index changes in its environment.

Research objective 4 - Comparing the permittivity sensing capability of GNF resonator-based nanohybrid and a MNP resonator-based nanohybrid

In previous stages, it was observed that the scattering properties of nanohybrids are sensitive to the permittivity variations of the surrounding medium. Nanohybrids inherit this sensing capability from their NRs, whose LSPR properties are sensitive to the permittivity changes in the surrounding medium. Therefore, the medium sensing capability of the nanohybrids are highly dependent on the properties and the type of NR used inside. In this stage, the medium sensing capabilities of a GNF resonator-based nanohybrid and a MNP resonator-based nanohybrid were compared. The results from the numerical simulations showed that

the scattering intensities of the GNF resonator-based nanohybrid are always better than its constituents for the selected medium permittivity range. However, the scattering enhancement from the MNP resonator-based nanohybrid diminishes when the medium permittivity value changes from its resonant value. Because of this reason, if sensing applications depend on the scattering intensities of the nanohybrid, the GNF resonator-based nanohybrids can be used to detect a broader permittivity range than MNP resonator-based nanohybrids.

Research objective 5 - Investigating the prospect of using nanohybrids as biosensors

As the final stage, we have shown the prospect of using the proposed nanohybrid designs in biosensing applications to detect and reconstruct the permittivity profiles of tumours. Using a simple tumour permittivity model, we demonstrated two methods through which we can exploit scattering properties of nanohybrids to obtain the permittivity profile of the tumour. First, the frequency separation between the peaks in the scattering spectra of gold nanoshell resonator-based nanohybrids were used for tumour detection. Then, it was shown how to use the enhanced scattering intensities of all-carbon nanohybrids in tumour permittivity reconstruction. It was found that both methods can successfully reconstruct the tumour permittivity profile. The results illustrate the prospect of using nanohybrids for minimally invasive biosensing applications.

8.2 Suggestions for Future Work

The work presented in this thesis can be further extended in both theoretical and experimental areas. We outline a few suggestions for future work below.

Modelling and analysing the absorption properties of proposed nanohybrid designs

In this work, we have focused on analysing the scattering properties of several nanohybrid designs and their applications in sensing. Due to exciton-plasmon interactions, the absorptions properties of nanohybrids can also possess exciting features that can be useful in application areas such as cancer hyperthermia, where the heat produced by nanohybrids is used to destroy cancer cells. Therefore, modelling and analysing the optical absorption properties of proposed nanohybrid designs can extend their applications to new directions.

Modelling scattering properties of nanohybrid designs with multiple nanoresonators and quantum emitters

In this work, we have focused on nanohybrid systems with a single NR and a QE. However, when there are multiple NRs and QEs, the interactions and cooperative effects among the constituents can give rise to new scattering features. Therefore, we believe that modelling nanohybrid systems with multiple NRs and QEs will improve our understanding of the nanohybrids and will improve the applicability of nanohybrids in practical scenarios.

Modelling the optical response of the nanohybrids comprising quantum emitters with three or more energy levels

In this thesis, when developing the main analytical equations, the QE was modelled as a two-level system. However, QE with three or more levels can show interesting optical phenomena such as electronically induced transparency. Therefore, analytical modelling of nanohybrids with three or higher level QEs will improve our understanding of nanohybrids.

A comprehensive modelling of nanoshell resonator-based nanohybrids

In chapter 4, an effective medium theory-based approach was used to model the polarizability of the nanoshell resonator. It is possible to improve the analytical model even further by quantum mechanically modelling the optical response of the nanoshell resonator and its interaction with the QD. Such models will allow us to study quantum effects in such systems and will improve our understanding of nanohybrids with nanoshell resonators.

Incorporating nonlocal effects when modelling nanohybrids with ellipsoidal NRs

When nanoparticle size becomes very small, nonlocal effects become important. Nonlocal effects cause a frequency blueshift in the scattering spectrum [27, 45]. Although there are analytical models available to model the nonlocal response of spherical nanoparticles, most of the studies that focus on the nonlocal responses of non-spherical nanoparticles have used numerical simulations. It is possible to improve the analytical model by considering nonlocal effects when modelling the scattering properties of a nanohybrid system with an ellipsoidal NR and a coupled QE.

Comprehensive modelling of the scattering properties of all-carbon nanohybrids

In chapter 5, the scattering properties of GNF were modelled by approximating its polarizability to that of a disk. This assumption is widely used in previous studies and has good validity with experimental results. However, it is possible to model the optical response more accurately using quantum mechanics and incorporating additional structural effects such as skin effects. It is also possible to extend the analytical model to analyse nanohybrids with multilayered graphene

sheets. We can also improve the analytical model by modelling the CNT as a three or multilevel QE.

Developing advanced tissue model and investigating the biosensing capability of nanohybrids by modelling the scattering properties of clusters of nanohybrids

When demonstrating the prospect of using nanohybrids for biosensing applications, a simple tissue permittivity model was used. However, it is important to use an advanced tissue model with high complexity and accuracy to validate their use for sensing applications even further. As explained in Chapter 7, in nanohybrid based biosensing applications, a large number of nanohybrids accumulate inside the tumour. Therefore, interactions among them can be considered to improve the accuracy of the model.

Experimental realisation and validation of proposed nanohybrid designs and their practical applications

Following our theoretical analysis and numerical results, it is essential to experimentally validate these nanohybrid designs and investigate the possibility of using them in sensing applications.

This page intentionally left blank.

Bibliography

- [1] Premaratne, M. & Stockman, M. I. Theory and technology of spasers. *Advances in Optics and Photonics* **9**, 79–128 (2017).
- [2] Artuso, R. D. & Bryant, G. W. Strongly coupled quantum dot-metal nanoparticle systems: exciton-induced transparency, discontinuous response, and suppression as driven quantum oscillator effects. *Phys. Rev. B* **82**, 195419 (2010).
- [3] Stockman, M. I. Nanoplasmonics: past, present, and glimpse into future. *Opt. Express* **19**, 22029–22106 (2011).
- [4] Senevirathne, V. *et al.* Scattering characteristics of an exciton-plasmon nanohybrid made by coupling a monolayer graphene nanoflake to a carbon nanotube. *Journal of Physics: Condensed Matter* **31**, 085302 (2019).
- [5] Senevirathne, V. & Premaratne, M. Comparison of the permittivity sensing capabilities of graphene-based nanohybrids and metal nanoparticle-based nanohybrids. In *2019 IEEE 19th International Conference on Nanotechnology (IEEE-NANO)*, 302–305 (IEEE, 2019).
- [6] McEnery, K., Tame, M., Maier, S. & Kim, M. Tunable negative permeability in a quantum plasmonic metamaterial. *Physical Review A* **89**, 013822 (2014).
- [7] Cox, J. D., Singh, M. R., Gumbs, G., Anton, M. A. & Carreno, F. Dipole-dipole interaction between a quantum dot and a graphene nanodisk. *Phys. Rev. B* **86**, 125452 (2012).

- [8] Hapuarachchi, H. & Premaratne, M. Thermoresponsive nanohybrids for tumor imaging. In *2018 IEEE 12th International Conference on Nano/Molecular Medicine and Engineering (NANOMED)*, 20–24 (IEEE, 2018).
- [9] Artuso, R. D. *The Optical Response of Strongly Coupled Quantum Dot-Metal Nanoparticle Hybrid Systems*. Ph.D. thesis, Faculty of the Graduate School of the University of Maryland, College Park (2012).
- [10] Stockman, M. I. The spaser as a nanoscale quantum generator and ultrafast amplifier. *J. Opt.* **12**, 024004 (2010).
- [11] Ridolfo, A., Di Stefano, O., Fina, N., Saija, R. & Savasta, S. Quantum plasmonics with quantum dot-metal nanoparticle molecules: influence of the fano effect on photon statistics. *Physical review letters* **105**, 263601 (2010).
- [12] Hapuarachchi, H., Mallawaarachchi, S., Hattori, H. T., Zhu, W. & Premaratne, M. Optoelectronic figure of merit of a metal nanoparticle—quantum dot (mnp-qd) hybrid molecule for assessing its suitability for sensing applications. *Journal of Physics: Condensed Matter* **30**, 054006 (2018).
- [13] Zalevsky, Z. & Abdulhalim, I. *Integrated nanophotonic devices* (Elsevier, 2014).
- [14] Loos, M. Chapter 1 - nanoscience and nanotechnology. In Loos, M. (ed.) *Carbon Nanotube Reinforced Composites*, 1 – 36 (William Andrew Publishing, Oxford, 2015). URL <http://www.sciencedirect.com/science/article/pii/B9781455731954000011>.
- [15] Wood, R. W. On a remarkable case of uneven distribution of light in a diffraction grating spectrum. *Proceedings of the Physical Society of London* **18**, 269 (1902).

- [16] Fano, U. The theory of anomalous diffraction gratings and of quasi-stationary waves on metallic surfaces (sommerfeld's waves). *JOSA* **31**, 213–222 (1941).
- [17] Stern, E. & Ferrell, R. Surface plasma oscillations of a degenerate electron gas. *Physical Review* **120**, 130 (1960).
- [18] Huang, K. C. *et al.* Electrically driven subwavelength optical nanocircuits. *Nat. Photon.* **8**, 244–249 (2014).
- [19] Atwater, H. A. & Polman, A. Plasmonics for improved photovoltaic devices. *Nature materials* **9**, 205 (2010).
- [20] Li, Y. *et al.* On-chip zero-index metamaterials. *Nature Photonics* **9**, 738 (2015).
- [21] Poddubny, A., Iorsh, I., Belov, P. & Kivshar, Y. Hyperbolic metamaterials. *Nature Photonics* **7**, 948 (2013).
- [22] Anker, J. N. *et al.* Biosensing with plasmonic nanosensors. *Nat. Mater.* **7**, 442–453 (2008).
- [23] Luo, X., Qiu, T., Lu, W. & Ni, Z. Plasmons in graphene: recent progress and applications. *Materials Science and Engineering: R: Reports* **74**, 351–376 (2013).
- [24] Barnes, W. L., Dereux, A. & Ebbesen, T. W. Surface plasmon subwavelength optics. *nature* **424**, 824–830 (2003).
- [25] Zhang, J. & Zhang, L. Nanostructures for surface plasmons. *Advances in Optics and Photonics* **4**, 157–321 (2012).
- [26] Maier, S. A. *Plasmonics: fundamentals and applications* (Springer Science & Business Media, 2007).

- [27] Amendola, V., Pilot, R., Frascioni, M., Maragò, O. M. & Iatì, M. A. Surface plasmon resonance in gold nanoparticles: a review. *Journal of Physics: Condensed Matter* **29**, 203002 (2017).
- [28] Kumarapperuma, L., Premaratne, M., Jha, P. K., Stockman, M. I. & Agrawal, G. P. Complete characterization of the spasing (II) curve of a three-level quantum coherence enhanced spaser for design optimization. *Applied Physics Letters* **112**, 201108 (2018).
- [29] Mejía-Salazar, J. & Oliveira Jr, O. N. Plasmonic biosensing: focus review. *Chemical reviews* **118**, 10617–10625 (2018).
- [30] Hapuarachchi, H. *et al.* Cavity qed analysis of an exciton-plasmon hybrid molecule via the generalized nonlocal optical response method. *Physical Review B* **95**, 245419 (2017).
- [31] Yu, H., Peng, Y., Yang, Y. & Li, Z.-Y. Plasmon-enhanced light–matter interactions and applications. *npj Computational Materials* **5**, 1–14 (2019).
- [32] Haes, A. J. *et al.* Plasmonic materials for surface-enhanced sensing and spectroscopy. *MRS bulletin* **30**, 368–375 (2005).
- [33] Nehl, C. L. & Hafner, J. H. Shape-dependent plasmon resonances of gold nanoparticles. *Journal of Materials Chemistry* **18**, 2415–2419 (2008).
- [34] Orendorff, C. J., Gearheart, L., Jana, N. R. & Murphy, C. J. Aspect ratio dependence on surface enhanced raman scattering using silver and gold nanorod substrates. *Physical Chemistry Chemical Physics* **8**, 165–170 (2006).
- [35] Garcia-Leis, A., Garcia-Ramos, J. V. & Sanchez-Cortes, S. Silver nanostars with high sers performance. *The Journal of Physical Chemistry C* **117**, 7791–7795 (2013).

- [36] Wirtz, M. & Martin, C. R. Template-fabricated gold nanowires and nanotubes. *Advanced Materials* **15**, 455–458 (2003).
- [37] Long, N. N. *et al.* Synthesis and optical properties of colloidal gold nanoparticles. In *Journal of Physics: Conference Series*, vol. 187, 012026 (IOP Publishing, 2009).
- [38] Xia, Y. & Halas, N. J. Shape-controlled synthesis and surface plasmonic properties of metallic nanostructures. *MRS bulletin* **30**, 338–348 (2005).
- [39] Link, S. & El-Sayed, M. A. Shape and size dependence of radiative, non-radiative and photothermal properties of gold nanocrystals. *International reviews in physical chemistry* **19**, 409–453 (2000).
- [40] Kreibig, U. & Vollmer, M. *Optical properties of metal clusters*, vol. 25 (Springer Science & Business Media, 2013).
- [41] Davis, T. J., Vernon, K. C. & Gómez, D. E. Effect of retardation on localized surface plasmon resonances in a metallic nanorod. *Optics express* **17**, 23655–23663 (2009).
- [42] Myroshnychenko, V. *et al.* Modelling the optical response of gold nanoparticles. *Chemical Society Reviews* **37**, 1792–1805 (2008).
- [43] Chen, H., Kou, X., Yang, Z., Ni, W. & Wang, J. Shape- and size-dependent refractive index sensitivity of gold nanoparticles. *Langmuir* **24**, 5233–5237 (2008).
- [44] Averitt, R. D., Westcott, S. L. & Halas, N. J. Linear optical properties of gold nanoshells. *JOSA B* **16**, 1824–1832 (1999).
- [45] Raza, S. *et al.* Blueshift of the surface plasmon resonance in silver nanoparticles studied with eels. *Nanophotonics* **2**, 131–138 (2013).

- [46] West, P. R. *et al.* Searching for better plasmonic materials. *Laser & Photonics Reviews* **4**, 795–808 (2010).
- [47] Lee, K.-S. & El-Sayed, M. A. Gold and silver nanoparticles in sensing and imaging: sensitivity of plasmon response to size, shape, and metal composition. *The Journal of Physical Chemistry B* **110**, 19220–19225 (2006).
- [48] Amendola, V., Saija, R., Maragò, O. M. & Iatì, M. A. Superior plasmon absorption in iron-doped gold nanoparticles. *Nanoscale* **7**, 8782–8792 (2015).
- [49] Miller, M. M. & Lazarides, A. A. Sensitivity of metal nanoparticle surface plasmon resonance to the dielectric environment. *The Journal of Physical Chemistry B* **109**, 21556–21565 (2005).
- [50] Stewart, M. E. *et al.* Nanostructured plasmonic sensors. *Chemical reviews* **108**, 494–521 (2008).
- [51] Willets, K. A. *et al.* Nanoscale localized surface plasmon resonance biosensors. *Nanobiotechnology II: More Concepts and Applications* 159–173 (2007).
- [52] Liu, Y. *et al.* A plasmonic gold nanostar theranostic probe for in vivo tumor imaging and photothermal therapy. *Theranostics* **5**, 946 (2015).
- [53] Oh, S. J. *et al.* Molecular imaging with terahertz waves. *Optics express* **19**, 4009–4016 (2011).
- [54] Hüger, E. & Osuch, K. Making a noble metal of pd. *EPL (Europhysics Letters)* **71**, 276 (2005).
- [55] Khan, I., Saeed, K. & Khan, I. Nanoparticles: Properties, applications and toxicities. *Arabian Journal of Chemistry* **12**, 908–931 (2019).
- [56] Chen, Y., Xin, X., Zhang, N. & Xu, Y.-J. Aluminum-based plasmonic photocatalysis. *Particle & Particle Systems Characterization* **34**, 1600357 (2017).

- [57] El-Sayed, I. H., Huang, X. & El-Sayed, M. A. Surface plasmon resonance scattering and absorption of anti-egfr antibody conjugated gold nanoparticles in cancer diagnostics: applications in oral cancer. *Nano letters* **5**, 829–834 (2005).
- [58] Hirsch, L. R. *et al.* Nanoshell-mediated near-infrared thermal therapy of tumors under magnetic resonance guidance. *Proceedings of the National Academy of Sciences* **100**, 13549–13554 (2003).
- [59] Lin, T.-E., Chen, W.-H., Shiang, Y.-C., Huang, C.-C. & Chang, H.-T. Colorimetric detection of platelet-derived growth factors through competitive interactions between proteins and functional gold nanoparticles. *Biosensors and Bioelectronics* **29**, 204–209 (2011).
- [60] Chen, L., Li, J. & Chen, L. Colorimetric detection of mercury species based on functionalized gold nanoparticles. *ACS applied materials & interfaces* **6**, 15897–15904 (2014).
- [61] Niu, H. *et al.* Sensitive colorimetric visualization of perfluorinated compounds using poly (ethylene glycol) and perfluorinated thiols modified gold nanoparticles. *Analytical chemistry* **86**, 4170–4177 (2014).
- [62] Loo, C., Lowery, A., Halas, N., West, J. & Drezek, R. Immunotargeted nanoshells for integrated cancer imaging and therapy. *Nano letters* **5**, 709–711 (2005).
- [63] El-Sayed, I. H., Huang, X. & El-Sayed, M. A. Selective laser photo-thermal therapy of epithelial carcinoma using anti-egfr antibody conjugated gold nanoparticles. *Cancer letters* **239**, 129–135 (2006).
- [64] de Ceglia, D. & Vincenti, M. 8 - plasmonics. In Haus, J. W. (ed.) *Fundamentals and Applications of Nanophotonics*, 233 – 252 (Woodhead Publishing,

- 2016). URL <http://www.sciencedirect.com/science/article/pii/B9781782424642000087>.
- [65] Ru, E. C. L. & Etchegoin, P. G. Chapter 3 - introduction to plasmons and plasmonics. In Ru, E. C. L. & Etchegoin, P. G. (eds.) *Principles of Surface-Enhanced Raman Spectroscopy*, 121 – 183 (Elsevier, Amsterdam, 2009). URL <http://www.sciencedirect.com/science/article/pii/B978044452779000009X>.
- [66] Johnson, P. B. & Christy, R.-W. Optical constants of the noble metals. *Phys. Rev. B* **6**, 4370 (1972).
- [67] Haus, J. W. *Fundamentals and applications of nanophotonics* (Woodhead Publishing, 2016).
- [68] Kreibig, U. & Vollmer, M. Theoretical considerations. In *Optical Properties of Metal Clusters*, 13–201 (Springer, 1995).
- [69] Novoselov, K. S. *et al.* Two-dimensional atomic crystals. *Proceedings of the National Academy of Sciences* **102**, 10451–10453 (2005).
- [70] Novoselov, K. S. & Geim, A. The rise of graphene. *Nat. Mater* **6**, 183–191 (2007).
- [71] Grigorenko, A., Polini, M. & Novoselov, K. Graphene plasmonics. *Nature photonics* **6**, 749 (2012).
- [72] Koppens, F. H., Chang, D. E. & Garcia de Abajo, F. J. Graphene plasmonics: a platform for strong light–matter interactions. *Nano letters* **11**, 3370–3377 (2011).
- [73] Rakić, A. D., Djurišić, A. B., Elazar, J. M. & Majewski, M. L. Optical properties of metallic films for vertical-cavity optoelectronic devices. *Applied optics* **37**, 5271–5283 (1998).

- [74] Grigorenko, A., Polini, M. & Novoselov, K. Graphene plasmonics. *Nature photonics* **6**, 749 (2012).
- [75] Jablan, M., Buljan, H. & Soljačić, M. Plasmonics in graphene at infrared frequencies. *Physical review B* **80**, 245435 (2009).
- [76] Rupasinghe, C., Rukhlenko, I. D. & Premaratne, M. Spaser made of graphene and carbon nanotubes. *ACS Nano* **8**, 2431–2438 (2014). PMID: 24559464, <https://doi.org/10.1021/nn406015d>.
- [77] Jayasekara, C., Premaratne, M., Stockman, M. I. & Gunapala, S. D. Multimode analysis of highly tunable, quantum cascade powered, circular graphene spaser. *Journal of Applied Physics* **118**, 173101 (2015).
- [78] Bao, Q. *et al.* Broadband graphene polarizer. *Nature photonics* **5**, 411 (2011).
- [79] Falkovsky, L. Optical properties of graphene. In *Journal of Physics: Conference Series*, vol. 129, 012004 (IOP Publishing, 2008).
- [80] Wang, W., Xiao, S. & Mortensen, N. A. Localized plasmons in bilayer graphene nanodisks. *Physical Review B* **93**, 165407 (2016).
- [81] Fang, X.-Y. *et al.* Temperature-and thickness-dependent electrical conductivity of few-layer graphene and graphene nanosheets. *Physics Letters A* **379**, 2245–2251 (2015).
- [82] Hao, L. & Sheng, L. Optical conductivity of multilayer graphene. *Solid State Communications* **149**, 1962 – 1966 (2009). URL <http://www.sciencedirect.com/science/article/pii/S0038109809004566>.
- [83] Haus, J. 4 - materials. In Haus, J. W. (ed.) *Fundamentals and Applications of Nanophotonics*, 89 – 148 (Woodhead Publishing,

- 2016). URL <http://www.sciencedirect.com/science/article/pii/B978178242464200004X>.
- [84] Aram, T. N. & Mayou, D. Quantum two-level model for excitonic solar cells. *Solar Panels and Photovoltaic Materials* 29 (2018).
- [85] Liang, W. Excitons. *Physics Education* 5, 226 (1970).
- [86] Torchilin, V. *Handbook of nanobiomedical research: Fundamentals, applications, and recent developments*, vol. 3 (World scientific, 2014).
- [87] High, A., Hammack, A., Butov, L., Hanson, M. & Gossard, A. Exciton optoelectronic transistor. *Optics letters* 32, 2466–2468 (2007).
- [88] Fassioli, F., Dinshaw, R., Arpin, P. C. & Scholes, G. D. Photosynthetic light harvesting: excitons and coherence. *Journal of The Royal Society Interface* 11, 20130901 (2014).
- [89] Kamada, H. & Gotoh, H. Quantum computation with quantum dot excitons. *Semiconductor science and technology* 19, S392 (2004).
- [90] Amo, A. *et al.* Exciton–polariton spin switches. *Nature Photonics* 4, 361 (2010).
- [91] Andreakou, P. *et al.* Optically controlled excitonic transistor. *Applied Physics Letters* 104, 091101 (2014).
- [92] Griffiths, D. J. & Schroeter, D. F. *Introduction to quantum mechanics* (Cambridge University Press, 2018).
- [93] Peng, J.-S. & Li, G.-X. *Introduction to modern quantum optics* (World Scientific, 1998).
- [94] Mansur, H. S. Quantum dots and nanocomposites. *Wiley Interdisciplinary Reviews: Nanomedicine and Nanobiotechnology* 2, 113–129 (2010).

- [95] Resch-Genger, U., Grabolle, M., Cavaliere-Jaricot, S., Nitschke, R. & Nann, T. Quantum dots versus organic dyes as fluorescent labels. *Nature methods* **5**, 763 (2008).
- [96] Ruan, J. *et al.* Her2 monoclonal antibody conjugated rnase-a-associated cdte quantum dots for targeted imaging and therapy of gastric cancer. *Biomaterials* **33**, 7093–7102 (2012).
- [97] Yukawa, H. *et al.* Monitoring transplanted adipose tissue-derived stem cells combined with heparin in the liver by fluorescence imaging using quantum dots. *Biomaterials* **33**, 2177–2186 (2012).
- [98] Parak, W. J., Pellegrino, T. & Plank, C. Labelling of cells with quantum dots. *Nanotechnology* **16**, R9 (2005).
- [99] Holzinger, M., Le Goff, A. & Cosnier, S. Nanomaterials for biosensing applications: a review. *Frontiers in chemistry* **2**, 63 (2014).
- [100] Loss, D. & DiVincenzo, D. P. Quantum computation with quantum dots. *Physical Review A* **57**, 120 (1998).
- [101] Nabiev, I. *et al.* Fluorescent quantum dots as artificial antennas for enhanced light harvesting and energy transfer to photosynthetic reaction centers. *Angewandte Chemie International Edition* **49**, 7217–7221 (2010).
- [102] Spataru, C. D., Ismail-Beigi, S., Capaz, R. B. & Louie, S. G. Theory and ab initio calculation of radiative lifetime of excitons in semiconducting carbon nanotubes. *Phys. Rev. Lett.* **95**, 247402 (2005).
- [103] Dai, H. Carbon nanotubes: Synthesis, structure, properties, and applications. In *Topics in Applied Physics*, vol. 80 (Springer, 2001).
- [104] Saito, R., Dresselhaus, G. & Dresselhaus, M. S. *Physical properties of carbon nanotubes* (World Scientific, 1998).

- [105] Avouris, P., Freitag, M. & Perebeinos, V. Carbon-nanotube photonics and optoelectronics. *Nature photonics* **2**, 341 (2008).
- [106] Nanotubes, C. Synthesis, structure, properties, and applications. *Topics in applied physics* **80**, 113–146 (2001).
- [107] Duc Vu Quyen, N., Quang Khieu, D., Tuyen, T. N., Xuan Tin, D. & Thi Hoang Diem, B. Carbon nanotubes: Synthesis via chemical vapour deposition without hydrogen, surface modification, and application. *Journal of Chemistry* **2019** (2019).
- [108] Dobrzańska-Danikiewicz, A., Łukowiec, D., Cichocki, D. & Wolany, W. Carbon nanotubes manufacturing using the cvd equipment against the background of other methods. *Archives of Materials Science and Engineering* **64**, 103–109 (2013).
- [109] Shah, K. A., Najar, F. A., Sharda, T. & Sreenivas, K. Synthesis of multi-walled carbon nanotubes by thermal cvd technique on pt–w–mgo catalyst. *Journal of Taibah University for Science* **12**, 230–234 (2018).
- [110] Siddhardha, B. & Parasuraman, P. Theranostics application of nanomedicine in cancer detection and treatment. In *Nanomaterials for Drug Delivery and Therapy*, 59–89 (Elsevier, 2019).
- [111] Pan, J., Li, F. & Choi, J. H. Single-walled carbon nanotubes as optical probes for bio-sensing and imaging. *Journal of Materials Chemistry B* **5**, 6511–6522 (2017).
- [112] Ou, C. *et al.* A novel amperometric immunosensor based on layer-by-layer assembly of gold nanoparticles–multi-walled carbon nanotubes–thionine multilayer films on polyelectrolyte surface. *Analytica chimica acta* **603**, 205–213 (2007).

- [113] Cha, T.-G. *et al.* Optical nanosensor architecture for cell-signaling molecules using dna aptamer-coated carbon nanotubes. *ACS nano* **5**, 4236–4244 (2011).
- [114] Wang, J. & Lin, Y. Functionalized carbon nanotubes and nanofibers for biosensing applications. *TrAC Trends in Analytical Chemistry* **27**, 619 – 626 (2008). URL <http://www.sciencedirect.com/science/article/pii/S0165993608001283>. Electroanalysis Based on Nanomaterials.
- [115] Yang, N., Chen, X., Ren, T., Zhang, P. & Yang, D. Carbon nanotube based biosensors. *Sensors and Actuators B: Chemical* **207**, 690–715 (2015).
- [116] Dang, X. *et al.* Layer-by-layer assembled fluorescent probes in the second near-infrared window for systemic delivery and detection of ovarian cancer. *Proceedings of the National Academy of Sciences* **113**, 5179–5184 (2016).
- [117] Welsher, K., Sherlock, S. P. & Dai, H. Deep-tissue anatomical imaging of mice using carbon nanotube fluorophores in the second near-infrared window. *Proceedings of the National Academy of Sciences* **108**, 8943–8948 (2011).
- [118] Hong, G. *et al.* Multifunctional in vivo vascular imaging using near-infrared ii fluorescence. *Nature medicine* **18**, 1841 (2012).
- [119] Bianco, A., Kostarelos, K. & Prato, M. Applications of carbon nanotubes in drug delivery. *Current opinion in chemical biology* **9**, 674–679 (2005).
- [120] Singh, R. & Torti, S. V. Carbon nanotubes in hyperthermia therapy. *Advanced drug delivery reviews* **65**, 2045–2060 (2013).
- [121] Bradburne, C. E. *et al.* Cytotoxicity of quantum dots used for in vitro cellular labeling: role of qd surface ligand, delivery modality, cell type, and direct comparison to organic fluorophores. *Bioconjugate chemistry* **24**, 1570–1583 (2013).

- [122] Chen, N. *et al.* The cytotoxicity of cadmium-based quantum dots. *Biomaterials* **33**, 1238–1244 (2012).
- [123] Lin, J., Huang, Y. & Huang, P. Graphene-based nanomaterials in bioimaging. In *Biomedical Applications of Functionalized Nanomaterials*, 247–287 (Elsevier, 2018).
- [124] Liu, Z., Tabakman, S., Welsher, K. & Dai, H. Carbon nanotubes in biology and medicine: in vitro and in vivo detection, imaging and drug delivery. *Nano research* **2**, 85–120 (2009).
- [125] Sarid, D. & Challener, W. A. *Modern introduction to surface plasmons: theory, Mathematica modeling, and applications* (Cambridge University Press, 2010).
- [126] Hohenester, U. & Trugler, A. Interaction of single molecules with metallic nanoparticles. *IEEE Journal of Selected Topics in Quantum Electronics* **14**, 1430–1440 (2008).
- [127] Carmichael, H. Photon antibunching and squeezing for a single atom in a resonant cavity. *Physical review letters* **55**, 2790 (1985).
- [128] Ficek, Z. Gulfam, qurrat-ul-ain, z. ficek, and j. evers, *phys. rev. a* **86**, 022325 (2012). *Phys. Rev. A* **86**, 022325 (2012).
- [129] Weeraddana, D., Premaratne, M. & Andrews, D. L. Quantum electrodynamics of resonance energy transfer in nanowire systems. *Physical Review B* **93**, 075151 (2016).
- [130] Salasnich, L. *Quantum Physics of Light and Matter: A Modern Introduction to Photons, Atoms and Many-Body Systems* (Springer, 2014).
- [131] Blum, K. *Density matrix theory and applications*, vol. 64 (Springer Science & Business Media, 2012).

- [132] Wiseman, H. M. & Milburn, G. J. *Quantum measurement and control* (Cambridge University Press, 2009).
- [133] Scully, M. O. & Zubairy, M. S. *Quantum optics* (Cambridge university press, 1997), 6 edn.
- [134] Gardiner, C., Zoller, P. & Zoller, P. *Quantum noise: a handbook of Markovian and non-Markovian quantum stochastic methods with applications to quantum optics*, vol. 56 (Springer Science & Business Media, 2004).
- [135] Lindblad, G. On the generators of quantum dynamical semigroups. *Communications in Mathematical Physics* **48**, 119–130 (1976).
- [136] Waks, E. & Sridharan, D. Cavity qed treatment of interactions between a metal nanoparticle and a dipole emitter. *Phys. Rev. A* **82**, 043845 (2010).
- [137] Sakoda, K. *Optical properties of photonic crystals*, vol. 80 (Springer Science & Business Media, 2004), 2 edn.
- [138] Wang, F. & Shen, Y. R. General properties of local plasmons in metal nanostructures. *Physical review letters* **97**, 206806 (2006).
- [139] Hanarp, P., Käll, M. & Sutherland, D. S. Optical properties of short range ordered arrays of nanometer gold disks prepared by colloidal lithography. *The Journal of Physical Chemistry B* **107**, 5768–5772 (2003).
- [140] Langhammer, C., Schwind, M., Kasemo, B. & Zoric, I. Localized surface plasmon resonances in aluminum nanodisks. *Nano letters* **8**, 1461–1471 (2008).
- [141] Kane, B. Levitated spinning graphene flakes in an electric quadrupole ion trap. *Physical Review B* **82**, 115441 (2010).

- [142] Bohren, C. F. & Huffman, D. R. *Absorption and scattering of light by small particles* (John Wiley & Sons, 2008).
- [143] Le Ru, E. & Etchegoin, P. *Principles of surface enhanced Raman scattering and related plasmonic effects* (Elsevier, Amsterdam, 2009).
- [144] Weitkamp, C. *Lidar: range-resolved optical remote sensing of the atmosphere*, vol. 102 (Springer Science & Business, 2006).
- [145] Morton, J. G., Day, E. S., Halas, N. J. & West, J. L. Nanoshells for photothermal cancer therapy. In *Cancer nanotechnology*, 101–117 (Springer, 2010).
- [146] Lal, S., Clare, S. E. & Halas, N. J. Nanoshell-enabled photothermal cancer therapy: impending clinical impact. *Accounts of chemical research* **41**, 1842–1851 (2008).
- [147] Portney, N. G. & Ozkan, M. Nano-oncology: drug delivery, imaging, and sensing. *Analytical and bioanalytical chemistry* **384**, 620–630 (2006).
- [148] Hirsch, L. R. *et al.* Metal nanoshells. *Annals of biomedical engineering* **34**, 15–22 (2006).
- [149] Chettiar, U. K. & Engheta, N. Internal homogenization: Effective permittivity of a coated sphere. *Optics express* **20**, 22976–22986 (2012).
- [150] Vial, A. & Laroche, T. Description of dispersion properties of metals by means of the critical points model and application to the study of resonant structures using the fdtd method. *Journal of Physics D: Applied Physics* **40**, 7152 (2007).
- [151] Prodan, E., Radloff, C., Halas, N. J. & Nordlander, P. A hybridization model for the plasmon response of complex nanostructures. *science* **302**, 419–422 (2003).

- [152] Nurunnabi, M., Khatun, Z., Reeck, G. R., Lee, D. Y. & Lee, Y.-k. Near infrared photoluminescent graphene nanoparticles greatly expand their use in noninvasive biomedical imaging. *Chemical Communications* **49**, 5079–5081 (2013).
- [153] Koppens, F. H., Chang, D. E. & Garcia de Abajo, F. J. Graphene plasmonics: a platform for strong light–matter interactions. *Nano letters* **11**, 3370–3377 (2011).
- [154] Yang, K. *et al.* Graphene in mice: ultrahigh in vivo tumor uptake and efficient photothermal therapy. *Nano letters* **10**, 3318–3323 (2010).
- [155] Kondo, D., Sato, S. & Awano, Y. Self-organization of novel carbon composite structure: graphene multi-layers combined perpendicularly with aligned carbon nanotubes. *Applied physics express* **1**, 074003 (2008).
- [156] Rao, R. *et al.* Graphene as an atomically thin interface for growth of vertically aligned carbon nanotubes. *Scientific reports* **3**, 1891 (2013).
- [157] Tung, V. C. *et al.* Low-temperature solution processing of graphene- carbon nanotube hybrid materials for high-performance transparent conductors. *Nano letters* **9**, 1949–1955 (2009).
- [158] Yu, D. & Dai, L. Self-assembled graphene/carbon nanotube hybrid films for supercapacitors. *The Journal of Physical Chemistry Letters* **1**, 467–470 (2009).
- [159] Khan, U., O'Connor, I., Gun'ko, Y. K. & Coleman, J. N. The preparation of hybrid films of carbon nanotubes and nano-graphite/graphene with excellent mechanical and electrical properties. *Carbon* **48**, 2825–2830 (2010).

- [160] Das, S. *et al.* Synthesis and characterization of self-organized multilayered graphene–carbon nanotube hybrid films. *Journal of Materials Chemistry* **21**, 7289–7295 (2011).
- [161] Kong, H. Hybrids of carbon nanotubes and graphene/graphene oxide. *Current Opinion in Solid State and Materials Science* **17**, 31–37 (2013).
- [162] Xia, K., Zhan, H. & Gu, Y. Graphene and carbon nanotube hybrid structure: a review. *Procedia IUTAM* **21**, 94–101 (2017).
- [163] Zhu, Y. *et al.* A seamless three-dimensional carbon nanotube graphene hybrid material. *Nature communications* **3**, 1225 (2012).
- [164] Lv, R., Cruz-Silva, E. & Terrones, M. Building complex hybrid carbon architectures by covalent interconnections: Graphene–nanotube hybrids and more. *ACS nano* **8**, 4061–4069 (2014).
- [165] Li, J.-J. & Zhu, K.-D. Tunable slow and fast light device based on a carbon nanotube resonator. *Optics Express* **20**, 5840–5848 (2012).
- [166] Song, D. *et al.* Measurement of the optical stark effect in semiconducting carbon nanotubes. *Applied Physics A* **96**, 283–287 (2009).
- [167] Huang, K. *et al.* Size-dependent localization and penetration of ultrasmall gold nanoparticles in cancer cells, multicellular spheroids, and tumors in vivo. *ACS nano* **6**, 4483–4493 (2012).
- [168] Luk'yanchuk, B. *et al.* The fano resonance in plasmonic nanostructures and metamaterials. *Nature materials* **9**, 707 (2010).
- [169] Liu, J., Jalali, M., Mahshid, S. & Wachsmann-Hogiu, S. Are plasmonic optical biosensors ready for use in point-of-need applications? *Analyst* (2020).

- [170] Liu, B., Zhu, W., Gunapala, S. D., Stockman, M. I. & Premaratne, M. Open resonator electric spaser. *ACS nano* **11**, 12573–12582 (2017).
- [171] Shukla, T., Upmanyu, N., Pandey, S. P. & Sudheesh, M. Site-specific drug delivery, targeting, and gene therapy. In *Nanoarchitectonics in Biomedicine*, 473–505 (Elsevier, 2019).
- [172] Iyer, A. K., Khaled, G., Fang, J. & Maeda, H. Exploiting the enhanced permeability and retention effect for tumor targeting. *Drug discovery today* **11**, 812–818 (2006).
- [173] Greish, K. Enhanced permeability and retention (epr) effect for anticancer nanomedicine drug targeting. In *Cancer nanotechnology*, 25–37 (Springer, 2010).
- [174] Singhana, B., Slattery, P. & Melancon, M. P. Targeted gold nanoshells. In *Applications of Nanoscience in Photomedicine*, 267–290 (Elsevier, 2015).
- [175] Aminzadeh, R., Saviz, M. & Shishegar, A. A. Dielectric properties estimation of normal and malignant skin tissues at millimeter-wave frequencies using effective medium theory. In *Electrical Engineering (ICEE), 2014 22nd Iranian Conference on*, 1657–1661 (IEEE, 2014).
- [176] Ross, K. & Gordon, R. Water in malignant tissue, measured by cell refractometry and nuclear magnetic resonance. *Journal of microscopy* **128**, 7–21 (1982).